Adhesion in Hydrogel Contacts

by

Jahn Ramón Torres Jové

B. Sc., Virginia Commonwealth University, 2001

Sc. M., Brown University, 2005

Thesis

Submitted in partial fulfillment of the requirements for the Degree of Doctor of Philosophy in the School of Engineering at Brown University

PROVIDENCE, RHODE ISLAND

MAY 2015

This dissertation by Jahn R. Torres Jové is accepted in its present form

by the School of Engineering as satisfying the

dissertation requirements for the degree of Doctor of Philosophy.

Date _____ _____

Kyung-Suk Kim, Advisor

Recommended to the Graduate Council

Date _____ _____

Gregory D. Jay, Reader

Date _____ _____

Christian Franck, Reader

Approved by the Graduate Council

Date _____ _____

Peter M. Weber, Dean of the Graduate School

Curriculum Vitae

Jahn R. Torres Jové was born on November 6, in the year of 1978 in Ponce, Puerto Rico. He attended the Virginia Commonwealth University in Richmond, Virginia where he completed a Bachelors of Science degree in Mechanical Engineering in 2001. He entered the Fluid and Thermal Sciences Group in the Division of Engineering at Brown University, where he completed a Science Masters degree in Engineering in 2005. He joined the Solid Mechanics Group in the School of Engineering at Brown University in 2010.

Acknowledgements

I would like to express my gratitude to my advisor Prof. Kyung-Suk Kim for his support. His knowledge both in depth and breadth has served as an inspiration to systematically and rigorously approach the multi-disciplinary phenomena described in this work. His constant challenge of my assumptions has driven me to objectively pursue experimental work grounded in mechanical theory. I must also express my gratitude to Dr. Gregory D. Jay for his invaluable guidance through my years as a graduate student. To Prof. Kenneth S. Breuer, I give thanks for patiently teaching me the value of rigorous experiments grounded in analytical work. Prof. Allan Bower has kindly provided his technical insight, patient guidance and corrections on my many errors. I must also acknowledge Prof. Hanish Kesari; for his insights in dissipation allowed me to completely change the way I approached the phenomena of adhesion. Prof. Geoffrey D. Bothun from the University of Rhode Island provided his technical assistance and many fruitful conversations. His selfless collaborative attitude made this work possible.

During the course of this work I have gained a deep appreciation of the great support that Dr. Fletcher A. Blackmon has provided to me over the years. His unflappable encouragement has made the completion of this work possible. Thanks should also go to Dr. Harold C. Robinson for his guidance; Mr. Joseph Stace for always providing his expertise and perspective; Dr. Vittorio Ricci and Dr. Lynn Ewart-Paine for their professional guidance; all from the Naval Undersea Warfare Center.

Many present and past laboratory coworkers were very generous with their technical and moral succor. These include laboratory mates in the Nano and Micromechanics Laboratory; Dr. Mazen Diab, Dr. Jin-Woo Yi, Dr. Sang-Pil Kim, Dr.

Chien-Kai Wang, and Dr. Hsiao-Mei Wu, as well as Mr. Anthony McCormick from the Electron Microscopy Facility and Mr. Michael Monn from the Solid Mechanics Group, at Brown University. Acknowledgement should also be made of colleagues; Ms. Jillian Kiser and Mr. Colin Murphy from the Naval Undersea Warfare Center.

I must give thanks to my parents and siblings for serving as examples of perseverance, moral rectitude and professional excellence. Most importantly my eternal gratitude goes to my wife and son who have served as inspiration and technical guides, and have never complained about the sacrifice of time that has accompanied this endeavor. Without them there would be nothing.

Abstract of “Adhesion in Hydrogel Contacts” by Jahn R. Torres Jové, Ph.D., Brown University, May 2015

A generalized thermoelastic model for adhesion was developed to elucidate the mechanism of dissipation within the viscoelastic bulk of a hydrogel. Results show that in addition to the expected energy release rate of interface formation as well as the viscoelastic drag and viscous flow dissipation, the bulk composition exhibit dissipation due to phase inhomogeneity motion. The mixing thermodynamics of the matrix and solvent composition determine the dynamics of the phase inhomogeneities, which can enhance or disrupt adhesion. The model also accounts for the time dependent behavior since, given enough time, these inhomogeneities can be influenced by image forces at the interface causing migration, which may in turn, affect the dissipation at the interface. A nondimensional parameter is proposed to discern the dominant dissipation mechanism in hyperelastic contact detachment.

Table of Contents

Table of Figures

List of Tables

Chapter 1.0: Introduction

Abstract

This dissertation presents a comprehensive treatment of the mechanisms involved in the adhesion of hydrogel contacts, which affect the interaction between biological and synthetic surfaces found in applications from diarthrodial joints of the human body to submerged surfaces in marine environments. The intention herein is to develop a parametric study to elucidate the adhesive interaction in soft hydrogel material contacts. A number of advances are introduced, which include a new mechanism for adhesive energy dissipation which depends on the mixing affinity of the polymer and solvent in the hydrogel; a novel calibration technique for normal force measurements in the atomic force microscope which enabled the highly accuracy needed to measure the properties of a multi-layered structure which gives rise to the formation of nested wrinkles on a PDMS substrate.

1.1 Background of Hydrogel Adhesion

Interest in self-cleaning, low adhesion coatings for biomedical applications, optical surfaces in harsh environments, friction reduction and antifouling of structures in the maritime environment, have renewed the impetus to study polymeric coatings as a means of surface protection. Work in these fields has given rise to the need to characterize the adhesion between synthetic and biological interfaces. The biofouling of synthetic surfaces may shorten the productive life of man-made devices intended to improve the economic, and health of individuals in society. Adhesion is an important

aspect in the performance of surfaces used in devices ranging from those that must reside within the human body in order to replace or improve the function of biological systems, to maritime structures intended for defense or the exploitation of natural resources at minimal environmental cost. All of these synthetic surfaces will be quickly affected by biofouling after residing in their intended environments beyond a critical time.

The settlement of fouling agents on water-contacting surfaces is of great cost to society due to labor intensive cleaning, material deterioration and energy losses from drag (Huergo 2003). The variety and tenacity of biofouling organisms in these maritime environments provides for a complex engineering problem that if solved, or even improved, could reap considerable returns. Recent work has focused on coatings that should eliminate biofouling agent proliferation by inhibiting initial agent spore/cellular adhesion to the coated surfaces (Costerton 2001, Callow 2006). Previous studies have shown a decrease in biofouling agent adhesion to substrates with a variety of surface chemistries and morphologies. Some of the chemistries, which include dual domain (hydrophobic/hydrophilic) polymers (Gudipati 2007) and bio-inspired proteins (Statz 2008), show improvements over polydimethylsiloxane-based (PDMS-based) polymers that rely on their non-wetting nature to reduce contact between fouling agent and the synthetic surface (Kavanaugh 2003). Although not well understood, it is thought that dual domain features provide for increased thermodynamic and geometric resistance to the adsorption of adhesive glycoproteins used by the biofouling agents. To improve upon these effects, micro-scale surface morphological features have been added to enhance hydrophobicity (Hoipkemeier-Wilson 2004).

In other applications, such as diarthrodial joint replacements, the intent may be to improve adhesion between the synthetic stem and biological bone surfaces in order to avoid osteolytic disintegration of the interface. In diatrhodial joint lubrication, adhesion has been used to assess the lubricating effects of a number of synovial fluid constituents. This work has made use of lubricin, a glycoprotein responsible for boundary lubrication in human diarthrodial joints (Radin 1970), for the study of adhesive hydrogel coatings. Lubricin, (MW ~ 260kDa) with non-polar, net *positively charged* globular terminal domains and a polar, net negatively charged central region that is extensively modified by oligosaccharide side chains (Jay 2001), has previously been shown to lower the effective work of adhesion between synthetic surfaces (Jay 2007). It has been recently proposed that the polymer brush nature of lubricin along with a combination of *steric hindrance*, *electrostatic double layer* and *hydration repulsive forces* are responsible for its low adhesive and frictional properties when grafted onto a surface (Zappone 2007). Interestingly, other grafted polymer hydrogel coatings with these similar qualities do not show the frictional and adhesive performance of lubricin, which reduces adhesion and friction to the lowest levels reported (Jay 1992). Lubricin's amphipathic nature along with its polyelectrolytic nature allows it to interact with a wide variety of surfaces.

It is in this context, the specific problem of adhesion has been studied with the intent to develop a generalized model that may allow for adhesive effects to be optimized based on applications.

1.2 Theoretical Framework for Contacts

The modern treatment of contact mechanics is said to have started when Hertz formulated the first solution for the stress field within a half-space that was being impinged upon by a spherical body, published in 1882 (Hertz 1881, 1882). His solution was only applicable to the frictionless contact which exhibited no adhesion. At the time, efforts had been mostly concentrated in finding solutions to specific boundary-value problems using mathematical approximations. Before this only rough estimates for the frictional behavior of interfacing surfaces existed and it wasn't until works by Bowden and Tabor (1954) that the effects of asperities and other molecular variables on the shear strength of a contact started to be considered (Bowden 1952). Soon after, Archard studied the effects of loads on the real area of contacts produced by plastically deforming asperities, which developed wear upon experiencing shear stresses (Archard 1953).

It wasn't until Johnson, Kendal and Roberts' model, known today as the JKR model, that a solution of the relationship between adhesive forces and the contact area exhibited between contacting surfaces was produced (Johnson 1971). In this work, a variational approach was used to calculate the area between contacting solids, which achieved a minimum state of energy with contributions from the surface energy. The JKR model remains the prevalent model used for soft elastic contacts. Derjaguin, Muller, and Toporov (DMT, 1975) developed a similar model by a different approach, namely by emphasizing the difference between the Hertzian model and the area ring bounding contact. This area was deemed as the effective area of action for the adhesive forces. Work in the area of viscoelastic contacts started earlier. Andrews and Kinloch (1973) investigated the effects of viscous dissipation on the interfacial crack front as a result of

studies by Gent and Petrich (1969), and later Gent and Schultz (1972) (Gent 1969, Gent 1972, Andrews 1973). In their work, Gent *et al*. documented the changes in peel force as a function of rate of extension and later energy release rate as a function of crack front speed along with mixed adhesive and cohesive failure modes. The importance of the work by Gent and Petrich (1969) of the correlation between the energy release rate and the viscoelastic behavior of the polymers cannot be exaggerated (Gent 1969). An outstanding summary of this work along with updated advances was published by Maugis and Barquins (Maugis 1978). Greenwood and Johnson (1981) published a constitutive treatment of viscoelastic contacts which also included the effects of the surface interactions (Greenwood 1981). Today, the maximum adhesion energy predicted by such models remains of interest for most engineering applications.

More recently, the surface roughness has been identified to create inhomogeneous stresses which reach the critical load for defect size growth threshold necessary for the interfacial crack to break contact (Gao 2004). Contact instability during detachment has been seen in soft polymers (Chung 2006). The dissipative detachment mechanism was first described by Li and Kim as instabilities (Li 2009), which cause deviations between the JKR-predicted and the actual-achieved adhesive dissipation. Kesari et. al. also demonstrated this to be a phenomena within rough contacts (Kesari 2009).

In this thesis work, the adhesive contact between swollen viscoelastic hydrogels was investigated. A model developed within thermodynamic and mechanical constraints was sought, which remains consistent with the previous models discussed.

1.3 Metrics for the Evaluation of Adhesion to Coatings

Surface energy is often used as a performance metric for anti-fouling coatings, but this practice is quickly falling out of favor due to a lack of phenomenological data correlation between fouling incidence and surface energy. A close look at the available data will show that the macroscale wettability effect is unsuitable to predict the anti-fouling effectiveness of coatings (Hoipkemeier-Wilson 2004, Callow 2000, Genzer 2006). A number of groups have found that glycoprotein-mediated adhesion involves interactions that depend on molecular forces and surface topographical features that can be quite complex (Torres 2005, Sigal 1998, Jay 2007, Zappone 2007). Fouling agent adhesion is invariably affected by fluid-swollen glycoprotein interfacial contacts.

The bottom of figure 1.1 shows in the left ordinate, the average bead radius-normalized adhesive force measured during pulse-force modulation (PFM) atomic force microscopy (AFM) measurements along with the contact angle measurements in the right ordinate axis for a number of grafted polymer coatings (polymer brushes) including the PRG4 glycoprotein, known as Lubrincin, labeled as LUB250. Lubricin exhibits the lowest contact angle at 8.7º, similar to a superhydrophilic swollen hydrogel, along with an average adhesive force of 4.095 ± 0.047 mN/m.

The contact angle equilibrium was attained within a timescale on the order of seconds. Polystyrene polymer brushes (1.0PS(6hr)) exhibited hydrophobic behavior ($\theta_{ls} > 90^{o}$) as well as the highest adhesive forces. With the polyacrylic acid brushes (PAA) exhibiting a wide range of average adhesive forces from as low as 7.6 ± 0.8 mN/m to 35.7 ± 2.4 mN/m, with contact angles of 56 º and 80º due to the range in grafting densities. The polystyrene-b-poly(acrylic acid) (PSbPAA) dual domain brushes exhibited

the lowest adhesion forces with 3.1 ± 0.3 mN/m. The top of figure 1.1 shows the results of settlement of ulva algae spores on the hydrogel coatings.

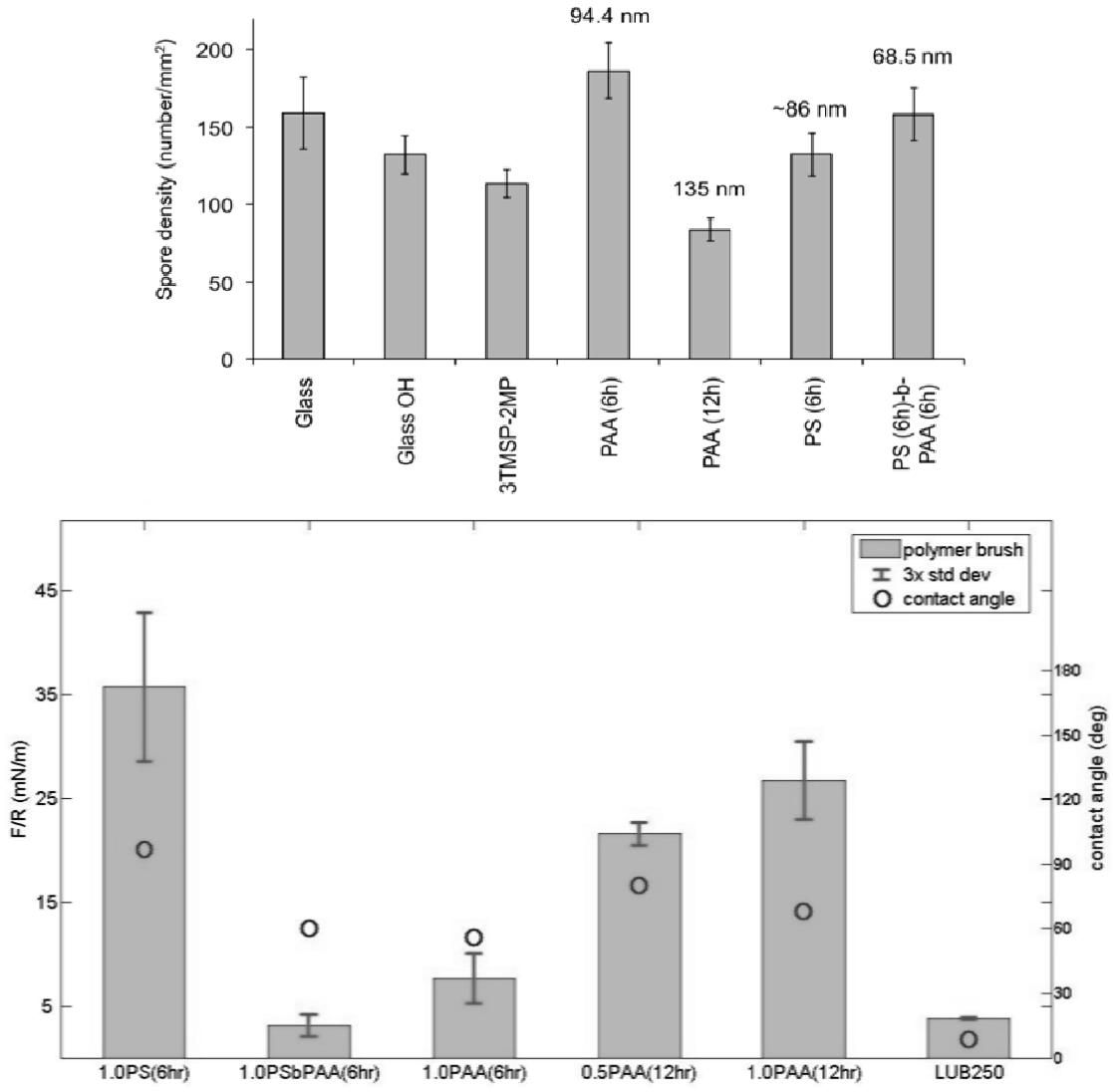

Figure 1.1 Ulva spore settlement density (top) for each of the hydrogel coatings studied. The grafted dry length in nanometers is reported above each bar for the hydrogles. Contact radius-normalized force of adhesion (bottom) measured with the AFM borosilicate colloidal probe (left ordinate) and corresponding contact angle measured (right ordinate) for each hydrogel coating (abscissa). Three standard deviation limits are also reported (brackets).

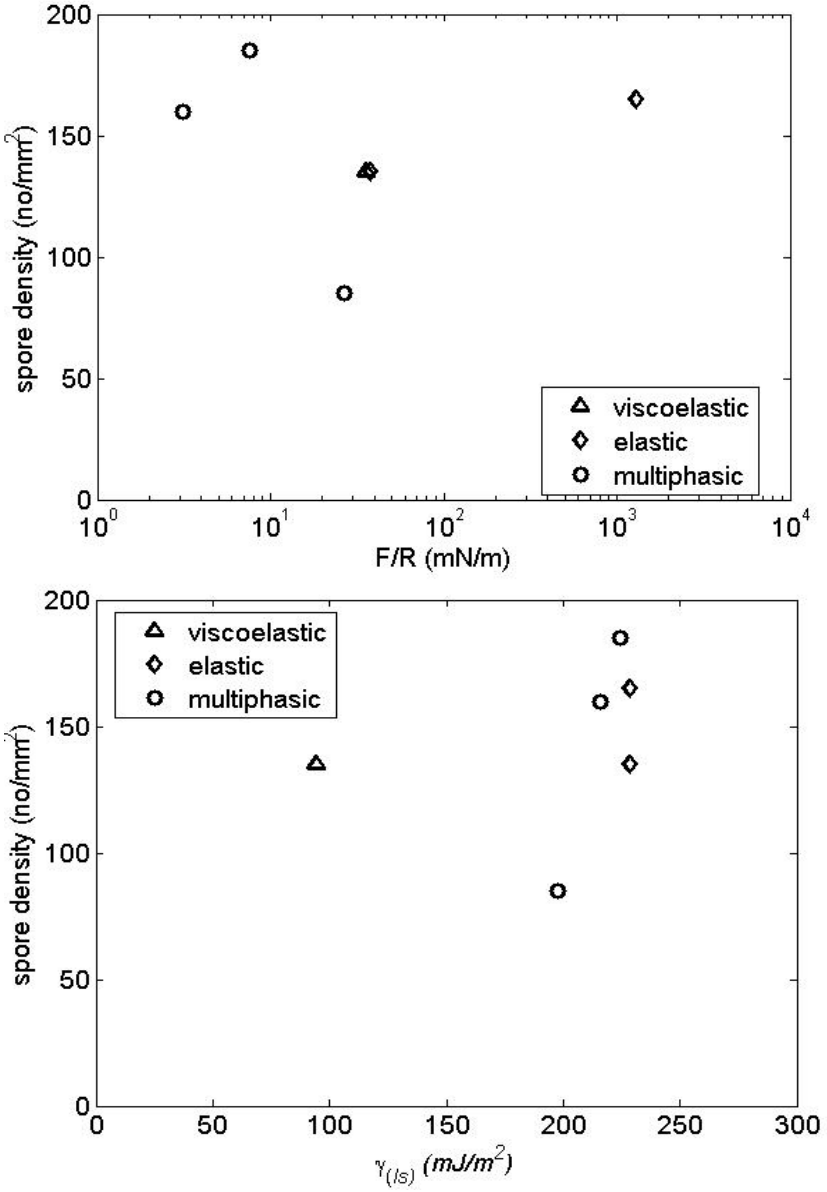

Figure 1.2 Ulva spore settlement density as a function of normalized pull-off force (top) and liquid-solid surface energy (bottom).

A careful study of figure 1.2 shows the lack of general correlation between spore settlement with adhesive force (top) and liquid-solid surface energy (bottom), for coatings in general. It should be noted that lubricin has been shown to inhibit cell adhesion as well as inhibit biofouling settlement (Aninwene 2014) although its

superhydrophilic nature puts it in the high liquid-solid surface energy range (>300mJ/m^2).

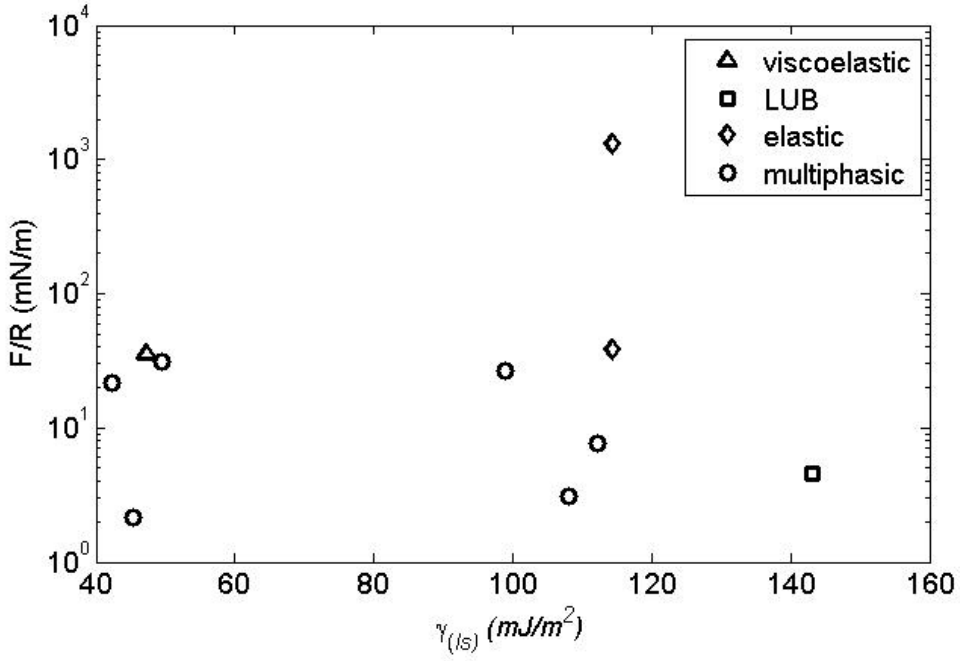

Figure 1.3 Normalized pull-off force as a function of surface energy for all coatings tested.

Figure 1.3 shows that the hydrophilicity (liquid-solid surface energy) in hydrogel coatings does not directly correlate well to the pull-off force at separation of the colloidal probe from the substrate.

Although the low force of adhesion in some polymer brush hydrogels has been attributed to the mechanism for repulsion and/or anti-adhesion being of the *steric-entropic* and *hydration repulsive* types (deGennes 1987, Israelachvili 1991), under loads where contact is attained, the detachment mechanism characteristic of adhesion is quite distinct from a mere repulsive effect. This suggests that the underlying mechanism at play in the adhesive glycoprotein is micromechanical in nature, as opposed to a thermodynamic macroscopic phenomenon, like wettability. Efforts to minimize fouling

by manipulating surface energy have proven marginally effective mainly due to a lack of understanding of the detachment mechanisms at play in the observed low adhesion phenomena. In this work, a direct adhesion energy measurement is conducted using the atomic force microscopy and correlated to a number of detachment mechanisms.. It is a characteristic of viscoelastic contacts that contact surfaces exhibiting different amounts of dissipated energy may exhibit the same pull-off force. While a force is applied, changes in the contact strain allow for the forces to remain constant. Therefore, it is the energy dissipated that is most relevant in quantifying adhesion and not the pull-off force during detachment.

1.4 Surface Roughness

Surface structures with complex morphology have been the focus of much recent research activities, motivated by the observations which strongly implicate morphology in the adhesive behavior of surfaces (Johnson 1984). Surface roughness as an essential enhancer of the hydrophobicity of a surface was first reported by Wenzel in the 1930's (Wenzel 1936), but renewed interest has been sparked by new knowledge on the ability to control adhesion by producing hierarchical roughness in functional surfaces. The use of roughness for biochemically resistant surfaces (Sigal 1998), and water dispersion control surfaces has been studied in different given environments.

The modeling of phenomenology such as adhesion, traditionally characterized within the realm of material properties, has seen an increased emphasis on the study of the relationships between material properties and hierarchical structures (Efimenko 2002). It has been widely observed in nature that the surface functionality of many

specialized organisms, which includes self-cleaning and anti-fouling, lies in the morphology of the hierarchical structures within these surfaces. These multi-scale, hierarchical surface structures observed in self-cleaning phenomena has made it desirable to design and control surface morphology at discrete length scales. These engineered surfaces have also been shown to have potential to provide solutions to a wide range of problems, from synthetic adhesive systems and improved interfacial toughness, to the understanding of the biolubrication within natural joints as well as the improvement of biocompatibility between human and synthetic materials. Several research groups (Long 2009, Efimenko 2009) have shown the advantage of using coatings which employ multi-scale surface patterns in reducing biofouling of marine structures. Rahmawan et al. (Rahmawan 2010) designed a dual-scale hierarchical structure by depositing diamond-like carbon (DLC) thin films onto poly(dimethyl) siloxane (PDMS) cast molded micropillars. After fouling adhesion studies, they showed experimental evidence that surface superhydrophobicity may be achieved by tuning the morphology of the surface structures. Zhang et al. (Zhang 2012) developed a semi-empirical model that is based on the concept of hierarchical wrinkling to design mechanically controlled multifunctional devices. In that case, the surface properties can be changed from superhydrophilicity to superhydrophobicity by modulating the applied mechanical loading. This multi-scale hierarchical wrinkle may be used to produce smart coatings that can render the surface non-wettable or wettable based on need. Nevertheless, the elastic mechanism governing the formation of hierarchical nested wrinkles on soft surfaces has remained elusive. In this thesis work, a highly accurate measurements of the elastic modulus as a function of depth into the substrate, along with results from a linear bifurcation analysis will show

that the stress state within the interfaces of a multi-layer system of mismatching mechanical properties is responsible for the appearance of nested wrinkles in the surface of a UV radiation-treated poly(dimethyl) siloxane (PDMS) substrate.

1.5 Models for the Mechanics of Hydrogels

Hydrogels are swollen polymeric networks of synthetic and biological origins, which show phase segregation at different length scales. At the microscopic level, the solvent swells the polymer network increasing its volume, changing its mechanical properties. Chemical crosslinks can govern the thermomechanics of the system by forcing two polymer chains to remain close at volume fractions that would otherwise induce a separation (deGennes 1979). In biological systems what is considered a "good solvent" for the gel network formation may be a "bad solvent" for other functional and biologically relevant components. Therefore, inhomogeneities are a particular feature of gels at the microscopic level since, in their simplest form, gels are a mixture of a larger solid scaffold network and a liquid solvent, both of which can be fluid to different degrees. These and other characteristics make hydrogels an essential material component of biological systems governing the mechanics of animal tissue deformation (Nelson 2000, deGennes 1979), the lubricating and viscoelastic response of synovial fluid in diarthrodial joints (Jay 2007b), as well as in the mediation of the biocompatibility of the synthetic-biological material interface of fouling maritime organisms and artificial organs in the human body.

With the advent of advanced interrogation techniques, considerable attention has been given to developing constitutive relations, which describe the complex and often

coupled mechanical and chemical response of hydrogels to external stimuli (Hong 2008, Hong 2009, Wu 2010, Li 2012). The current treatments of the chemical potential near the surface are grounded in the work by Flory (1943, 1944) and Asaro *et al.* (1972), which use a modification of Gibbs' working potential for homogenous mixtures in the treatment of stress-driven corrosion cracking. Larche *et. al*., described the transport within phases in the bulk of solids as arising from compositional inhomogeneities (Larche 1984). More precisely, it is the stress field due to the presence of the inhomogeneities that which induces the transport of species. This may be seen in a dual-domain material, where phase separation may exist at equilibrium, and transport only occurs during disturbances of such equilibrium upon an applied strain. Wu (Wu 1996) derived an expression for the chemical potential that included surface stresses, bulk strain energy and surface energy, lacking mixing entropy effects and thermal gradient forces. Similarly, Freund (Freund 1998) attempted to elucidate the nature of the chemical potential for elastostatic deformation. In the current thesis work, the chemical potential is taken to be a function of the entropy of mixing as in the Flory-Huggins model for mixtures ($\mu = \partial \psi_{H\,mix} / \partial \phi_p$) (Dill 2003).

1.6 Outline of Present Work

In this dissertation, the mechanisms which govern the adhesion of hydrogel surfaces are elucidated. This is done by presenting experimental evidence along with a theoretical framework that shows the effects of micromechanisms within the bulk which contribute to the energy necessary to separate two surfaces coated with polymer and solvent mixtures.

The adhesive energy between separating surfaces is quantified by employing the atomic force microscopy (AFM) normal force technique. In order to make precise measurements, a novel normal force calibration technique for direct AFM cantilever calibration is described in Chapter 2. The employment of this technique is shown in Chapter 3 to give the precise nanometer force measurement necessary to make measurements of the bulk modulus changes undergone by a polymer exposed to UV radiation, which in turn produces hierarchical roughness in the form of wrinkles. In Chapter 4, the adhesion of hydrogel contacts is shown to be influenced by the presence of the bulk inhomogeneous mixture of polymer and solvent. The adhesive behavior between multiphase hydrogels, viscoelastic and purely elastic solids is quantified by precise adhesion measurements. Chapter 5 includes a discussion of this work in relation to current and past work in the context of biofouling of surfaces and suggests further work necessary for its applica

Chapter 2.0: Diamagnetic Levitation Cantilever System for the Calibration of Normal Force Atomic Force Microscopy Measurements

Abstract

In this chapter a novel technique is reported for normal force calibration for Atomic Force Microcopy (AFM) adhesion measurements known as the diamagnetic normal force calibration (D-NFC) system. The levitation produced by the repulsion between a diamagnetic, highly ordered pyrolitic graphite (HOPG) sheet and four rare earth magnets is used to produce lossless spring. A silicon cantilever is balanced in the levitating graphite sheet, in order to produce an oscillation due to an unstable mechanical moment. The measurement of the natural frequency of this oscillation allows for the calculation of the stiffness of the system to three-digit accuracy. A number of cantilevers were calibrated with less than 1% error. The D-NFC response was proven to have a high sensitivity for the structure of water molecules collected on its surface. This in turns allows for the study of the effects of coatings on the structure of surface water. The potential for the use of the D-NFC system as a molecular structure detection system is also demonstrated.

2.1 Introduction

Over the last two decades multiple methods of calibrating the stiffness constant for atomic force microcopy cantilevers have been developed (Nonnenmacher 1990, Cleveland 1993, Torii 1996, Tortonese 1997, Sader 1999, Sader 1999b). All of these rely on the mechanical development of beam theory and do not account for the effects of roughness and dimensional variations, which may be significant at the micron-scale and on the order of 20% (Tortonese 1997). Furthermore, the analytical solution for V-shaped cantilevers is quite complex and present another instance for large uncertainty. Another shortcoming of present calibration techniques is the reliance on material properties like the density and/or mass of the cantilever, which has great variability due to the micro-fabrication techniques used. Nonenmacher and Cleveland *et al*. devised a calibration technique in which a number of masses are added to the AFM cantilever and the frequency of the mechanical response measured (Cleveland 1993). Sader et al. (1999b) made an improvement in the calibration values for stiffness by adding an analytical accounting of the viscous effects during dynamic stiffness measurements. In these methods the AFM cantilever is modeled as a massless spring with a concentrated end-mass assuming and an added mass several orders of magnitude larger than the cantilever mass. Even if assumed accurate, this process presents the mechanical challenges of placing a mass at a specific point in this micron scale system.

Thin layers of coatings used for improved reflection and conductivity exert a configurational pre-stress on the reflective surface of the cantilever, which may proof significant at small scales. These coatings are of varying thickness, which present

large uncertainties in the density measurements and therefore in calibrations dependent on calculations involving dimensional terms. Techniques dependent on the optically measured dimensions of the cantilever are subject to errors due to scattering of light and resolution of roughness if done under scanning electron microscopy (SEM). It is conceivable that a semi-empirical model may be developed to account to the effect of the roughness on the cantilever stiffness, but even under such a model the geometry of the cantilever must be accounted for as well as pre-stress effects of the reflective coatings and bulk residual stresses incurred during fabrication. Nevertheless, SEM measurements are costly and prohibitively inefficient for most laboratories.

Methods of absolute calibration developed by Torii *et al*. present the most practical alternatives but require a second calibrated cantilever (Torii 1996). Therefore, the uncertainty depends on the accuracy of the stiffness value for the reference cantilever. For these reference method cantilevers the difficulty lies in that the degree of uncertainty for the calibration is directly proportional to the stiffness or flexural rigidity of the reference cantilever $\left(u_c \propto \kappa_{REF}\right)$. On the other hand the stiffness of the cantilever maybe reduced by reducing the thickness of the cantilever, $\left(\kappa_{REF} \propto h^3\right)$ (Timoshenko 1959), which in turns increases the dimensional uncertainties.

2.2 Calibration Method

2.2.1 D-NFC System Method for Calibration of AFM Normal Force

The *diamagnetic normal force calibration* (D-NFC) system (figure 2.1) consists of a silicon cantilever bar supported on diamagnetic highly oriented pyrolitic graphite (HOPG) sheet levitated over four rare-earth magnets.

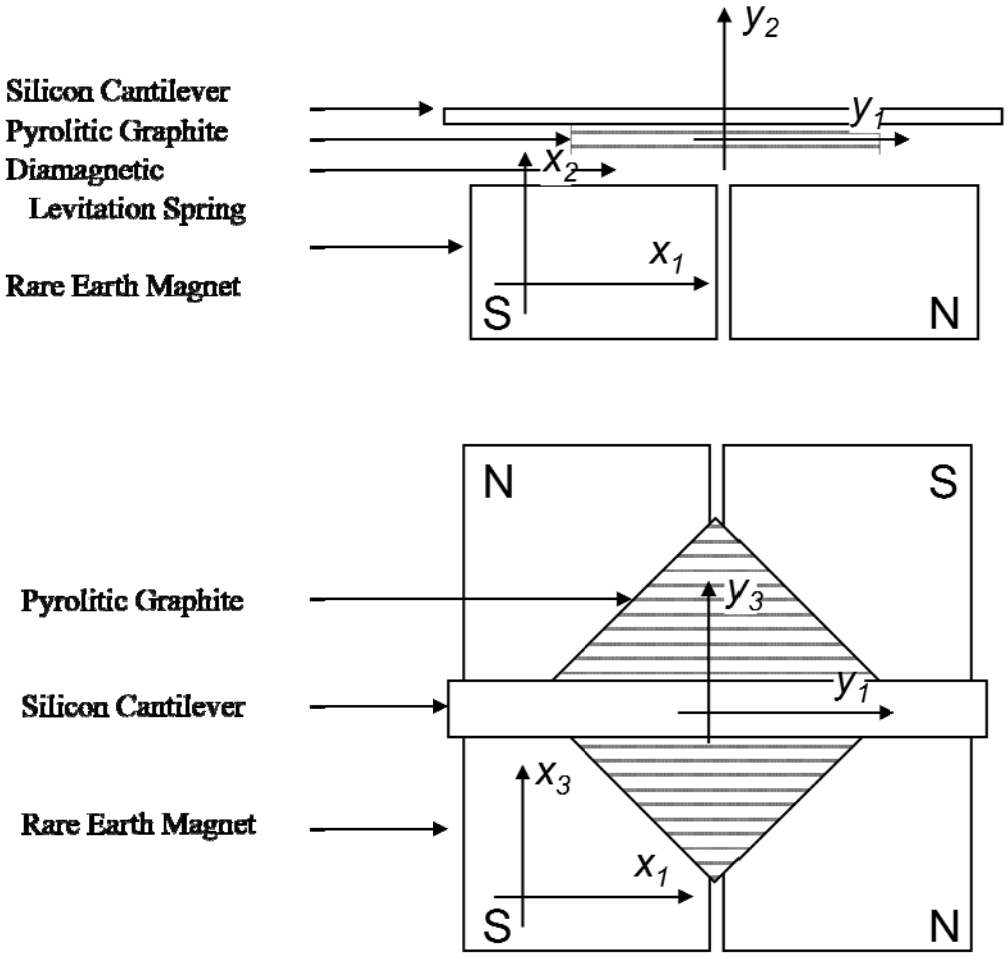

Figure 2.1 Load cell diagram for diamagnetic normal force calibration device (D-NFC) with a x-coordinate system and y-coordinate system describing the position and orientation of the rare earth magnet and the levitated mass, respectively.

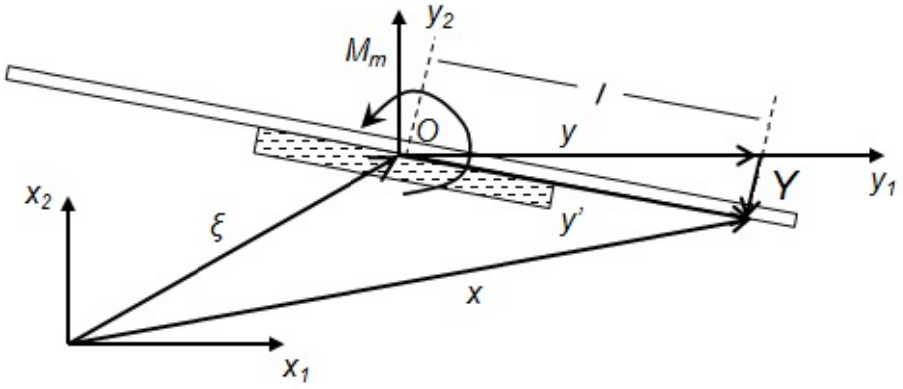

Figure 2.2 Spatial frame diagram for diamagnetic normal force calibration device (D-NFC) moving parts. Here **Y** = **y** x **Ω.**

A magnetic field potential well is produced by aligning four rare-earth magnets in north-to-south configuration due to the magnetic dipole induced (μ) in a sheet of HOPG. The magnetic body force (fm) exerted by the magnets on the HOPG is a function of the magnitude of the gradient of the static field flux density (B) and the magnetic dipole $\left(f_m = \nabla(\mathbf{B}\cdot\mu)\right)$, (Taylor 2005). The magnetic potential energy stored in such a system is given by the

$$U_m = \int_V \mathbf{B}\cdot\mu\, dV, \qquad (2.1)$$

where the magnetic dipole moment is a function of the volume susceptibility (χ_m), a material property which gives a measure of the magnetic polarizability of a material. In the absence of a magnetic field, diamagnetic materials present no magnetic dipoles. Magnetic dipoles are only induced in the presence of a field and are aligned within opposition to the applied field. Susceptibilities for HOPG are on the order of -10^{-4}, in standard international (SI) units, and the differences between the

susceptibility perpendicular to the basal plane may be an order of magnitude higher than the susceptibility parallel to the plane. This anisotropy has been exploited in the past to calibrate lateral force atomic force microscopy cantilevers (Li 2006).

Levitation is attained when the magnetic potential energy is balance with the gravitational potential energy,

$$\frac{1}{\mu_o}\int_V \nabla\left(\mathbf{B}\cdot\boldsymbol{\chi}\cdot\mathbf{B}\right)dV = \int_V \rho g \mathbf{e}_2\, dV, \qquad (2.2)$$

where ρ is the mass density of the HOPG sheet and g is the gravitational acceleration constant. During the application of an external normal force, at a distance (l) from the cantilever-HOPG system, which disturbs this equilibrium, the D-NFC exhibits a restoring magnetic moment given by

$$\mathbf{M}_m = \frac{1}{\mu_o}\int_V \mathbf{x}\times\nabla_x\left(\mathbf{B}\cdot\boldsymbol{\chi}\cdot\mathbf{B}\right)dV, \qquad (2.3)$$

where $\mathbf{Y}$ (= $\mathbf{y}$ x $\boldsymbol{\Omega}$) is defined in figure 2.2 by the $\boldsymbol{y}$ position vector with respect to the center of mass (O) and $\boldsymbol{\Omega}$ is the rotation vector, and the term

$$\mathbf{F}_m = \frac{1}{\mu_o}\int_V \nabla_x\left(\mathbf{B}\cdot\boldsymbol{\chi}\cdot\mathbf{B}\right)dV, \qquad (2.4)$$

is the net magnetic force body force of the HOPG sheet under the influence of the magnetic field flux. The stiffness of the Si cantilever and HOPG sheet levitated body is given by the rate of change of the magnetic moment with respect to the rotation as;

$$\kappa_{ij}^m = \frac{\partial M_i^{(m)}}{\partial \Omega_j}. \qquad (2.5)$$

2.2.2 Unconstrained Vibration Characteristics of Device

The motion of the D-NFC is characterized as an unconstrained cantilever beam oscillation with a pinned end boundary condition. Therefore, the infinitesimal strain within the cantilever is zero, making the motion a rigid body rotation about the origin (*O*). The only damping (d_{33}) present is mainly due to inertial effects (low Reynolds numbers) due to the viscosity of air, on the order of 10^{-5} kg/s. The characteristic equation of motion for a damped oscillator is given (Appendix A) by

$$\ddot{\mathbf{\Omega}}_3 + 2\zeta\,\omega_n \dot{\mathbf{\Omega}}_3 + \omega_n^2 \mathbf{\Omega}_3 = 0, \qquad (2.6)$$

where ζ $(= d_{33} \big/ 2\sqrt{I_{33}\kappa_{33}^m})$ is related to the magnetic angular stiffness κ^m, $\boldsymbol{\omega}$ is the natural angular frequency $(= \sqrt{\kappa_{33}^m / I_{33}})$, the subscript ($n$) is used to denote the natural frequency of oscillation, and the number of dots over a variable represents the order of the time derivative of the same variable. A general solution for equation 2.6 above is given by $\mathbf{\Omega}(t) = e^{-\zeta \omega_n t}\left(C_1 \sin \omega_d t + C_2 \cos \omega_d t\right)$, where $\omega_d = \omega_n \sqrt{1-\zeta^2}$, C_1 and C_2 are both coefficients given by the initial conditions. Most importantly, for the D-NFC characterization the relationship between the natural frequency and the angular stiffness of the system is given by

$$\kappa_{33}^m = I_{33}\omega_n^2 . \qquad (2.7)$$

In order to calculate the magnetic stiffness of each D-NFC system at the point of contact with a specific distance (l) from the fulcrum, free vibration natural angular frequency measurements of a bare cantilever and a cantilever holding a glass bead at

l must be made. In such cases where the glass bead is placed in the cantilever, the angular stiffness of the system may be closely described by $\boldsymbol{\kappa}_0 = \mathbf{I}_0\omega_0^2$, where the moment of inertia is given by the moment of inertia of the cantilever, the glass bead, and the moment produced by the bead with respect to the cantilever center ($y_1 = 0$) as; $\mathbf{I}_0 = \mathbf{I} + \frac{2}{5}mR^2 + ml^2$.

Therefore, the ratio between the angular stiffness of the unloaded to the loaded D-NFC cantilever system, $\boldsymbol{\kappa}/\boldsymbol{\kappa}_0 = \mathbf{I}\omega^2 / \mathbf{I}_0\omega_0^2$; assuming that $\boldsymbol{\kappa} \sim \boldsymbol{\kappa}_0$, provides an expression for the angular stiffness ($\boldsymbol{\kappa}$) with respect to measurable quantities given by

$$\boldsymbol{\kappa} = \frac{m\left(2R^2 + 5l^2\right)\omega^2\omega_0^2}{5\left(\omega^2 - \omega_0^2\right)}, \qquad (2.8)$$

where *m* is the mass of the borosilicate bead, *R* is the radius of the bead, ω_n is the angular frequency of the cantilever bar without the glass bead, and $\boldsymbol{\omega_0}$ is the angular frequency of the cantilever bar with the glass bead placed on it and a distance *l* from the center of the bar (figure 2.2). The moment caused by the glass bead is given as the product of the force (f) and the distance (l) from the center of rotation as well as the product of the angular stiffness (α) and the angle of rotation (θ) of the cantilever bar as follows;

$$\mathbf{f}l = \boldsymbol{\kappa}\theta = \boldsymbol{\kappa}\frac{\delta_{y_1=l} - \delta_{y=0}}{l}, \qquad (2.9)$$

where δ is the cantilever displacement at the point of contact ($y_1 = l$) and the fulcrum ($y_1 = 0$). The displacement at the fulcrum is a function of the normal magnetic stiffness (κ_n) of the system. Limiting the size of the diamagnetic graphite sheet

reduces the ratio of the normal stiffness to the angular stiffness. Therefore, assuming most of the displacement occurs at the point of contact ($\delta_{y1=0} = 0$), along with some algebraic manipulation the stiffness of the system is given by

$$\mathbf{k}_{ref} \approx \frac{\mathbf{f}}{\delta_{y_1=l}} = \frac{\boldsymbol{\kappa}}{l^2}. \qquad (2.10)$$

2.3 Materials and Methods

A photo-detector was use in order to convert the laser light information reflected from the oscillating D-NFC cantilever into a voltage output signal that was recorded using a U9-Labjack data acquisition unit (LABJACK, Lakewood, CO). With the goal of studying the effects of water condensate on the stiffness of the D-NFC system frequency, measurements of an uncoated cantilever were compared to measurements of a cantilever which was coated with a fluoropolymer in order to render it hydrophobic (contact angle > 90º).

2.3.1 Contact Angle Analysis

The images of a sessile drop of de-ionized distilled water were captured using a high precision Q-Imaging Retiga 2000R charge-coupled device (CCD) camera (Q-Imaging, Inc., Surrey, BC, Canada). A MATLAB technical computer language instrument control code was used to control the CCD camera and analyze the images by fitting curves to the solid and liquid surfaces of the drop-solid surface contact and the angle between the tangent lines intersecting points in the surface was take in the triple line region.

2.3.2 Bead Characterization

A borosilicate bead (Duke Scientific Co., Palo Alto, CA) with a measured diameter of 536 ± 6 μm was used for the frequency shift measurements as described below. The same imaging arrangement described above for the contact angle measurements was use in order to record an image for each bead. A MATLAB technical language computer algorithm was also used to analyze images from a CCD camera with known pixel size and extract glass bead diameters. The bead diameter was used along with the density of borosilicate glass in order to calculate the mass for each bead.

2.3.3 Environmental Control

An environmental chamber was use in order to control the relative humidity during the experiment. All experiments were conducted at room temperature (21ºC) and with a relative humidity ranging from 25% to 58%. Dry nitrogen (N_2) supplied from a tank was used in order to replace the air inside the chamber with dry gas. Experiments were also conducted by increasing the relative humidity by one percent units using a water/salt bubble bath inside the chamber and monitoring the RH sensor (Vaisala HM 34, Vaisala, Inc.) placed inside the chamber. Control of the RH was repeatable and possible for an unlimited amount of time. A computer fan was adapted with a variable voltage supply in order to completely mix the air inside the chamber. A Goldberg-type placement device was constructed to place the bead on the cantilever in a controlled manner. This experimental system allowed single-digit relative humidity control.

2.3.4 Dynamic Measurement of Stiffness

The oscillatory response of the D-NFC system was measures both with and in the absence of a glass bead placed at the indentation position for calibration. The response of a photo-detector to the laser reflected from the oscillating D-NFC cantilever was recorded. A MATLAB technical computer language algorithm was written in order to analyze the recorder response signal. A fast-Fourier transform analysis was performed in order extract the power spectrum of the output signal gathered for each sampled oscillation. The value of the frequency corresponding to the highest power amplitude, namely the main frequency component of the power spectrum, was extracted as the natural frequency of the corresponding mode of oscillation (figure 2.3 bottom). The top of figure 2.3 shows how the values thus extracted were used to fit a curve for the response of a simple harmonic oscillator model (Kinsler 2000).

2.3.5 Static Measurement of Stiffness

The displacement of the D-NFC cantilever as a result of placement of a glass bead on the indentation position was recorded with a high resolution charge-coupled device (CCD) camera (Q-Imaging, Inc., Surrey, BC, Canada). A MATLAB technical computer language algorithm was written in order to analyze the recorded displacement with a resolution of 10.45μm.

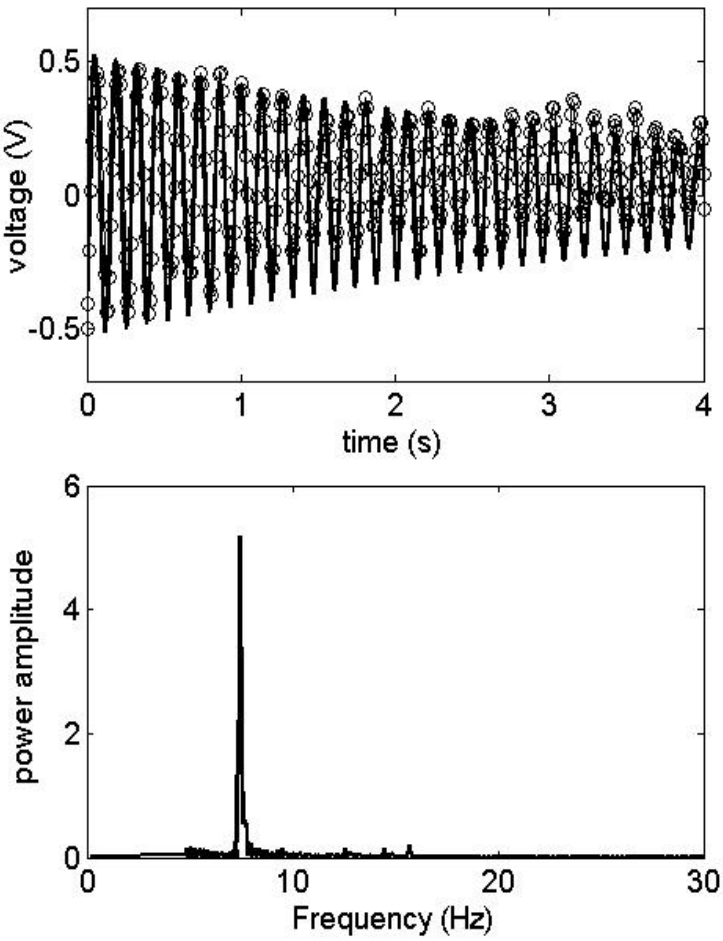

Figure 2.3 Raw data (above) and power spectrum (below) from the photo sensor signal collected during free vibration of the D-NFC levitated mass.

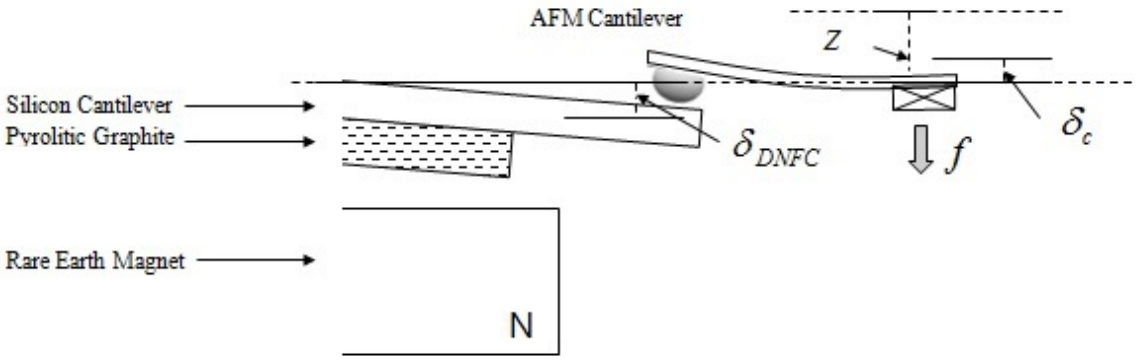

Figure 2.4 Diagram of AFM cantilever and D-NFC contact during calibration measurement.

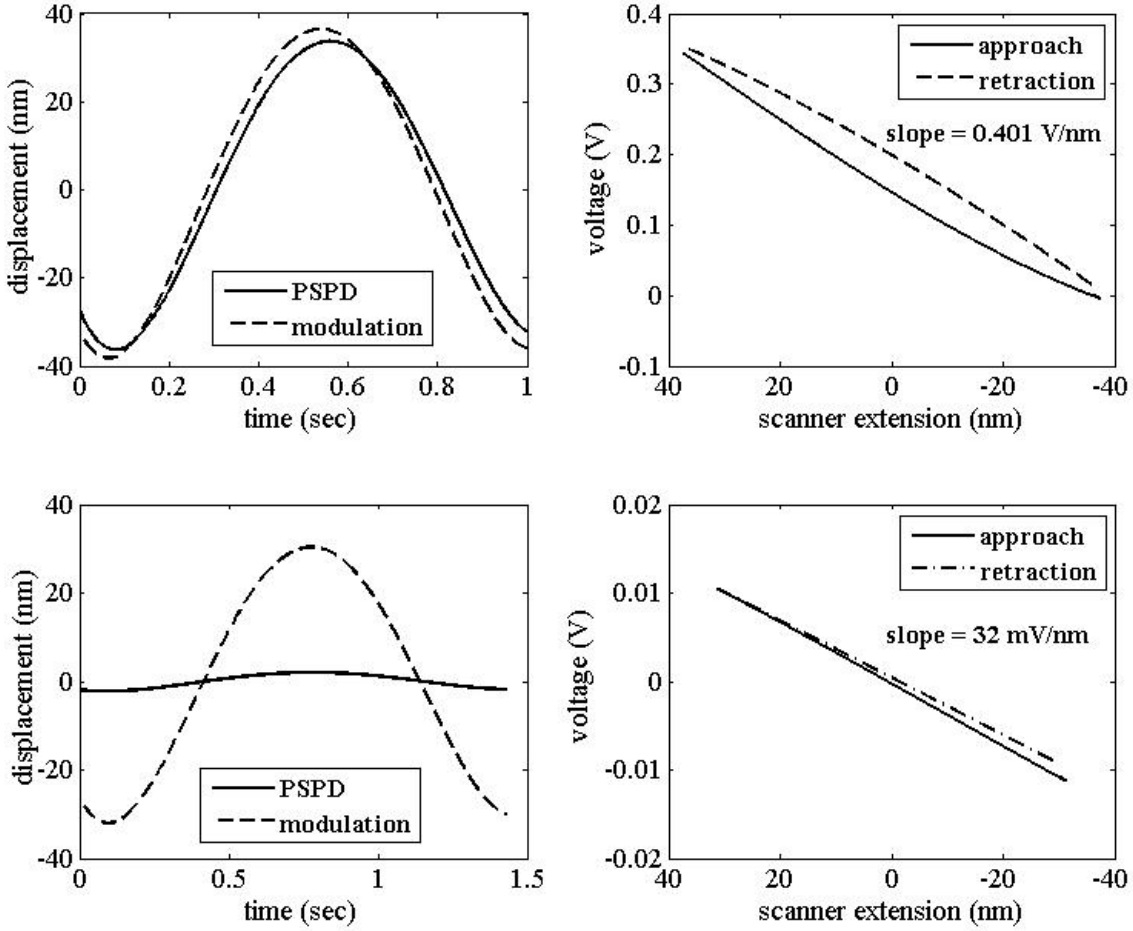

Figure 2.5 Atomic force microscope position sensitive photodetector (PSPD) output for AFM cantilever contact with calibration grid (top) and D-NFC cantilever (bottom).

2.3.6 AFM Calibration Methodology

The voltage as a function of distance is recorded by making contact with the AFM cantilever in the same spatial position where the glass bead was placed during the measurements for the D-NFC system stiffness characterization (figures 2.4 and 2.5). In order to characterize the response of the position sensitive photodiode

(PSPD) a measurement of the cantilever force as a function of distance (f vs. d) curve is generated by applying a force against the surface of a standard Silicon wafer (stiff) calibration grid. The slope of this curve is used to gauge the sensitivity of the system, which is used to calculate the calibrated stiffness with the following relationship;

2.3.5 Static Measurement of Stiffness

The displacement of the D-NFC cantilever as a result of placement of a glass bead on the indentation position was recorded with a high resolution charge-coupled device (CCD) camera (Q-Imaging, Inc., Surrey, BC, Canada). A MATLAB technical computer language algorithm was written in order to analyze the recorded displacement with a resolution of 10.45μm.

$$k_c = k_{ref} \frac{z - \delta_c}{\delta_c} \qquad (2.11)$$

where k is the stiffness for the AFM probe cantilever (subscript c) and the D-NFC system (subscript ref), z and δ_c are the AFM piezoelectric scanner and cantilever displacements, respectively. The calculation outlined here follows the rationale described by Torii *et al.* (Torii 1996). In practice the data gathered with the AFM must first be calibrated to the sensitivity of both the piezoelectric factor characteristic of the lead-zirconate titanate (PZT) scanner and the position sensitive photo diode (PSPD).

2.3.7 Uncertainty Propagation Analysis

The uncertainty of the D-NFC system was calculated by using a root-sum of the squares method (RSS) (Figliola 1995) expressed as

$$u_{\kappa} = \pm\sqrt{\sum_{i}^{K}\left(\theta_{\varepsilon}u_{\varepsilon}\right)_{i}^{2}}, \qquad (2.12)$$

where the uncertainty for each step of the D-NFC characterization is weighted by a sensitivity factor $\left(\theta_{\varepsilon} = \partial\alpha/\partial\varepsilon\right)$, which also converts each uncertainty to the appropriate dimensional units. Here the measurement step uncertainty of the average value of each measurement is given by the quotient product of the standard deviation (*std*) and the squared-root of the number of trials (*N*) of said measurement ($u_{\varepsilon} = std_{\varepsilon}/\sqrt{N}$). The explicit expression for the sensitivities is given in Appendix B.

2.4 Results and Discussions

2.4.1 D-NFC Device Characterization

The characteristics of several D-NFC devices are summarized in table 2.1. The angular frequencies (ω_n) of the devices ranged from 46.94 ± 0.54 to 88.46 ± 0.47 rad/s, with stiffness ($\kappa^m{}_{33}$) ranging from 8.1 ± 1.6 to 28.8 ± 8.2 mN/m. The damping coefficient (ζ) of these devices is within the range of 0.48 ± 0.19 to 2.1 ± 0.25, with effective drag coefficients (d_{33}) of $4.79\text{x}10^{-2}$ ± $1.91\text{x}10^{-2}$ to $10.11\text{x}10^{-2}$ ± $1.14\text{x}10^{-2}$ mkg/s. The higher damping coefficient associated with the D-NFC1 device originates from its larger projected area for the HOPG sheet (see dimmensions in 2nd column). Comparison between the static and dynamic measurements of the angular stiffness

shows the discrepancy arising from the effects a relatively low normal stiffness. Due to the competing angular (κ) and normal stiffness (κ_n) of the dimensions of the graphite and cantilever must be carefully optimized as $\kappa << \kappa_n l^2$, to make the displacement at the fulcrum negligible (equation 2.9). The analysis of error propagation performed using equation 2.12 and equations B.1-B.4 shows an uncertainty in the angular stiffness measurement (u_α) approximating ± 1.36x10^{-2} mN·m and an uncertainty in the D-NFC system stiffness (u_κ) as low as ± 1.6 mN/m.

Table 2.1 D-NFC devices dimensions and dynamic characteristics.

Specimen	PG Sheet Dimensions (mm)	Mass (mg)	Cantilever Dimensions (mm)	ω (rad/s)	ω_0 (rad/s)	ζ	k_{stat} (mN/m)	k_{dyn} (mN/m)
D-NCF 1	3.79 x 4.55 x 0.41	18.0	4.05 x 1.00 x 0.29	88.72 ± 0.47	86.46 ± 0.47	2.1 ± 0.25	42.4 ± 10.6	28.8 ± 8.2
D-NFC 2	2.71 x.3.45 x 0.50	15.8	4.64 x 1.24 x 0.29	52.16 ± 0.19	49.85 ± 0.38	0.19 ± 0.05	10.6 ± 0.66	8.2 ± 1.6
D-NFC 3	2.87 x 3.70 x 0.55	16.6	4.72 x 0.92 x 0.29	47.17 ± 0.19	45.82 ± 0.19	0.48 ± 0.19	8.6 ± 0.33	8.7 ± 1.8

2.4.2 AFM Cantilever Calibration

In order to calculate the sensitivity of the of the PSPD (S_g), the slope of the voltage as a function PZT scanner displacement (V_m) is recorded while the AFM cantilever is in contact with a silicon calibration grid (Veeco Metrology, Santa Barbara, CA). A measurement of voltage as a function of displacement is recorded for the AFM cantilever during contact with the D-NFC device and its slope (S_{DNFC}) is

taken as the sensitivity of the calibration measurement. The calibrated cantilever stiffness (k_c) in terms of calibration variables and signals is given by

$$k_c = k_{ref} \frac{V_m * S_g - V_{PSPD} * S_{DNFC}}{V_{PSPD} * S_{DNFC}}. \qquad (2.13)$$

Table 2.2 Stiffness constants for AFM cantilever calibrated with the D-NFC system.

Specimen	Contact Type	Coating Type	Nominal k (N/m)	D-NFC Technique k (N/m)	Cleveland Technique[1] k (N/m)	% error
12NSC18	Si Tip	Al	3.5 ± 0.4	1.784 ± 0.010	2.145 ± 0.065	(15)
13NSC18	Si Tip	Al	3.5 ± 0.4	1.408 ± 0.017	2.246 ± 0.068	(53)
16NSC18	Si Tip	Al	3.5 ± 0.4	3.072 ± 0.030	4.321 ± 0.130	(35)
18NSC18	Si Tip	Al	3.5 ± 0.4	2.272 ± 0.001	1.252 ± 0.037	45

Specimen	Dimensions (μm)	Quality Factor	f_0 (kHz)
12NSC18	219.2 x 35.4 x 2.0	355	69.73
13NSC18	218.3 x 35.8 x 5.0	442	70.84
16NSC18	237.8 x 35.0 x 4.0	371	81.48
18NSC19	203.5 x 33.1 x 3.1	306	65.20

Figure 2.4 shows the calibration process graphically. Figure 2.5 (top left shows the displacement as a function of time of both the scanner and AFM cantilever during contact. The PSPD voltage as a function of scanner displacement is shown in top right of figure 2.5. Similarly the bottom right and left graphs of figure 2.5 show the respective curves for AFM cantilever during contact with the D-NFC device. As described above, the uncertainty in the D-NFC stiffness measurements is on the order

of 1.0 mN/m, which achieves a theoretically minimum calibration error of 0.1%. The additional measurements steps associated with the final calibration of the AFM cantilever contribute an uncertainty to the overall calibration measurement. Table 2.2 shows the values for AFM cantilevers calibrated with the D-NFC system and the comparisons with manufacturer (Nominal) reported values, as well as those of two commonly used method by and Cleveland *et al.* (Cleveland 1993).

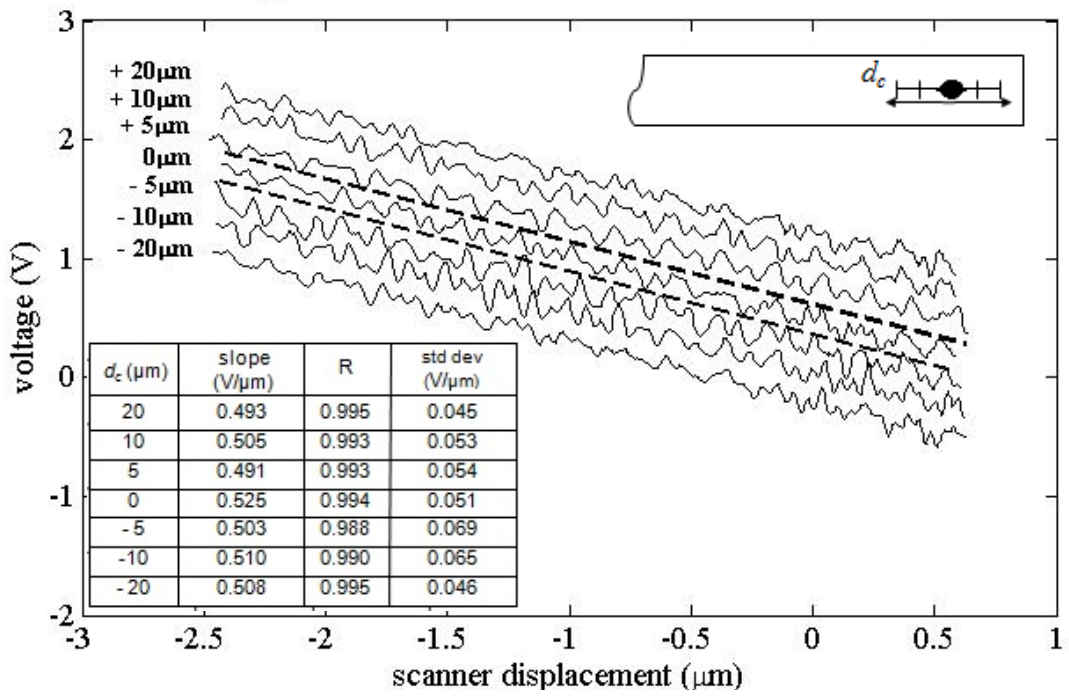

d_c (µm)	slope (V/µm)	R	std dev (V/µm)
20	0.493	0.995	0.045
10	0.505	0.993	0.053
5	0.491	0.993	0.054
0	0.525	0.994	0.051
-5	0.503	0.988	0.069
-10	0.510	0.990	0.065
-20	0.508	0.995	0.046

Figure 2.6 PSDP voltages as function of distance AFM cantilever and D-NFC contact position relative to the D-NFC indentation. Notice the stability of the slope values for a range of 30µm away from the center of the indentation in the direction of the positive and negative y-coordinate.

2.4.3 Effects of AFM Cantilever and D-NFC Contact Position

Figure 2.6 shows typical PSDP voltage as a function of AFM PZT scanner displacement measurement during contact with the D-NFC cantilever in the center of

the indentation position, along with the curves for contact ± 5μm, 20μm and 30μm along the y_1-axis. The average slope based on these contact positions is 0.505 ± 0.011 V/m. It may be seen from the inset in figure 2.6 that the variation in stiffness of the D-NFC as a function of bead position is negligible.

2.4.4 D-NFC Sensitivity to Relative Humidity

In order to assess the sensitivity of the stiffness of the D-NFC reference to the water in the environment a series of stiffness measurements where done under varying relative humidity (RH). A cantilever coated with a hydrophobic polymer was used as control. Contact angle measurements confirmed the deposition of the fluoropolymer on the initially hydrophilic cantilever surface. Measurements yielded contact angles of 68º and 101.7º for the uncoated and coated Si cantilevers, respectively. The diameter and mass of the bead used in the uncoated cantilever measurements were 581μm and 81μg, respectively. While the diameter and the mass for the bead used with the coated cantilever were 412μm and 226μg, respectively.

The frequency as a function of RH for Si cantilever uncoated shows some oscillatory behavior and barely noticeable shift due to the addition of the glass bead mass. This oscillation is attenuated for the cantilever coated with hydrophobic polymer and reappears for the coated cantilever with the added glass bead mass likely due to the glass bead not being coated. Nevertheless, the shift is noticeably towards a lower frequency as expected due to the added mass. The uncoated cantilever exhibited average frequencies of 7.969±0.449 Hz and 8.0827±0.535 Hz with and without the mass, respectively. The coated cantilever exhibited average

frequencies of 8.493±0.501 Hz and 7.553±0.752 Hz for the bare cantilever and the cantilever with the added glass bead mass, respectively. In the case of the uncoated cantilever, an increase in D-NFC cantilever stiffness after bead placement is due to the increased hydrophilic surface area provided by the hydrophilic borosilicate bead. This increase in stiffness was not exhibited by the D-NFC with a coated cantilever and bead.

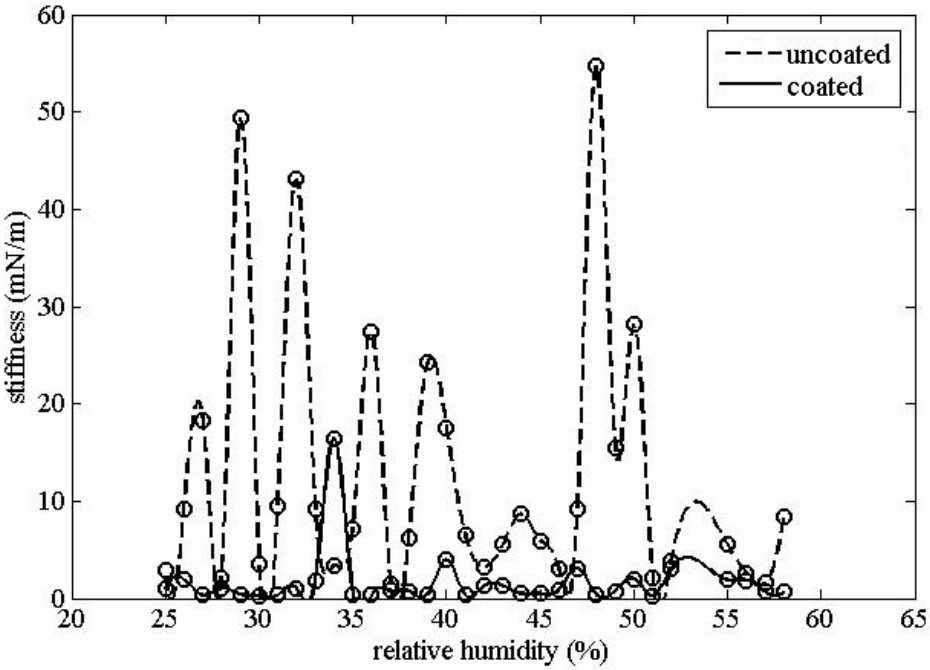

Figure 2.7 D-NFC cantilever stiffness as a function of relative humidity for uncoated (blue) and coated (black) Si wafer cantilevers shows water borne variability. This device is suitable for the study of surface water molecular structure.

The stiffness of the D-NFC systems varied predictably with the environmental relative humidity (figure 2.7). The stiffness of the uncoated system oscillates due to the collection of water on the surface of the cantilever. As water collects in the surface it forms a layer of random molecules that exhibit diamagnetic behavior, thereby adding repulsion to the cantilever, which in turn increases the stiffness. As

water continues to coalesce in the surface, paramagnetic ice-like water may forms which allows for a reduction in the diamagnetic repulsion and stiffness alike. In a crystal structure the water ions are far enough to make the mutual interaction energy due to magnetic moment interlattice effects negligible compared to the energy due to the external magnetic field. Therefore, the ice-like sheet of water behaves paramagnetically (Asay 2005).

2.5 Conclusion

As demonstrated by the error propagation analysis, the D-NFC provides an approximate milli-Newton per meter of displacement accuracy on a single Newton per meter of displacement level calibration, which translates into less than 0.1% (.061%) error. This is the most accurate method yet for AFM normal force measurements. Most of the current techniques for normal force calibration rely on material isotropy assumptions, which are not appropriate for epitaxially grown silicon-based crystalline materials with dimensions at the micrometer scale. Surface roughness, difficulty achieving dimensional uniformity and material defects will also produce error sensitivity beyond what is acceptable for forces at the nano-Newton level. A cursory inspection of current stiffness calculation methods in the literature shows error sensitivity to density, frequency and length measurements. Newer reference cantilever calibration techniques have provided an improvement in accuracy, but are very sensitive to reference cantilever beam design calculations of stiffness, which can be difficult to fabricate. The D-NFC device provides a cost effective calibration technique that can be fabricated with inexpensive laboratory

materials, without the use of high resolution microscopy in order to make cantilever dimensional measurements.

The D-NFC system also provides a platform for single-molecule measurements akin to mass-balance systems. The role of the structure of water in intermolecular interactions and surface force fields may be studied using chemically functionalized coatings.

Chapter 3.0: Measurements of Hierarchical Wrinkle-inducing Graded Bulk Modulus on UV/Ozone Treated PDMS Substrate

Abstract

This chapter presents the atomic force measurements (AFM) of the stiffness of elastomeric material treated with UV/Ozone radiation. It is here further shown that upon oxidation the material develops multilayer systems which includes a zone with graded stiffness. Experimental measurements revealed that these multilayer systems form free-surface nested wrinkles with wavelengths that span different orders of magnitude. A linear bifurcation analysis revealed that the multi-scale wrinkling behavior observed is mainly due to elastic mismatch at the different interfaces of the composite structures.

3.1 Introduction

Buckling phenomena of thin, stiffer films on compliant substrates, known as bilayer systems, have received increasing attention due to the ease of manufacture of engineering multifunctional structures, where the surface patterns are controllable. Biot produced a treatment on such stiff films embedded within viscoelastic media (Biot 1957). He described the parametric characterization of the folding instability produced by the critical compressive strain between a film, embedded within other

viscoelastic media. Using a modified constitutive model for the material along with perturbation analysis and a momentum equation earlier developed under initial stress framework (Biot 1938) the relationship to predict the dominant wavelength was given as a function of the film thickness and mismatch in moduli. More recently, Sun showed using a perturbation analysis under a finite deformation framework, that evolution of one-dimensional sinusoidal surface topographical contours, known as wrinkles, formed at the surface of the bilayer system due to buckling when compressed beyond a critical strain level. The stable wavenumber wrinkle bifurcated configuration was determined from instabilities of a particular path of deformation by finding the nontrivial solutions to the linearized system of equations with the imposed boundary conditions (Sun 2011). More importantly, the morphological evolution of the wrinkles, such as period doubling, was studied as a function of finite pre-strain on these bilayer systems. The key factor of this instability phenomenon is the mismatch in the elastic moduli at the interface between the two adjacent material layers, along with the finite level of the deformation.

In addition to the formation of wrinkles at a given length scale, hierarchical self-nested wrinkles have been reported (Efimenko 2005). Efimenko's group showed self-nested wrinkles with wavelengths that range from 50 nm to few millimeters. Self-nested wrinkles are a distinct feature from sequential period-multiplying instabilities found in bilayer systems.

In the present work, elastic instability of an elastomer treated with UV/Ozone is analyzed using a hybrid experimental and analytical approach. It is here shown that exposure of pre-strained elastomeric materials to UV/Ozone radiation will cause

the formation of multiple layers with differing stiffness under the free surface. The existence of multiple layers within the substratum was found to have been produced after irradiation.

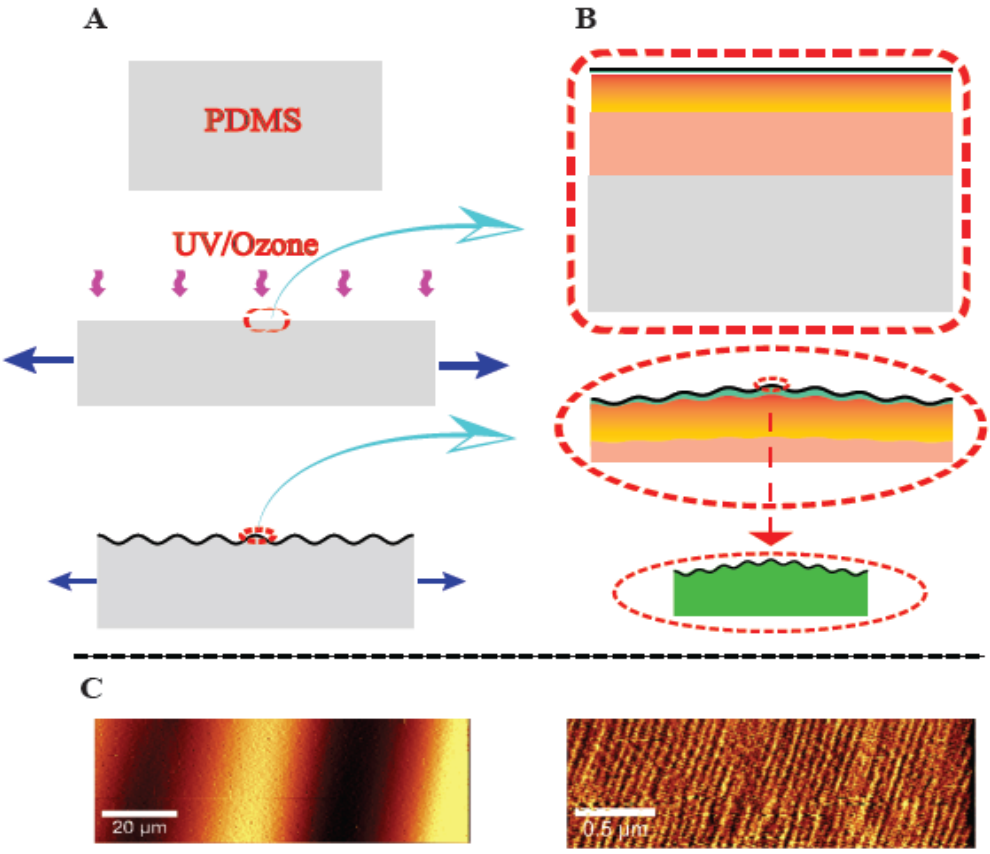

Figure 3.1 PDMS UV/Ozone wrinkled surface fabrication schematic. After casting, PDMS is pre-strained and then irradiated with a UV light in the presence of ozone (A), thereby forming a multilayer system of SiO_x and polymer complex (B), with a thin stiff glass film on the free surface followed by softer, graded layers with interfacial moduli step changes. Upon strain release, a multi-scale wrinkle formation (C) may be observed at the free surface in the AFM topography images.

A layer with exponentially decaying elastic modulus along with a number of step changes in modulus where found to govern the mechanisms of nested-wrinkle formation. The linearized buckling perturbation analysis described by Diab *et. al.* (2014) was employed to show that multiple length scales of the stiffness structures

give origin to the surface periodic contours characterized by several wavelengths and that these wavelengths will appear with the same loading conditions as a function of the ratio of the moduli at each interface.

3.2 Experiments

3.2.1 Sample Preparation

All the experiments were performed using poly(dimethyl siloxane) (PDMS) samples prepared by mixing silicone elastomer base and curing agent (Sylgard 184, Dow Corning, OH) at the weight ratio 10:1. The solution was degassed in a vacuum chamber at -27 Hg for 20 minutes, until visible bubbles were removed and then cured in an oven at 85℃ for 6 hours. Following curing, the samples were deformed with a prescribed pre-strain and placed in a UV/Ozone chamber (Novascan PSD-4) that operates at the ambient pressure and room temperature (figure 3.1). The chamber consists mainly of a low-pressure mercury vapor lamp that emits energy at two wavelengths, 184.9 nm and 253.7 nm. First, atmospheric Oxygen molecules dissociate at 184.9 nm and then react with O_2 to form Ozone (Ouyang 2000). Ozone absorbs strongly at 253.7 nm to dissociate into atomic oxygen that reacts with the organic portions of the polymer to form volatile fragments of low molecular weight like CO_2 and H_2O.

3.2.2 Wrinkling of UV/Ozone Treated PDMS

In addition to the unstrained samples produced for bulk measurements, some PDMS samples were stretched using a custom-designed loading device, before

irradiation in the UV/Ozone chamber for varying exposure time between 60 and 240 minutes. The distance between the mercury lamp and the sample was set as 5mm and thus the properties of the layers are a function of the exposure time to the UV/Ozone. After removal from the chamber, the sample pre-strain was released slowly to maintain quasistatic conditions. An optical microscope calibrated with a stage micrometer was used to measure the wavelength and amplitude of the wrinkle pattern on the modified surface of the PDMS. These measurements were supplemented with topographic studies in the AFM at nanometer scales. The evolution of the wave characteristics of the wrinkles as a function of UV/Ozone exposure time is discussed in Appendix C.

3.3 Measurements and Discussion

3.3.1 AFM Measurements of the Material Stiffness

The stiffness of a PDMS sample treated with UV/Ozone was measured using the atomic force microscopy (AFM), Dimension 3100 with Nanoscope IIIa controller (Veeco Metrology, Inc., Santa Barbara, CA), in the pulse force mode (PFM) (Krotil 1999). For an overview of the pulse force mode see Appendix D. The PFM allows for the material characterization of soft matter without disrupting its structural integrity by accessing feedback signals with a digital data acquisition (WITec GmbH, Ulm Germany). The two different cantilevers used were a silicon nitride sharp cantilever to obtain high-resolution images of the coating free surface, and a fabricated borosilicate colloidal probe cantilever that permits a theoretical estimation of the mechanical properties. The cantilever was calibrated using the normal force

calibration method described in Chapter 2. A PFM scan of the cross-section was conducted to measure the stiffness in order to assess the cross-sectional compositional morphology of the substrate. The data for the maximum adhesive force was extracted from the curve of the force as a function of distance between the contacting surfaces generated in the PFM measurements (Appendix E). The zero-load adhesive force (P_o) exhibited in an elastic contact between a sphere of radius R_S and a flat surface ($R_F = \infty$) was first derived by Johnson *et. al*. (1971) and is given by $F = 1.5\pi R\gamma$* where R is the effective contact radius ($1/R = 1/R_F + 1/R_S$) and γ is the work of adhesion. The contact stiffness is calculated by measuring the force (P) exerted on the AFM cantilever (figure D.1, bottom left) by the substrate during colloidal probe penetration (δ), given by $k_c = P/\delta$ (figure D.1, top left).

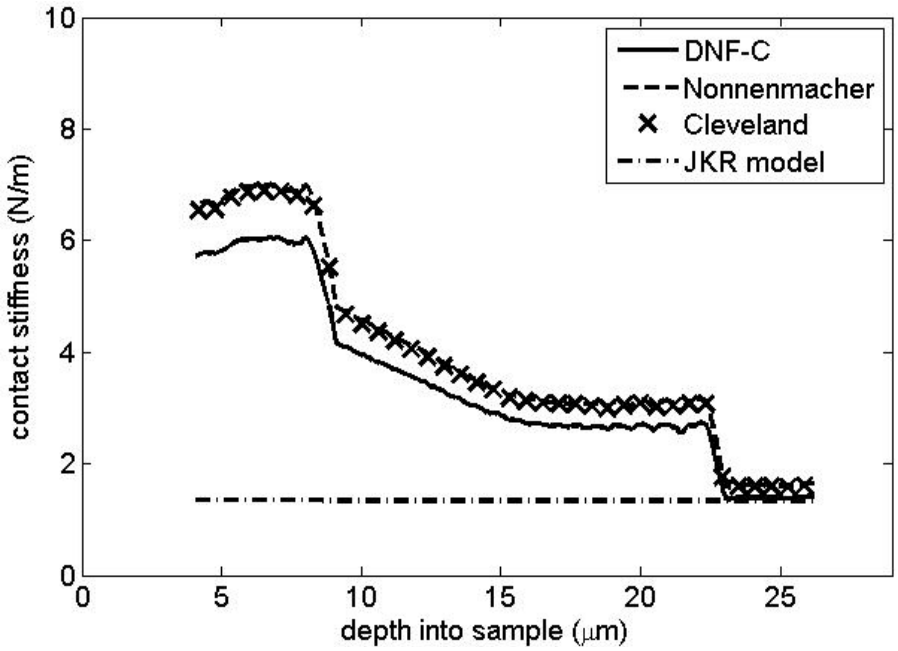

Figure 3.2 D-NFC calibrated data for UV/O_3 surface irradiated PDMS contact stiffness as a function of depth (solid line) compared to calculated contact stiffness using two other leading calibration methods by Cleveland and Nonnenmacher, along with the contact stiffness for PDMS estimated with the JKR model.

In order to calculate accurate values for the elastic modulus mismatch, between layers, used in the linear bifurcation method to predict the nested wrinkles wavenumbers observed during strain release, the D-NFC calibration method was employed. The calculation of the contact stiffness from the AFM measurements using the cantilever stiffness calibrated with the D-NFC device, was compared to calculations using two other leading calibration methods (Nonnemmacher 1991, Cleveland 1993). Calculations of contact stiffness using a calibrated cantilever show (figure 3.2) the D-NFC calibration method with a better fit when compared to the Johnson-Kendal-Roberts model prediction for the PDMS modulus (figure 3.2, cut line) (Johnson 1971).

The calculation of the contact stiffness from the AFM measurements using the cantilever stiffness calibrated with the D-NFC device, was compared to calculations using two other leading calibration methods (Nonnemmacher 1991, Cleveland 1993). Calculations of contact stiffness using a calibrated cantilever show (figure 3.2) the D-NFC calibration method with a better fit when compared to the Johnson-Kendal-Roberts model prediction (figure 3.2, cut line) (Johnson 1971).

The effective modulus of elasticity of the contact was calculated from the JKR model as;

$$E^* = \left\{ \frac{27}{8} \frac{R}{k_c^{\,3}} \left[P + 3\pi\gamma R + \left(6\pi\gamma^* RP + \{3\pi\gamma R\}^2 \right)^{1/2} \right] \right\}^{1/2}, \quad (3.1)$$

where the relationship between the effective modulus at the borosilicate probe and PDMS is given by, $E_p = 4/3((1-\nu_p^2)/\pi^2)E^* - ((1-\nu_p^2)/(1-\nu_g^2))E_g$.

As shown in figure 3.3, the Young's modulus as a function of depth reveals that the oxidized PDMS sample develops several distinct zones near the surface with different mechanical properties. A thin stiffer layer at the free surface with a thickness on the order of 0.01μm (figure 3.3, top left**)**, followed by a thicker modulus depleted zone (thickness ~ 0.4μm) composed of multi-layers with lower Young's modulus. Below this softer zone, there is a zone with modulus that decreases exponentially as

$$E(X_2) = E_{2o}\left\{(1-\eta)\, e^{\,a\,(X_2 - h_0 - h_1)} + \eta\right\}, \quad (3.2)$$

where η ($= E_{2o}/E_{2i}$), with a range of values $0 < \eta < 1$, is the ratio of the shear modulus at the surface closer to the free surface (E_{2o}), to the shear modulus closer to the bulk material (E_{2i}), and a represents the reciprocal of the decay length of the modulus. The modulus varies by one order of magnitude (50 – 4.5MPa) from a depth of 0.5 to 8μm from the free surface (figure 3.3, top right). In this exponential zone the reciprocal of the characteristic decay length (a) is measured as 1.72 μm^{-1}. A stepwise decrease (figure 3.3, bottom right), in modulus, to 2.75MPa occurs at a depth of 8μm with a further monotonically decreasing modulus, which plateaus to 1.5MPa at a depth of 16μm. The modulus then finally shows a stepwise decrease to an approximate 1MPa modulus at 22μm in depth.

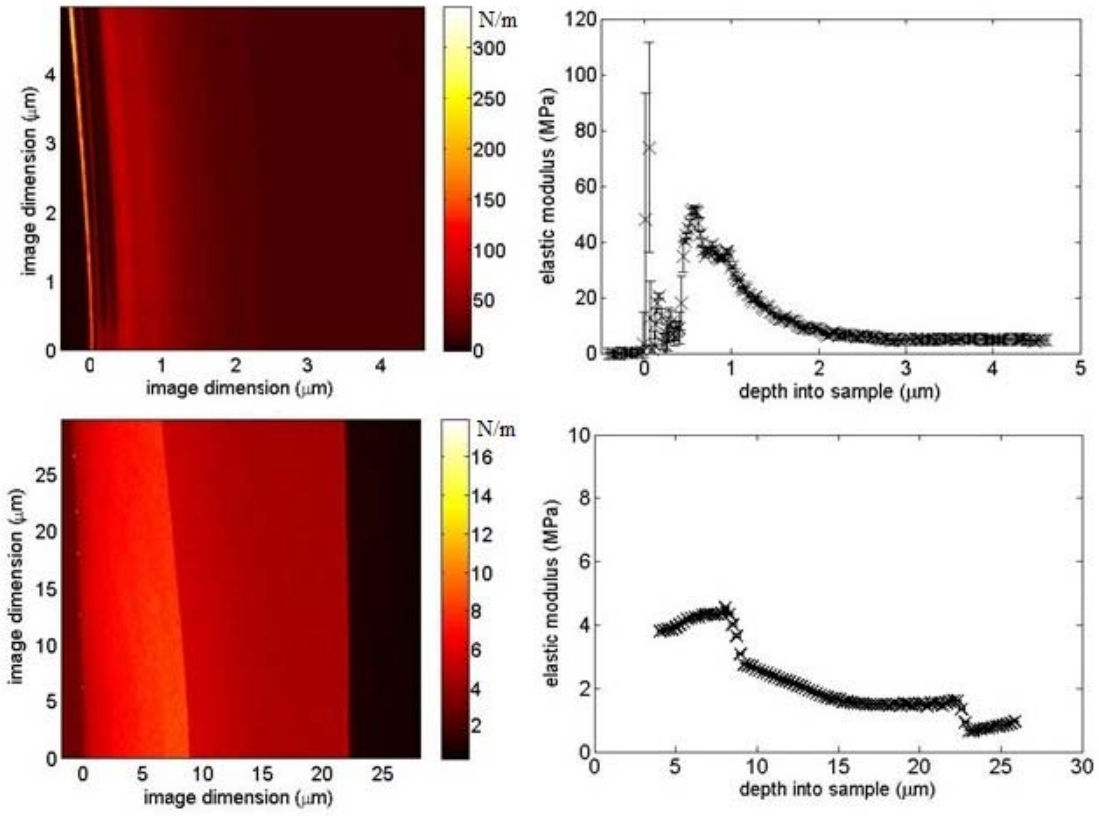

Figure 3.3 PFM measurements of Young's modulus of the oxidized PDMS as a function of depth from the free surface.

Chen et. al., has suggested that as the polymer is treated, with UV radiation in the presence of ozone, two regions near the surface with different oxidation rates form (Chen 2007). A surface zone with high oxidation rate leads to the progressive formation of silica-like (SiO_x) layer with thickness that ranges between 7 nm and 160 nm depending on the treatment conditions. This SiO_x layer constitutes a barrier that hinders further diffusion of oxygen towards the bulk material and thus producing a second zone with lower oxidation rate. This is in accord with the stiffness measurements that reveal a zone near the surface, where crosslinks are broken but the lack of available oxygen produces stiffness depletion. This is followed by a deeper zone where multiple layers of intermediate PDMS and SiO_x composition

forms characterized with graded and stepwise changes in modulus, at a depth from the thin stiffer layer at the free surface.

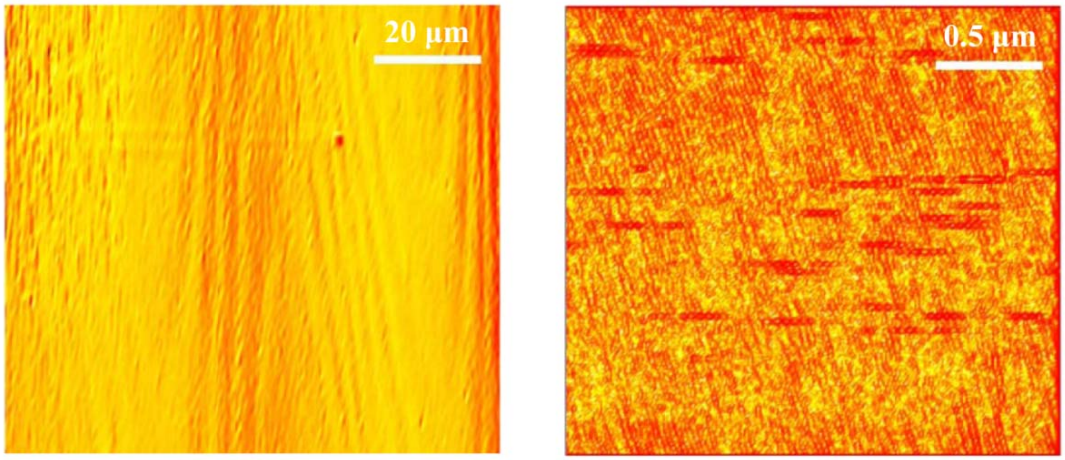

Figure 3.4 Topographic AFM image of fully released PDMS after UV/ozone treated. The same sample exhibits wrinkles with an approximate wavelength at the range of 50µm with nestled wrinkles with wavelengths on the order of 6-10µm (left) along with wavelengths at the nanometer scale (right, L = 70nm) nested within the 10µm wrinkles.

The lower modulus layer between the zones, at a depth from 0.1 to 0.5µm, may have formed as a consequence of the abrupt modulus mismatch of several orders of magnitude between the two zones near the surface. It has also been suggested that this intermediate zone with lower Young's modulus may be due to the gradual migration of low molecular weight or uncrossed-linked polymeric chains from the bulk material to the surface as the polymer ages after casting (Hillborg 2004, Chen 2007).

3.3.2 Wrinkling Characterization of UV/Ozone Treated PDMS

Using atomic force microscopy (AFM), the morphology of the fully released PDMS is shown in figures 3.4, left and 3.4, right. An areal power spectral density

(APSD) analysis was conducted by performing a 2-dimensional fast Fourier Transform decomposition of the AFM topographical data in order to extract the main features of the wrinkle morphology (Appendix F). These topographical measurements revealed multi-scale self-nested wrinkles with wavelengths ranging from 70 nm to 60μm.

3.4 Wrinkling Analysis of the Composite Structure

As shown in the previous section, elastomeric material treated with UV/Ozone radiation develops multi-layers with modulus that vary with depth from the free surface. In this section, the treated material is modeled as a multilayered structure with three distinct zones. The top layer consists of a stiff silica-like layer of thickness *t,* followed by a composite thicker layer with randomly varying modulus and thickness *h*, underneath which there is a zone with smoothly decaying modulus.

3.4.1 Linear Perturbation Analysis

In the model the three layers are assumed to undergo the same uni-axial plane strain compression in a direction parallel to the surface. The modulus of the free surface discreet layer is treated with an uniform profile, and the depleted layer is treated as a composite, while the stiffness of the zone with graded modulus is model as in equation 3.2. An additional layer step change in modulus was modeled at depth of 10um. The silica-like layer with thickness *t* was modeled using the beam layer theory as done by Shield et al. (1994). The incompressible neo-Hookean model is adopted for the intermediate zone with depleted elasticity and the deep substrate. The

AFM measurements of the Young's modulus presented in (figure 3.3) are used as properties to solve for the wavenumber ($k = 2\pi / L$) as a function of the critical strain. The analytical modeling and numerical analysis developed by Diab 2014, *et. al*., was used to solve the linear bifurcation problem of the multilayer system (figure 3.5). A linear bifurcation analysis was conducted for each mismatching interface modeled as a the multi-layer composite structure to obtain the wavenumber and critical strains for wrinkling, with a subsequent asymptotic matching calculation (figure 3.5, cut line) to match the solutions for all of the layers. Then, a finite element analysis was conducted to validate the linear bifurcation results. For the top layer (figure 3.5) only models the silica layer, which was treated using beam theory with coupled terms and a subsequent full elastic solution obtained in all the layers underneath; all the zone are modeled exactly with the dimensions and values as measured experimentally. In the second level, the silica along with the depleted layer and the graded zone down to 2 μm are treated as a beam. In the analysis for the deeper zone, the silica along with depleted layer and graded zone down to 8.27 micron are treated as a beam.

Figure 3.5, shows that for the given multilayer system there are three self-selective critical wrinkle states with the following components in the (k, ε) space: (0.072/μm, 0.219), (0.35/μm, 0.217) and (52/μm, 0.1). These correspond to wavelengths, L_1 = 0.12 μm, L_2 = 18 μm and L_3 = 85 μm. In the work presented here a pre-stretch ratio λ_{ps} = 1.5 was imposed before UV/Ozone treatment. However, in our analytical calculations, pre-stretch effect is not considered; therefore using the explicit expression for the wavenumber derived in Sun et al. (2012), we scale the

theoretical prediction by a factor of 0.56. Then, the scaled wavelengths become, L_{1s} = 0.067 µm, L_{2s} = 10 µm and L_{3s} = 45 µm. These values match very well with the FFT calculations (Appendix F, figure F.1, figure F.2) for the experimental measurements.

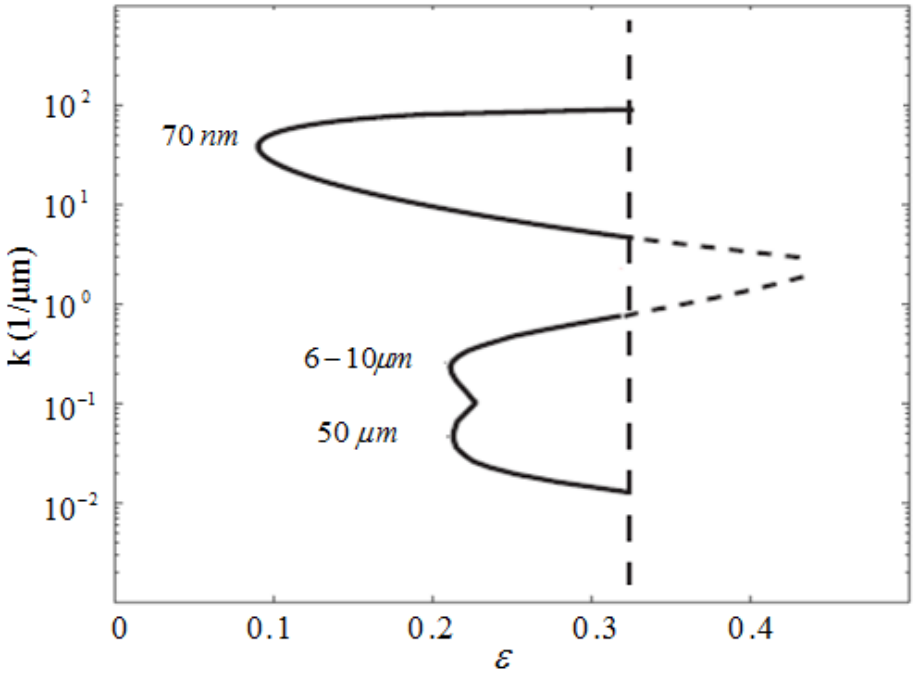

Figure 3.5 Critical wavenumber as a function of the critical strain for the composite structure resulted from the treatment of elastomeric material with UV/Ozone. The composite structure is modeled of three distinct materials: a silica layer (E = 148 MPa, ν = 0.3, t = 50 nm), an intermediate modulus depleted layer (E_0 = 10 MPa, η = 0.1) and a deep layer with graded modulus (E_1 = 50 MPa, η = 0.03). In the calculation, the beam theory was adopted for the silica layer and the neo-Hookean model for the other three layers and the solutions where match asymptotically in order to provide one curve (Analysis and plotting courtesy of M. Diab).

Conclusion

AFM measurmeents of the stiffness of a PDMS substrate treated with UV/ozone revealed a multi-layer system with several characteristic lengths scales. The linear bifurcation model predicted that the composite layer may buckle with different wavelengths that may span several orders of magnitude. The three-layer

model adopted in this masnuscript is very idealistic and the real systems may develop more layers upon treatement with UV/Ozone. It is expeted that every two adjacent layers with distinct mismatch of their moduli with an order of magnitude below 1 will provide another bifurcation solution with a specific detectable wavelength. A clear understanding of the formation of the different layers upon oxidation and the evolution of the wrinkles in the post-buckling regime may help designing multifunctional systems.

Chapter 4.0 Adhesion in Hydrogel Contacts

Abstract

A generalized thermoelastic model for adhesion was developed to elucidate the mechanism of dissipation within the viscoelastic bulk of a hydrogel. Results show that in addition to the expected energy release rate of interface formation as well as the viscoelastic drag and viscous flow dissipation, the bulk composition exhibit dissipation due to phase inhomogeneity motion. The mixing thermodynamics of the matrix and solvent composition determine the dynamics of the phase inhomogeneities, which can enhance or disrupt adhesion. The model also accounts for the time dependent behavior since, given enough time, these inhomogeneities can be influenced by image forces at the interface causing migration, which may in turn, affect the dissipation at the interface. A nondimensional parameter is proposed to discern the dominant dissipation mechanism in hyperelastic contact detachment.

4.1 Introduction

The contact between soft surfaces of elastic and viscoelastic nature has been central in the recent study of the biological system in the areas of protective coatings for lubrication and the durability of mechanical parts under extreme environmental conditions. Soft materials in particular exhibit adhesion dominated contact and frictional characteristic at multiple scales. Continuum models have sought to connect the molecular effects described by the cohesive zone laws and the macroscopic

measurement of adhesive energy spent separating contacting surfaces. Complex materials, such as hydrogels, are in particular use today due to improvements in the interrogation methods as well as fabrication techniques, but also due to their suitability in applications where mechanics meet the biological world. Applications that may benefit from a better understanding of the adhesion mechanism in soft materials include the protection of surfaces against the corrosive maritime environment, self-cleaning and biofouling, energy efficiency through low frictional coatings, as well as medical applications, which seek to avoid pathogen fouling and tribological failure of diarthrodial joints. This chapter reports on work to construct a model for the dissipation mechanisms involved in the adhesion observed in viscoelastic inhomogeneous hydrogel contacts.

4.2 Energy Criteria for Viscous-Elastic Contact Detachment

The detachment of elastic contacts is an inherently dissipative process where the Clausius-Duhem postulate for viscous-elastic contacts (inequality J.5 and equation J.7, Appendix J) provides the lower bound of entropy generation;

$$\rho\dot{\eta}\,\theta \geq \left(\Im^{inh}+\Im^{th}\right)\cdot\dot{\Re}_g + \frac{G_{Ic}\cdot\dot{\ell}}{A_T}, \qquad (4.1)$$

where $\nabla\cdot\underline{\wp} = \Im^{inh}$ is the configurational inhomegeneity force on the phase domain, $[\nabla s_c]\cdot\dot{\Re}_g = \dot{s}_c$ and $[\rho\, s_c]\nabla\theta = \Im^{th}$ represent the chain entropy changes and material thermal force per unit volume (F/L^3), respectively, $\dot{\Re}_g$ is the time rate of change of the radius of gyration of the polymer chain, A_T is the total area of contact, $\dot{l}$ is the rate of increase in crack length and G_{Ic} is the energy release rate in the normal mode.

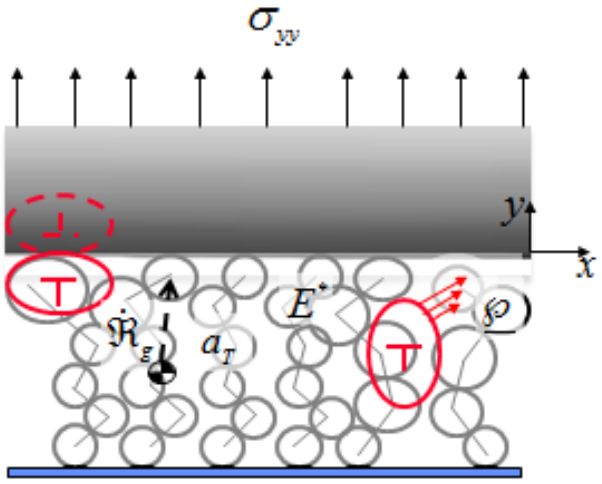

Figure 4.1 Schematic of mixing configuration of the polymer brush hydrogel under far-field (σ_{yy}) contact loading. The size of circles represents relative size of polymer-pervaded volume system. Note: inhomogeneity shown in red.

The rate of dissipation is $\dot{\Phi} = \rho\dot{\eta}\vartheta + \underline{\mathbf{P}}^{p} : \dot{\underline{\mathbf{F}}}$, and from the constitutive equation for the internal energy we know that; $\rho\dot{e} = \partial_{\underline{\mathbf{F}}} e : \dot{\underline{\mathbf{F}}}$, which along inequality 4.1 yields the dissipation (Truesdell 1984) for a viscous-elastic contact during detachment as given by;

$$\dot{\Phi} = \frac{G_{Ic} \cdot \dot{\ell}}{A_T} + \underline{\mathbf{P}}^{p} : \dot{\underline{\mathbf{F}}} + \left(\Im^{inh} + \Im^{th} \right) \cdot \dot{\Re}_g, \qquad (4.2)$$

where the mode I fracture energy release rate upon interfacial cracking during detachment given in terms of the interfacial energy between the two mating surfaces as; $G_{Ic} = 2\gamma^{(s)}$ (Broek 1982), and $\underline{\mathbf{P}}^{p}$ is the viscous stress due to fluid flow within the contact. This provides an energy-based interfacial fracture criterion discussed in the following section for viscoelastic contacts.

A criterion for detachment through crack propagation at the interface where the dissipation is equal to the effective energy release rate ($\dot{\Phi} = G_{eff} \cdot \dot{\ell}$) for fracture in a material of fading memory may be given by;

$$G_{Ic} \cdot \dot{\ell} \leq G_{eff} \cdot \dot{\ell} - \left\{ \underline{\mathbf{P}}^{P} : \underline{\dot{\mathbf{F}}} + \left(\Im^{inh} + \Im^{th} \right) \cdot \dot{\Re}_{g} \right\} A_{T} \ , \qquad (4.3)$$

where G_{eff} is the effective energy release rate.

4.3 Experiments and Measurements

4.3.1 Dimensional Analysis for Contact of Viscous-Elastic Solids

As shown in section 4.2, equation 4.2, the dissipation for a viscoelastic contact during detachment has functional relationships (Buckingham 1915), which for this set of variables are the following:

$$\begin{aligned} \Im^{inh} &= \hat{\Im}^{inh}\left(\gamma^{(inh)}, \xi^{(inh)} \right), \\ \Im^{th} &= \hat{\Im}^{th}\left(\rho_{g}, N, \nabla\theta \right), \\ G_{Ic} &= \hat{G}_{Ic}\left(\gamma^{(s)} \right), \\ \underline{\mathbf{P}}^{p} &= \underline{\hat{\mathbf{P}}}^{p}\left(\upsilon, \underline{\mathbf{D}}(t) \right), \end{aligned} \qquad (4.4)$$

where the dissipation due to the inhomogeneous phase motion is a function of the interfacial tension and shear force per unit length ($\gamma^{(inh)}, \xi^{(inh)}$) between the inhomogeneous phase and the bulk material. The material thermal forces are assumed to be small since the small thermal gradients ($\nabla\theta$) may be equilibrated quickly through the convective motion of the free-flowing solvent, while the grafting density (ρ_{g}) and degree of polymerization (N) are constants. The energy release

rate in the normal mode is a function of the energy per unit area of surface ($\gamma^{(s)}$). The viscous stress is a function of the viscosity (υ) of the fluid and the shear strain rate tensor ($\underline{\mathbf{D}}$).

4.3.2 Sample Preparation

4.3.2.1 Glycoprotein Coating Preparation

PRG4 glycoprotein was purified from human synovial fluid as described previously by Jay (Jay 1992). Purified human lubricin was diluted to concentrations of 10, 100, 200, 250 μg/ml in 0.9% NaCl (physiologic saline). Solutions were deposited on highly ordered pyrolytic graphite (HOPG) substrate to allow for thermodynamic equilibrium to be reached as the lubricin molecules settled on the hydrophobic surface. After 10 minutes the excess solution was removed with a pipette and the remaining fluid was extracted through capillary action, without disturbing the surface.

4.3.2.2 Direct Grafting of Polymer Chains

Poly(acrylic acid) (PAA, ≥99.5%), poly(styrene)-block-poly(acrylic acid) (PS-b-PAA), 3-(amino propyl) triethoxysilane (3-APTS), and N,N-dimethylformamide (DMF) were purchased from Sigma Aldrich, the poly(ethylene glycol) (PEG) was purchased from Fluka, ammonium hydroxide, sodium chloride sulfuric acid, silicone oil, hydrogen peroxide, ethanol, and methanol were either already on hand or purchased from Sigma Aldrich, Fisher Scientific, Across Organics and Gelest. Sea water powder was purchased from Lake Products

Company, Inc. Glass substrates were initially cleaned with piranha solution to remove organic residues. Piranha solution contains 3:1 mixture of sulfuric acid and 30% hydrogen peroxide. First, hydrogen peroxide was added to sulfuric acid in the fixed volume and then added to the glass container with the glass substrates for 2 hours at 100^{o}C. The glass substrates were then removed after it was cooled and rinsed several times with deionized (DI) water, and stored in DI water until use. Prior to coating with silane, the glass substrates were hydroxylated to enhance the density of available sites for silane reaction and improve surface modification. The glass substrates were soaked in 70:30 mixture of DI water with 30% hydrogen peroxide for 45 min at 70^{o}C, and then 5ml of NH_4OH was added for each 100ml of water/hydrogen peroxide solution. After cooling, slides were rinsed in DI water thoroughly and dried under a stream of nitrogen (N_2). Hydroxy-terminated glass slides were placed in 50 ml flasks containing 30 ml of mixture of anhydrous toluene and 0.2M 3-(amino propyl) triethoxysilane. The flask were stirred under a nitrogen atmosphere and heated to 80^{o}C for 12 hours. The resulting glass slides were washed with methanol solution and dried under vacuum at 35^{o}C to afford silane-modified glass slides. These silane-modified glass slides, polymer (PAA or PEG) and 10ml of N, N-dimethylformamide (DMF) were placed in a reaction vessel and stirred while being heated in an oil bath at 140^{o}C for 24 h. The slides were washed with DMF and methanol, and then dried under vacuum to remove the excess solvent. The characterization of the chemical composition of the hydrogel coatings is found in Appendix K.

The surface energy measurements to characterized the hydrogels were done following the method described in Section 2.3.1.

4.3.3 Contact Measurements

Adhesion measurements were made using the atomic force microscopy (AFM) Dimension 3100 with Nanoscope IIIa controller (Veeco Metrology, Inc., Santa Barbara, CA) in the *pulse force mode* (PFM) (Krotil 1999). For an overview of the pulse force mode see Appendix D. The PFM allows for the study of soft matter without disrupting its structural integrity by accessing feedback signals with a digital data acquisition (WITec GmbH, Ulm Germany). A high resolution PFM scan of the surface was conducted in order to assess the morphology of the hydrogel surface.

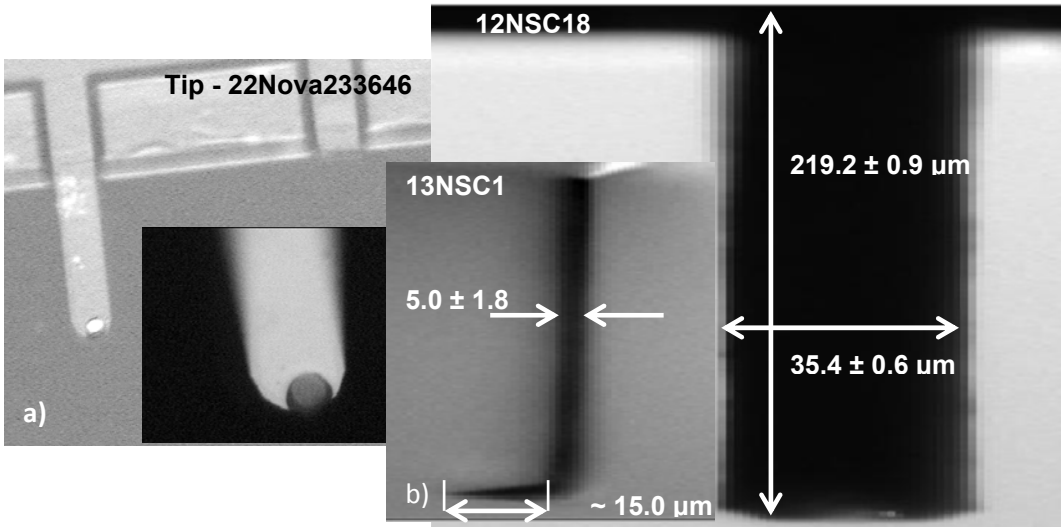

Figure 4.2 Colloidal probe (a) on AFM cantilever, and CCD images (b) for plane and lateral views of sharp AFM cantilevers used for topographical resolution.

Two types of AFM cantilever were used. The silicon nitride sharp cantilevers were used to obtain high resolution images of the coatings (figure 4.2b). In order to apply a contact mechanics theoretical framework to the analysis, a series of colloidal

probe cantilevers were fabricated in our laboratory. Borosilicate colloidal probe AFM tips (Novascan Technologies, Inc., Ames, IA) with a 12μm radius (figure 4.2a) were employed for contact measurements. The measurement was repeated for every pixel of the AFM surface image, yielding the 2-dimensional data maps for each sample. A MATLAB technical computer language algorithm was written in order to analyze each PFM curve. The main features gathered from the PFM curve include long-range forces during approach, van der Waal attractive forces during first contact, coating stiffness, maximum force exerted on the cantilever, maximum adhesive force and the work of adhesion during de-bonding.

4.3.3.1 Calibration Method

The *diamagnetic normal force calibration system* or D-NFC system described in Chapter 2.0 was used to calibrate the stiffness of the cantilever. The cantilever used in the following measurements was calibrated to have a stiffness of 7.1394 N/m.

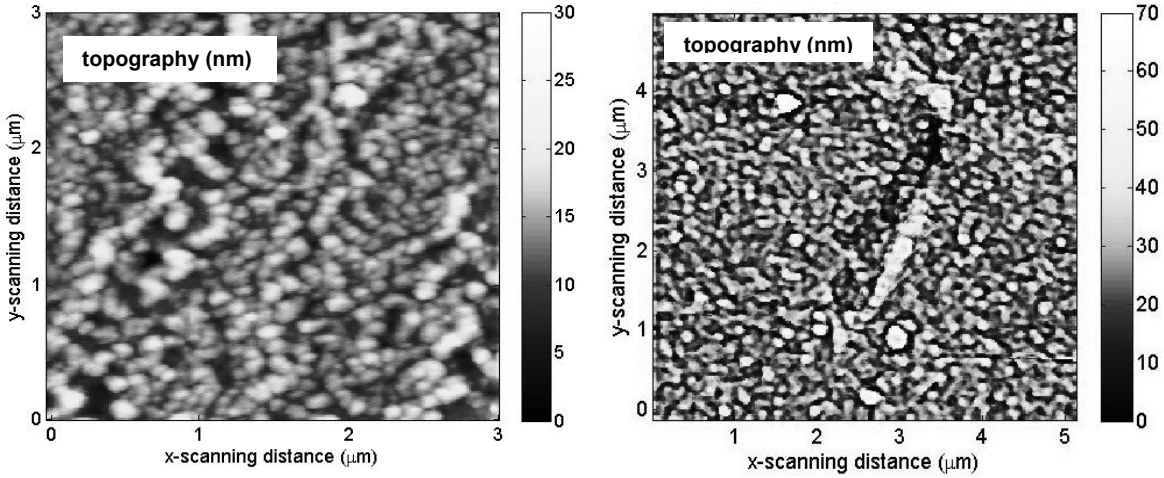

Figure 4.3 Topography data from 2-dimensional PFM images of lubricin (left) and rafted PAA polymer brushes (right).

4.4 Results and Discussion

In order to assess the adhesive properties of the hydrogel systems, the work of adhesion (area between the force curve and the displacement axis) must be quantified. The following sections uses the parameter space described in equation 4.4 to normalize for important variable.

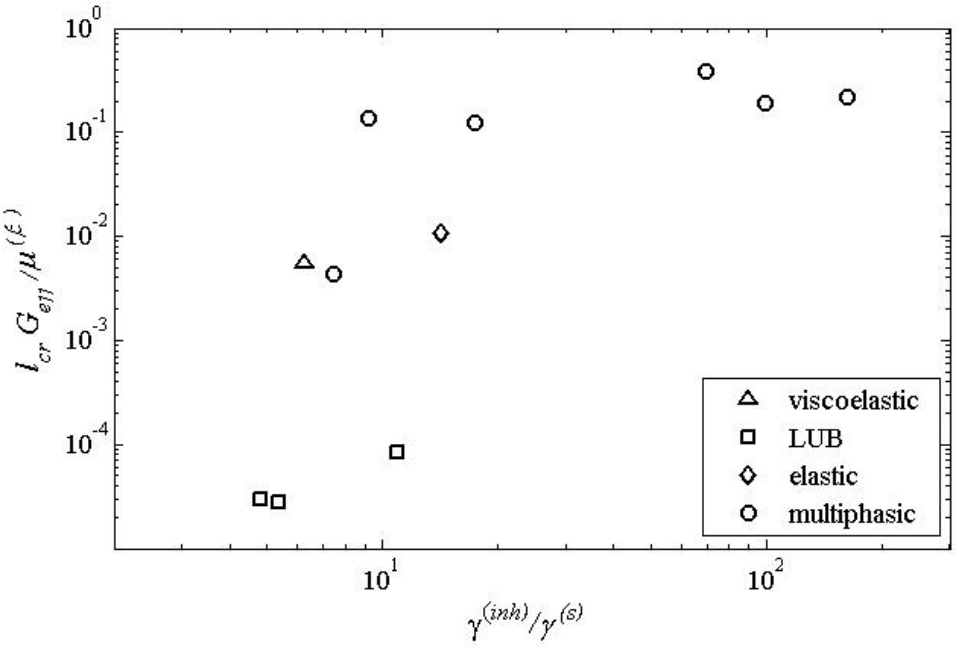

Figure 4.4 Normalized energy release rate as a function of the normalized phase interfacial tension. As the phase interfacial tension increase so does the dissipation of elastic energy increase with scaling (α) of 9/5.

4.4.1 Hydrogel Adhesive Response

Lubricin formed a physisorbed, 2-dimensional rough coating over hydrophobic highly oriented pyrolitic graphite (HOPG). Figure 4.3 shows the topography image for both lubricin (the 250μg/ml, left) and the fabricated polyacrylic acid (PAA) polymer brush coatings grafted on a glass slide (right). The

colloidal probe data from which the adhesive response is quantified is discussed in this section.

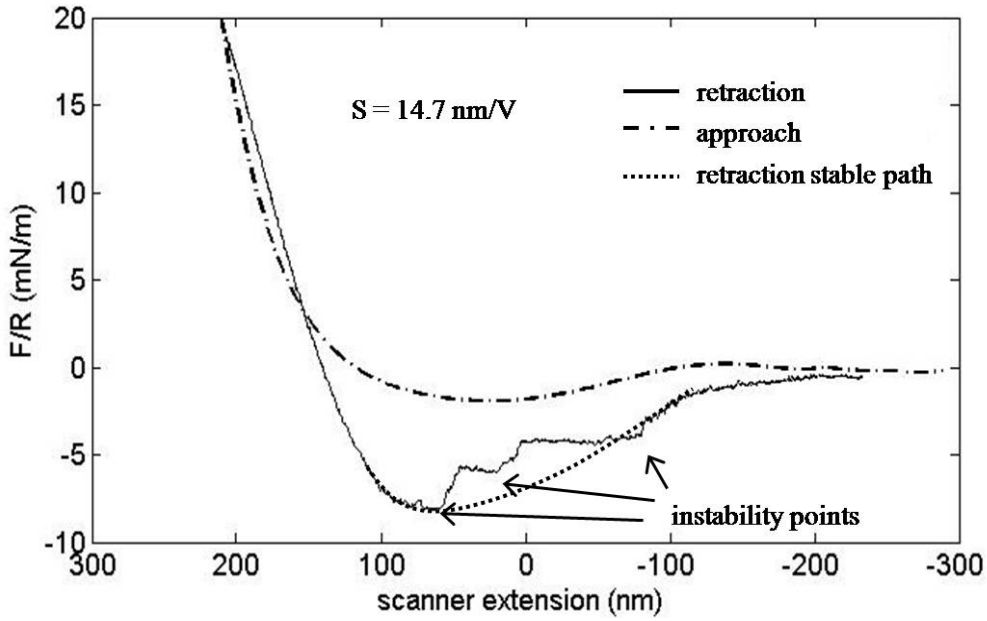

Figure 4.5 Normalized adhesive force as a function of contact distance in hyperelastic hydrogel AFM measurement with adhesive forces sudden drop at instability points (Li 2009, Chung 2006).

Figure 4.4 shows the effective work of separation, normalized by the mixing chemical potential ($\mu^{(\beta)}$) and the critical flaw half-length (l_{cr}), as a function of the inhomogeneity surface tension ($\gamma^{(inh)}$) and the work of adhesion ($\gamma^{(s)}$) related to the pull-off force for a purely elastic contact by the JKR model (Johnson 1971). The critical flaw half-length is estimated by; $l_{cr} \approx 8E^*\gamma^{(s)} \Big/ \pi\nu^*\sigma^{(cr)2}$, where E^* and ν^* are the contact modulus and Poisson's ratio, respectively, and $\sigma^{(cr)}$ is the critical far-field stress at which the contact begins detachment (Griffith 1921). Note, that there is an order of magnitude increase in mixing-normalized work of separation; $l_{cr}G_{eff} \Big/ \mu^{(\beta)} \sim 10^{-4} \rightarrow 10^{-1}$ with a corresponding order of magnitude increase in

normalized inhomogeneity surface tension. As the ratio of the surface energy and surface tension of the inhomogeneity approaches unity, the phase inhomogeneity loses its dominant effect in dissipation exhibiting a plateau effect.

The typical retraction data of the AFM cantilever for the hydrogels (figure 4.5) exhibits instability points where the adhesive force drops drastically in a stepwise fashion (Chung 2006, Li 2009). This phenomenon within the contact modifies the effective work of adhesion by producing low adhesion areas where these instabilities allow for the interfacial crack to propagate with lower energy dissipation.

4.4.2 Viscoelastic Adhesion

The viscoelastic dissipation in equation 4.2 (second term on the right) is a function of the time-dependent contact modulus and reduced crack speed, $\dot{\Phi}^P = \dot{\hat{\Phi}}^P\left(E^*, a_T \dot{\ell}\right)$. Therefore, the viscoelastic response of a material contact detachment is determined by the energy stored and dissipated within the bulk as well as interface formation. A shift factor may be calculated from the ratio of relaxation time τ_p (Ferry 1961) at the temperature in question (θ) and some reference temperature if the relaxation time is the variable used to characterize the time-dependent behavior of viscoelastic materials and if the structural behavior of the polymer solution is assumed to have the same dependence over a wide range of thermodynamic variables (temperature, pressures, concentrations, etc.). Therefore, with both bulk viscous behavior and mixing thermodynamics dominating the dissipation by the bulk, a ratio of viscous dissipation and the phase inhomogeneity

dissipation maybe calculated using the forcing frequency (ω), the phase inhomogeneity surface tension ($\gamma^{(inh)}$), the modulus ($E^*(\omega)$), and the reduced crack speed ($a_T \dot{\ell}$) with the viscoelastic shift factor (a_T) (Ferry 1961) given by;

$$a_T = \frac{\zeta \theta_g}{\zeta_g \theta}, \tag{4.7}$$

where θ is the temperature in question, θ_g is the glass transition temperature (subscript g), ζ is the frictional coefficient per unit monomer. The viscoelastic factor derived from the William-Landel-Ferry (WLF) theory for dispersive response of a viscoelastic material (Williams 1955, Ferry 1961**)** is given in terms of experimental factors as

$$\log a_T = -\frac{B}{2.303\phi_g} \frac{\theta - \theta_g}{\phi_g / \alpha_f + \theta - \theta_g}, \tag{4.8}$$

where B is an polymer-specific empirically approximated numerical factor, ϕ_g is the frictional coefficient per unit molecule, α_f is the thermal expansion of volume fraction. The scaling parameter derived by applying dimensional similarity is given by

$$\frac{R}{10^3 a_c} \cdot \frac{E^* a_T \dot{l}}{\omega \gamma^{(inh)}}, \tag{4.9}$$

where a factor of 10^{-3} has been added to convert the nondimensional group to the order of unity. This parameter is hereby referred to as the *Gent-Eshelby* (*Ge*) *number*, where R is the contact radius and a_c is the contact radius calculated from the JKR model (Johnson 1971).

Figure 4.6 shows that most of the coatings tested were of the hydrogel type ($Ge << 1$), pointing to the phase inhomogeneity as the dominating mechanism of dissipation. Whereas in the hydrophobic polystyrene coatings in water (triangle), a combination of low miscibility, the value of $Ge \approx 1$ points to the viscous dissipation as the dominant mechanism. The relaxation time for processes occurring above the glass transition temperature (θ_g) is proportional to the monomeric friction coefficient (ζ), that is $\tau^l \approx (N^v b)^3 \zeta / k_b \theta$, where N is the degree of polymerization, b is the Kuhn length and k_b is Boltzmann's constant (Doi 1986). For reduced crack speeds on the order equal or less than 30μm/s ($Ge \leq 1$) inhomogeneity and viscous processes will dominate dissipation. Therefore, using the reduce crack speed gives a consideration to the time scales involved in the competing dissipation processes. For $Ge >> 1$ elastic brittle failure of the interface is the dominant mode of detachment. Note also, that the elastic contact for the unetched glass (diamond with $Ge >> 1$) falls also under this category, while the hydroxylated (etched) glass (diamond with $Ge \sim 1$) exhibits some viscous drag due to the water bound to the surface hydroxide groups.

This phenomena is consistent with the usual practice of subjecting glass to a variety of chemical processes that produce the surface hydroxylation in order to improve adhesion, *e.g.*, Sulfuric acid/hydrogen-peroxide (piranha) cleaning solution, ultraviolet/ozone irradiation, plasma etching, *etc.* Although the layering of water at the surface produces structural (non-DLVO) repulsive forces measured on approach (Israelachvili 1991), this does not necessarily signify lower adhesion, as the oscillatory behavior also implies an irreversible process with the energetic valleys

that must be overcome during retraction in order to produce movement on the interfacial crack front.

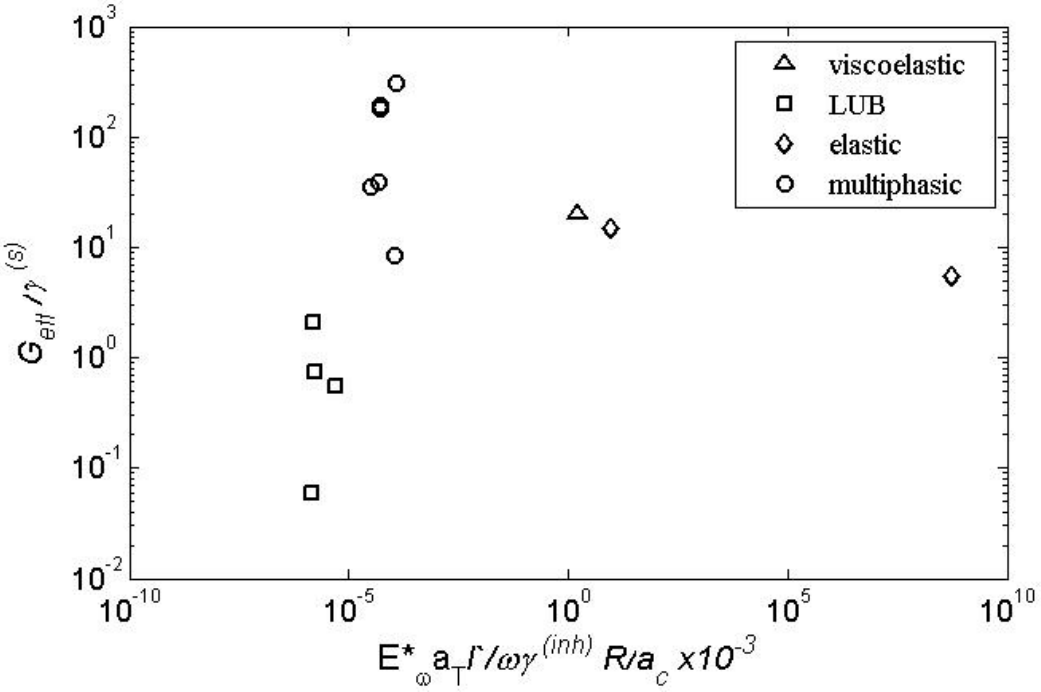

Figure 4.6 Normalized energy release dissipation as a function of the ratio of viscoelastic dissipation and dissipation due to phase inhomogeneity motion.

The water layer increases adhesion by dissipating elastic energy, not only by increasing the intrinsic surface energy, but also through the exertion of a drag on the crack front, represented by the first and second terms on the right of equation 4.2, respectively. An account of the measured properties used in the calculations of the graphs in this section may be found in Appendix L.

4.5 Conclusion

The effective energy release rate for a hydrogel contact has the functional form;

$$G_{eff} = \gamma^{(s)} + \gamma^{(s)}\dot{\hat{\Phi}}_i(a_T\dot{l}) + \dot{\hat{\Phi}}_j(\gamma^{(inh)}), \qquad (4.10)$$

where the first and second terms on the right are both a function of the surface energy, the second term being also a fractional term of the plastic dissipation due to viscous drag on the crack front, and the third term on the right is the additional dissipation term due to phase inhomogeneity motion. Normalizing for the dominant viscoelastic and phase inhomogeneity motion effects, yields the scaling of $\alpha \cong 1/3$ (figure 4.7) for the phase inhomogeneity-dominated adhesion.

The rate dependence of adhesion strength was first reported by Gent and Petrich in 1969 as the viscoelastic transitions between a viscous interface failing at lower rates of peel, into a viscoelastic and subsequently purely elastic interface as the rates of peeling increase. All of these effects were also shown to be failure mode dependent. In their work, the WLF theory was used to reconcile the differences in crack front speed at a wide range of peel rates, thereby elucidating the viscoelastic "drag" on the crack front. Previous work by Gent et al. (1968) and Kaelble (1964) had shown the congruence between this temperature and rate response for the bond strength, with the dispersive viscoelastic response of the polymeric adhesive.

Generally an increase in adhesive dissipation was observed with peel rate or temperature increase to a specific maximum value followed by a decrease in adhesion due to a transition into the purely elastic material behavior while maintaining the same failure mode throughout the temperature and peel rate range (Gent 1969).

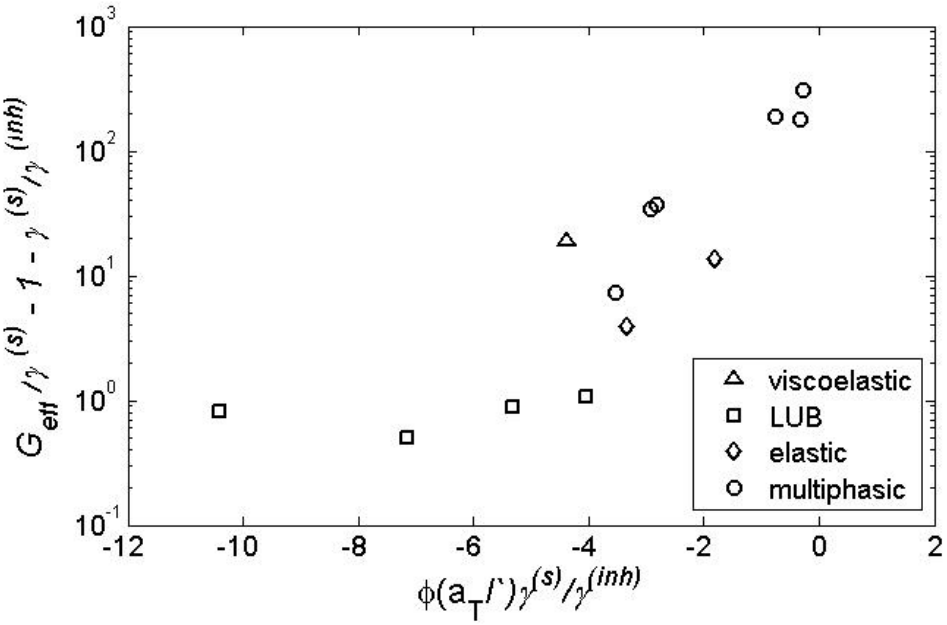

Figure 4.7 Effective energy release rate as a function of the reduced crack speed normalized for the dissipation mechanisms.

These transitions in viscoelastic behavior were not thought then to be due to transitions from viscous to viscoelastic to purely elastic bulk behavior, but transitions in viscoelastic behavior arising from the polymer chain dynamics. The first transition is associated with the frictional slip among polymeric chains and solvent flow, while the transition at high rates is due to individual polymer chains uncoiling. In the viscous regime an increase in adhesion is commensurate with the increase in viscous dissipation as the viscous drag effects dominate the complex modulus. The abrupt decay in contact stiffness within a narrow range of rates at the onset of elastic behavior originates from energy dissipated exclusively in the reconstitution of the interface with little changes in the viscous modulus. Nevertheless, the increase in adhesive dissipation with increasing rates resumes as

the viscous modulus increases and the cohesion returns to dominate the failure mode. Another less abrupt decay in contact stiffness within a range of rates occurs at the onset of elastic chain coiling induced elasticity and rotational drag, along with viscous flow dissipation. Within this (Gent *et al*.) viscoelastic framework, the role of interfacial contact instability remains unclear. Instabilities will add an additional time dependent component to the adhesion and cohesive failure modes in hydrogels. As the deformation rate increases to produce a Gent-Eshelby number greater than unity ($Ge > 1$) the crack speed through the interface ($E^* a_T \dot{l}$) increases and less time is afforded for phase inhomogeneities to reach the interface, as well as less time for inhomogeneities already at the interface to grow to the unstable contact critical size, thereby exhibiting an increasing adhesive dissipation**.** As $Ge << 1$ decreases, there is enough time for inhomogeneities ($\omega\gamma^{(inh)}$) to accumulate at the crack front and increase the instability driven rupture. Although this process of transport increases the total dissipation by adding a new mechanism, namely the dissipation due to phase inhomogeneity motion (third term on the right of equation 4.1), that increase may be countered by the reduction of the viscous dissipation at the crack front due to defect-enhanced stress, reducing the overall energy needed to form a new interface through crack opening.

Chapter 5.0 Concluding Remarks

Abstract

Viscoelastic hydrogel adhesion has been typically characterized by the affinity between surfaces to reduce the surface stresses given by unrestricted molecular species on a free surface, as well as mechanisms involved in the disruption of the interface, such as crack propagation, which accounts for the rate dependence of the adhesive energy measured in soft contacts. In this work, additional interactions related to the transport of species within the bulk of the material below the surface was demonstrated. In order to characterize contacts involving hydrogels, it is important to give consideration to the quality of the mixture between the polymeric substances comprising the coatings and the solvent environment in which these are submerge. A parametric study of the material properties has been presented in order to optimize desired surface interactions.

5.1 Measurements and Instrumentation

In order to elucidate the concurrent mechanisms responsible for the adhesion of the soft condensed materials, a normal calibration device (D-NFC), which provides single millinewton per meter of displacement calibration, has been developed.This deviceenabled the measurements of adhesive energy dissipated during contact detachment, as well as sub-megapascal changes with depth in modulus of UV-treated PDMS surfaces. The morphology of these distinctive layers,

and the ratio of the changing moduli in the bulk near the surface of the PDMS, has been correlated to the nested wrinkle morphology observed using Diab et. al. work (Diab 2014). The multilayered structure arising from UV radiation of the PDMS has been shown to be a mechanism for surface modification distinct from the period doubling mechanism shown by Sun and coworkers (Sun 2011).

5.2 The Use of Low Adhesion Coatings in Antifouling Applications

Past work in the area of development for antifouling coatings have sought to develop passive coatings, which reduced adhesion or even in some cases produce a repulsive force between the coating and the fouling biological agents, avoiding adhesion altogether. Such techniques have not yielded coatings which can eliminate fouling but have met various levels of success in delaying the settlement of fouling on the surface. The community of technologists and scientists have sought an elusive metric to compare and characterize coatings while at the same time providing an understanding of the mechanisms influencing adhesion. Surface energy and wetting have been at the forefront of the characterization metrics due to the popularity, grounded in the effectiveness and elegance of the JKR and DMT models for elastic contacts. Nevertheless, under these models, inconsistent results have yielded a slow progress in optimization of marginally effective coatings. The main reason for this is that the constitutive assumptions in theories are not appropriate to model the complex interaction of hydrogel coatings and soft biological surfaces of cells, which can change their surfaces in response to external stimuli including the surface energy of the synthetic counter-surface where settlement is meant to occur.

Detachment between two surfaces requires a conversion between elastic energy and the energy necessary to produce the interfacial surface area.This work has shown detachment dissipation in a viscoelastic hydrogel surface to be a function of interfacial crack speed and the viscous drag, the surface energy, and bulk mixinginteractions, which may affect the interface and enhanced detachment. With this knowledge the biofouling attachment of microscopic spores was analyzed. Figure 5.1 showsthe biofouling spore settling as a function of the energy release rate (G_{eff}) or energy dissipated by the contact during detachment,normalized with the JKR calculated work of adhesion ($\gamma^{(s)}$)for various multiphasic hydrogels (circles) and viscoelastic (triangle) and purely elastic (diamonds) coatings. The effects of the surface dominated adhesion seen in purely elastic and viscoelastic surfaces are contrasted to the bulk dominated effects exhibited by hydrogel coatings.

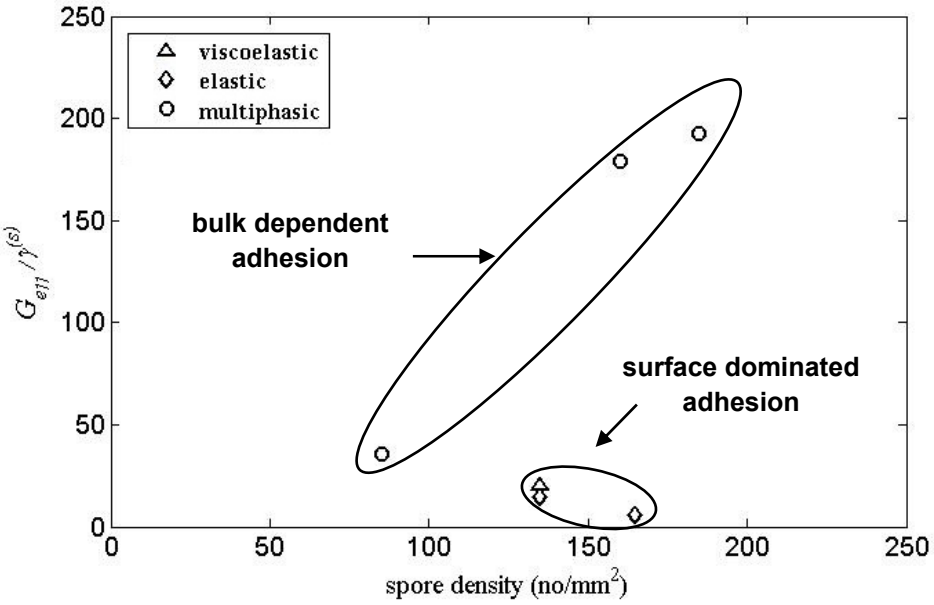

Figure 5.1 Ulva spore settlement as a function of surface energy-normalized energy release rate.

Of all of the coatings studied, the lubricin glycoprotein (LUB) coating, also known as PRG4, showed the lowest adhesion due to its complex failure mechanism, which includes cohesive as well as interfacial inhomogeneity weakening (figure 4.5) (Jay 1992). Expressing the inhomogeneity surface tension as a change of free energy of mixing due to the increase of interfacial area ($\gamma^{(inh)} = \partial \psi_{H\,mix} / \partial S$) (Dill 2003**)** allows for the design of polymer-solvent mixtures that will behave as a desired hydrogel. Coatings with the lowest possible adhesion must attain a multimodal failure mechanism. Ideally, a coating which exhibits a hydrogel polymer amphipathic surface structure, at the same time allowing for low intrinsic surface energy and cohesive failure must be fabricated. As the coating fails cohesively, a consistent hydrogel structure must remain in the new surface. This is not a simple task; however advances in new materials like nanocomposite polymers may be an avenue to explore.

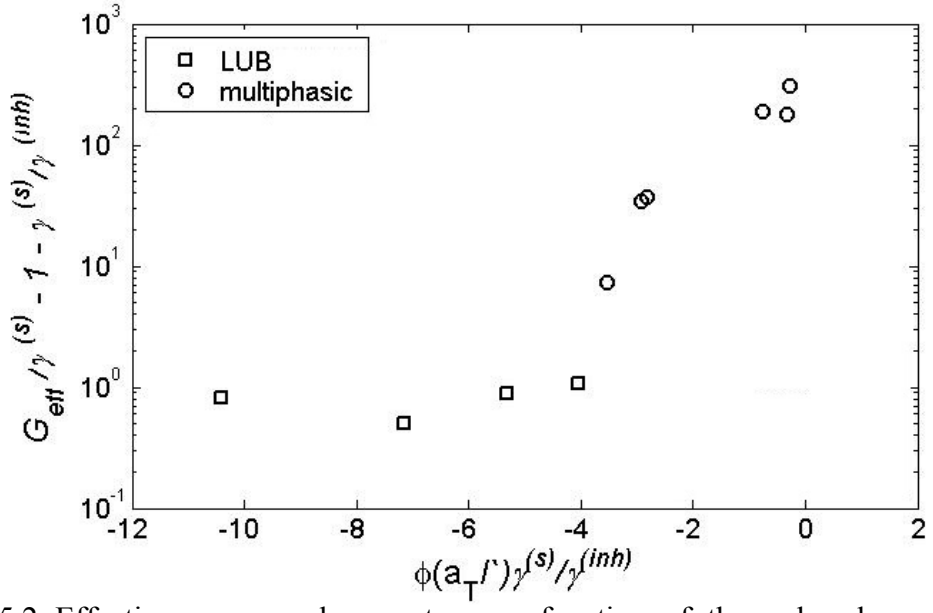

Figure 5.2 Effective energy release rate as a function of the reduced crack speed normalized by the phase inhomogeneity surface tension.

In the biotribological field, the new understanding of the bulk effects in hydrogel adhesion developed in this work has important implications for the micromechanics of adhesion and thin film rheology of the lubricin-hyaluronate complex (Jay 1992, Jay 2007b). In such hydrogels, the glycoprotein lubricin forms an inhomogenous moety, which provides the reduced adhesion in diarthrodial mammalian joints. In the absence of lubricin viscosity-supplementing hydrogels of hyaluronate will be less effective in improving boundary lubrication and only when grafted into the surface has hyaluronate shown a reduction in the coefficient of friction. In the absence of lubricin, hyaluronate lacks the defect mechanism necessary for cohesive failure, which yields a lower adhesion.

5.3 Future Work

At the molecular level, it is not yet clear what parameters are necessary to enhance defect assisted adhesive and cohesive failures. Materials like lubricin fail cohesively thereby reducing adhesion at a wide range of deformation rates, while other hydrogels with very low adhesion fail at the interface at some critical flaw size. Experimentally, the diffusion of species and the mixing characteristics of hydrogels may be assessed optically using particle-tracking velocimetry (PTV) studies (Jay 2007b) within a surface force apparatus (SFA) system (Israelchvili 1991). Along with the diffusive characteristics of the polymer-solvent mixture, a perturbation analysis for the characteristic wavelength of the defect distribution in the contact would shed light on the characteristic time scales for inhomogenity transport and its effects on both adhesive and cohesive failures. For this purpose the biaxial strain

modeling of PDMS nano-scale wrinkles would allow the fabrication of engineered surfaces providing a controlled defect-dominated interface. The study of the effects of defect distribution in such surfaces would serve as a validation of the characteristic wavelength perturbation study.

A careful study of lubricin and hyaluronic acid complex may clearly help confirm that the low adhesive behavior is dominated by cohesive failure of the thin film facilitated by the presence of lubricin.

On the instrumentation aspect of this work, the oscillatory behavior exhibited by the new D-NFC calibration system in the presence of water allows for the interrogation of the influence of molecular arrangement on intermolecular and surface force fields. If further characterized for this purpose, this simple device may be used to study the water structural arrangement on polymeric surfaces, which may be further correlated to coating adhesive behavior in a number of environments.

Appendix to Adhesion in Hydrogel Contacts

Appendix A: Dynamic Characteristics of the Diamagnetic-Normal Force Calibration System

The Lagrangian function (Forray 1968) for the D-NFC system is given by

$$L = \frac{1}{2}\sum_{i,j=1}^{3}\left[I_{ij}\dot{\Omega}_i\dot{\Omega}_j - \kappa_m\Omega_i\Omega_j\right], \qquad \text{(A.1)}$$

where the terms on the right represent the kinetic energy due to the moment of inertia and the stored magnetic energy, respectively. The force balance accounting for the damping of air for the tilting oscillator is found applying Lagrange's equation $\partial L/\partial\Omega_j = d/dt\left(\partial L/\partial\dot{\Omega}_j\right) - \partial L/\partial\Omega_j$, (Forray 1968) and is given by

$$\sum_{i,j=1}^{3}\left[I_{ij}\ddot{\Omega}_j + \kappa_{ij}^{m}\Omega_j\right] = \sum_{i,j=1}^{3} d_{ij}\dot{\Omega}_j, \qquad \text{(A.2)}$$

where I_{ij} is the moment of inertia tensor (Taylor 2005), and d_{ij} is the damping coefficient due to rotational motion drag.

Appendix B: D-NFC Error Propagation Analysis

The measurement sensitivity for each step in the calibration process was derived using equation 2.12. In the case of the device characterization the sensitivity for each step is given as follows; the mass measurement sensitivity is

$$\theta_m = \frac{\left(2R^2 + 5l^2\right)\omega^2\omega_o^2}{5\left(\omega^2 - \omega_0^2\right)}, \qquad \text{(B.1)}$$

the glass bead radius measurement sensitivity given as

$$\theta_R = \frac{4mR\omega^2\omega_o^2}{5\left(\omega^2 - \omega_0^2\right)}, \qquad \text{(B.2)}$$

the sensitivity of the glass bead placement position during the measurement given as

$$\theta_l = \frac{2lm\omega^2\omega_o^2}{\left(\omega^2 - \omega_0^2\right)}, \qquad \text{(B.3)}$$

the natural frequency measurement sensitivity for the cantilever and the cantilever with a glass bead placed on it are given respectively by

$$\theta_w = -\frac{2m\omega\omega_o^4\left(2R^2 + 5l^2\right)}{5\left(\omega^2 - \omega_0^2\right)^2} \quad \text{and} \quad \theta_{wo} = -\frac{2m\omega^4\omega_o\left(2R^2 + 5l^2\right)}{5\left(\omega^2 - \omega_0^2\right)^2}. \qquad \text{(B.4)}$$

It must be noted that this measurement is specially sensitive to the angular frequency shift, therefore a sufficiently heavy bead must be used in order to achieve a frequency shift on an order greater than 100 $\left(\omega^2 - \omega_0^2 \geq 100\right)$. For the calibration of each AFM cantilever the sensitivity for the angular stiffness and the arm produced by the position of the contact between AFM cantilever and D-NFC is $\theta_l = 1/l^2$ and $\theta_l = -2\alpha/l^3$, respectively. For the actual calibration of AFM tips the uncertainty sensitivity is given by $\theta_{kref} \approx S_g / S_{D\text{–}NFC}$.

Appendix C: Wrinkle Structure Evolution as a Function of Exposure Time to UV/Ozone

The average wavelength, across the entire image, was recorded once the wrinkles were observed to have formed. Wavelengths of different PDMS samples with exposure time varying between 60 and 240 minutes are shown in figure A.1a.

The wavelength and amplitude (figure A.1b) of the wrinkle mode varies almost linearly with the exposure time up to 210 minutes beyond which the wavelength becomes constant. This indicates that the chemical process governing the transformation between PDMS and SiO_x reaches saturation where the reactants near the surface of the PDMS are depleted due to the reaction rate surpassing the diffusion rate. In addition to this, the growth of the SiO_x layer on the free surface will reach a thickness, which will block any further diffusion of oxygen towards the bulk materials, in which case any modification of the polymer at depth would be limited by dissolved oxygen within the bulk.

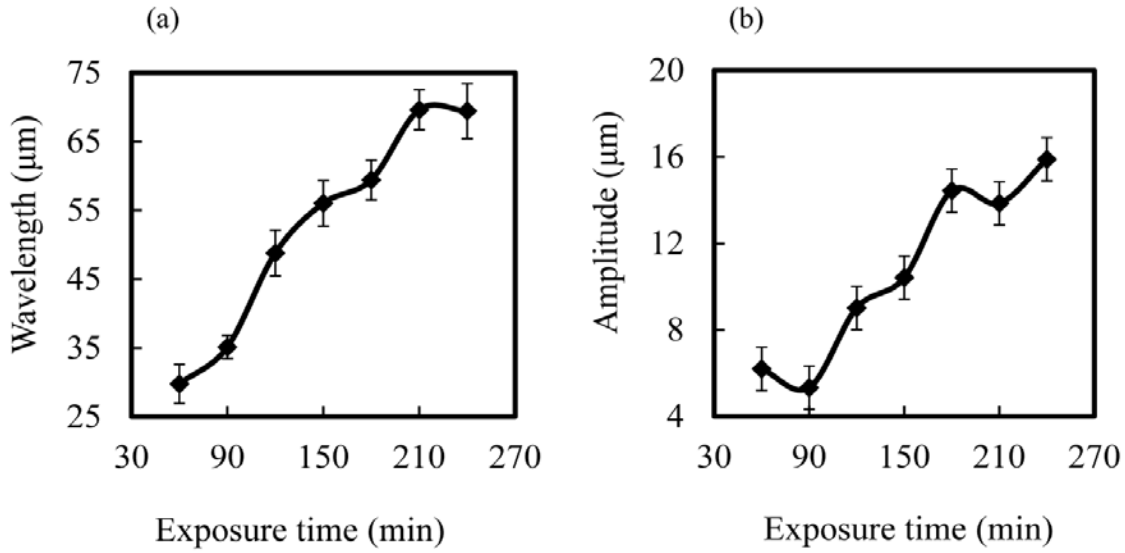

Figure A.1 Effect of the exposure time to the UV/zone on the wavelength (a) and amplitude of the wrinkle (b) of the wrinkled PDMS; wavelength is measured after fully releasing the sample; an error bar indicates 1 standard deviation.

Appendix D: Pulse Force Modulation

In the pulse force modulation of the AFM scanner is attained by applying an electric field of sinusoidal time variation. In this manner the relative displacement between the cantilever and can be made to produce an intermittent contact where the

force response as a function of distance acquired. Figure A.2 show the modulation of the scanner (cut line) superimposed on the data collected at the position sensitive photo-diode (PSPD) for the cantilever response (solid line).

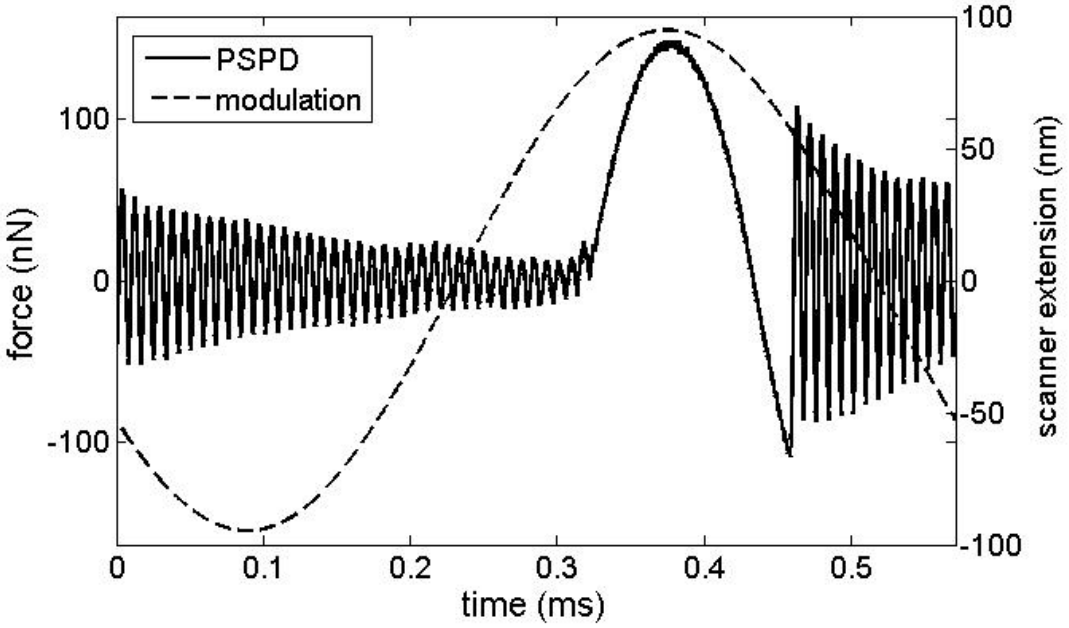

Figure A.2 Scanner extension (cut line) and cantilever response data collected at the PSPD (solid line) as a function of time. As the AFM scanner stretches and contracts in a sinusoidal electric field, the cantilever makes contact (time = 0.31ms) with, and detaches (time = 0.46ms) from the surface. Note the oscillatory behavior of the cantilever on approach and retraction.

Multiple force modulation curves may be collected for each image pixel by coordinating the lateral displacement of the scanner with the frequency of the normal sinusoidal variation. In this work the complete force modulation curves produced between the cantilever and hydrogel substrate were stored for later analysis. Figure A.3 shows what data may be extracted from each curve. Note the two curves shown for different pixel coordinates in the adhesion image.

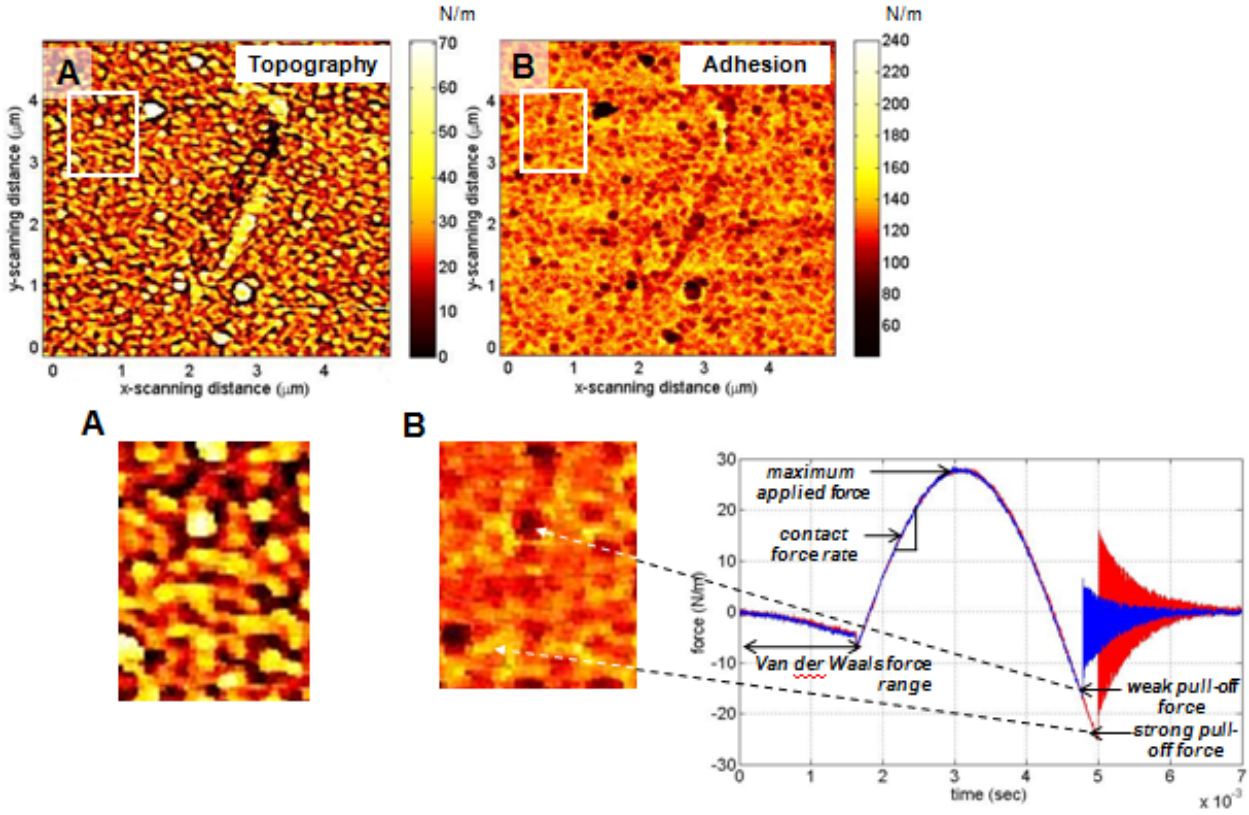

Figure A.3 Topography and adhesion data mapping, shown as A and B, respectively, extracted from pulse force modulation curves (bottom right). The bottom right shows a graph of two representative curves from which topography and adhesion information of the two pixels in the above image is taken. Text in the graph shows portions of the time series that provide data for different interaction forces between the cantilever probe and the substrate.

Appendix E: Cross-sectional Modulus Calculations from AFM Contact Stiffness Measurements

The contact stiffness was calculated using AFM data from the force as a function of depth data (figure A.4, bottom left), as well as the corresponding surface penetration calculated from the difference between the scanner extension and cantilever displacement. The edge effect was found by a finite element analysis to be

negligible at the low forces (on the order of nanonewtons) used to measure the contact stiffness.

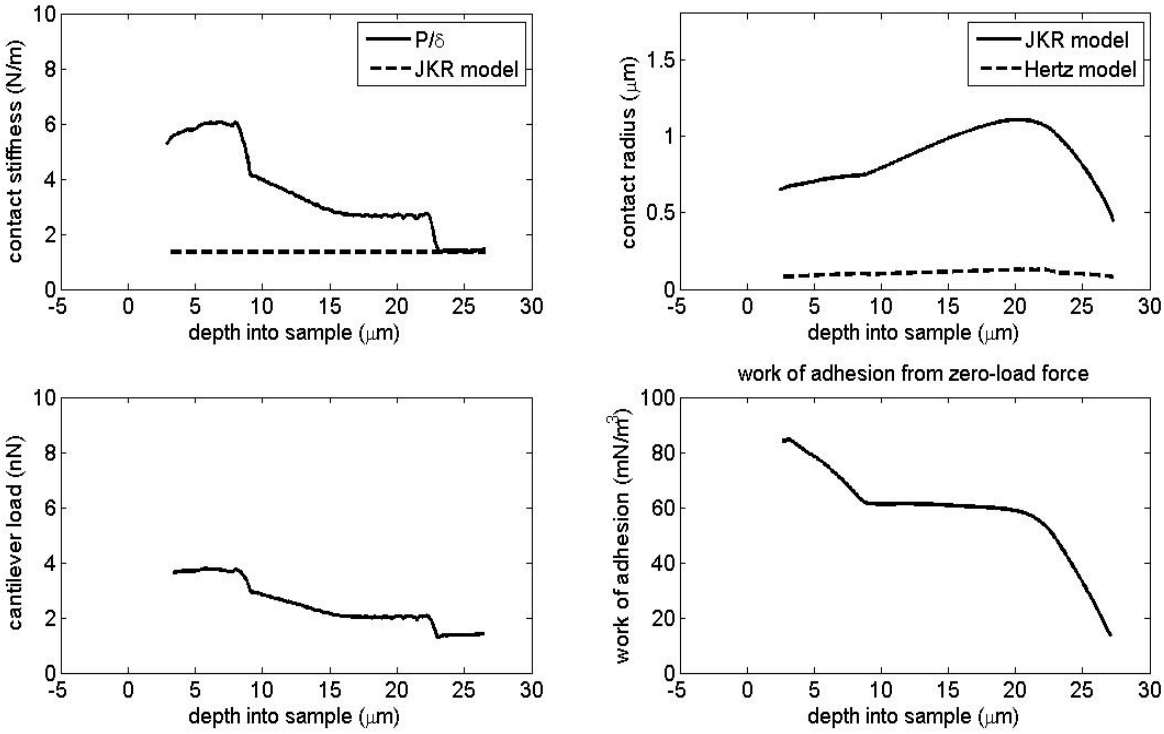

Figure A.4 Side scan of contact stiffness for UV/O_3 surface irradiated PDMS (top left), load on the cantilever as a function of depth (bottom left), and JKR and Hertzian contact model calculations for contact radius (top right) and work of adhesion from the energy release rate on contact detachment (bottom right).

Figure A.4 shows other corresponding properties as a function of the cross-sectional depth of the contact between the glass colloidal probe tip cantilever (k = 18.1394±0.002 N/m, S_{grd} = 14.763 nm/V, U_{grd} = 0.8467) and the PDMS/UVO treated substrate where a discrete film of the order of 10 nm may be elucidated at the top surface of the sample (figure 3.2, top left). A very low roughness surface is required for force measurement (figure. 3.2, bottom right) and penetration resolution 1nN and 1nm, respectively. This high calibration accuracy allows the pulse-force modulation to be performed with a low feedback, which is in turn necessary to maintain contact

with the surface. The work of adhesion (figure A.4, bottom right) measured as the maximum attractive force during the retraction of the AFM cantilever from the surface was used along with the JKR model to calculate the polymer bulk modulus (Chapter 3). Similar data was used for the measurements and calculation of the properties for depth of approximately 30um below the free surface (figure 3.2, bottom).

Appendix F: Areal Power Spectral Density Analysis of Wrinkled PDMS UV/Ozone Treated Surfaces

Data for 2% strain exhibit visible undulations can be measured roughly to 60-80μm wavelength (figure 3.3a). Most of the power is concentrated along one dimension since the wrinkles were produced uniaxially, with a bit of a tilt in two direction, 60 and 120 degrees (figure A.5, top left and top right angular spectrum). Smaller wrinkle shows at 6-10μm wavelength, but due to some wrinkle defects some of the frequencies necessary to reconstitute the profile are well distributed at the lower end of the frequency spectrum (figure A.5, top right radial spectrum). The 2-dimensional spectrum in bottom left of figure A.5, shows that most of the power is concentrated along one dimension since the wrinkles were produced uniaxially. There is still angular information in the 2D spectrum due to the surface tilt of the wrinkles in the AFM image (figure 3.3). Angular tilt shows up at 20 degrees and the radial spectrum (figure A.5, bottom right radial spectrum) showing the wrinkles in figure 3.3b to be on the range between 70-80nm in wavelength.

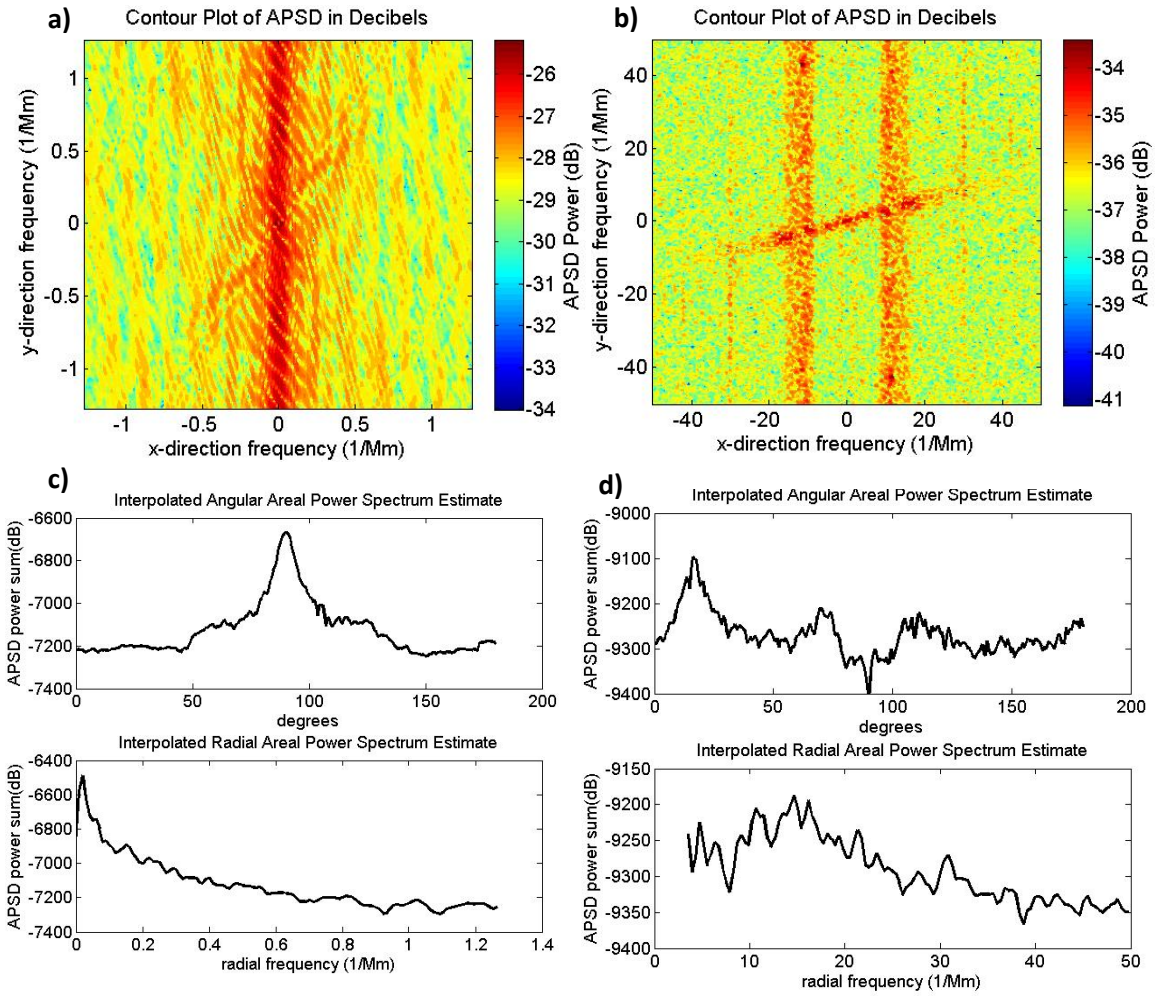

Figure A.5 Areal power spectrum density analysis of the 2D AFM images in figure 3.3. The contour plots for the micron-scale (a) and and nano-scale (b) images show the wavelength distribution of the wrinkles along with their respective (c, d) angular and radial distributions.

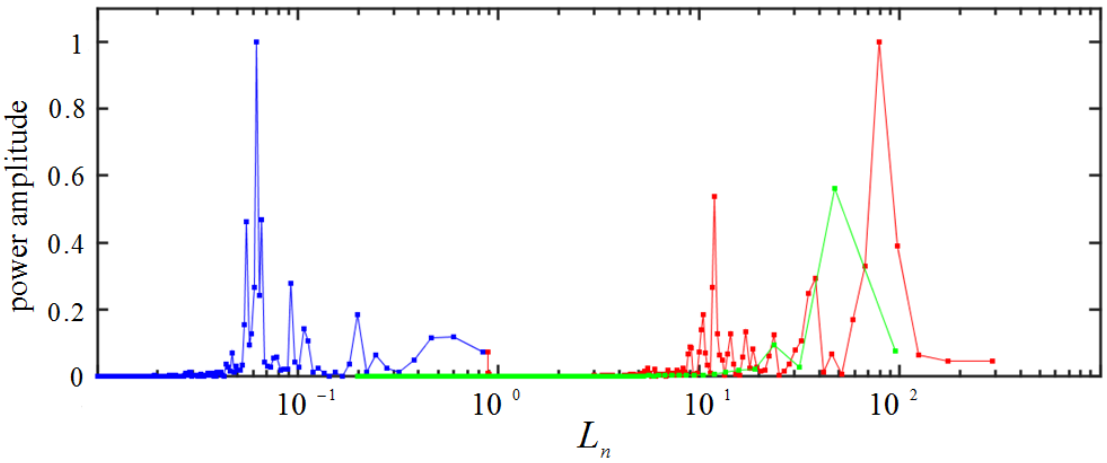

Figure A.6 Power spectrum FFT analysis of a cross-sectional cut of a PDMS UV/O treated wrinkled sample. The blue, and green and red lines show the wavelength spectrum for the nano-scale AFM images, and micron-scale optical micrographs, respectively.

Figure A.6 shows a 1-dimensional FFT analysis done on the micrograph of the cross-section of a PDMS UV\O treated sample, after release from a pre-strain greater than 2%.

Appendix G: Kinematical and Constitutive Treatment

The bodies in contact are mathematically defined as a configuration of points in R space bounded by a piecewise smooth boundary. For mathematical simplicity the deformation will be confined to one of the bodies and will be described in terms of undeformed (B) and deformed body (B_t) configurations mapped by a motion ($\chi(\mathbf{X},t):B\rightarrow B_t$) described in the material frame. The motion ($\mathbf{x} = \chi(\mathbf{X}, t)$) relating the new position ($\mathbf{x}$) of the material points ($\mathbf{X}$) at time (t) is regular (C^2) which means that it is a homeomorphism, that is a piecewise continuous or smooth, one-to-one

mapping with an inverse ($\exists : \chi^{-1}$) where nothing catastrophic occurs. The relationship between deformed and undeformed bodies will be given by the three-dimensional mapping defined by the convective derivative of the motion, which is known as the deformation gradient, denoted by: $\underline{\mathbf{F}}(\mathbf{X},t) = \nabla \chi(\mathbf{X},t)$. Therefore in material terms the deformation gradient is given as:

$$\underline{\mathbf{F}}(\mathbf{X},t) = \frac{\partial \mathbf{x}^i}{\partial \mathbf{X}^J}, \qquad \text{(G.1)}$$

which is a mixed Lagrangian-Eulerian tensor ($\underline{\mathbf{F}}: T_{\mathbf{X}}B \rightarrow T_{\mathbf{x}}B_t$; where $B_t = \chi(B)$) (Marsden 1983). In order to produce the motion in the elastic body (B) a traction ($\mathbf{t}$) is applied to the half-space which produces a strain energy (ψ) stored within the elastic solid. The material's tendency to resist deformation may be quantified by the generalized 1st Piola-Kirchoff stress tensor as;

$$\underline{\mathbf{P}} = P g^{ik} \lambda^{ij^{-1}} + 2 \frac{\partial \hat{\psi}_H}{\partial \lambda^{ji}}\bigg|_{\eta,\theta} G^{ik} \lambda^{ji}{}_I \qquad \text{(G.2)}$$

where λ^{ij} is the stretch factor of the deformation gradient tensor (equation G.1), the compressibility term is $P = p + 2J\,\partial \psi_H / \partial J$ with p being an arbitrary function due to hydrostatic pressure or constraint boundary conditions during finite deformation (Rivlin 1948, Green 1952, Gurtin 2012). In this work the spatial transformations given by the metric tensors in undeformed (G^{IK}, G_{IK}) and deformed (g^{ik}, g_{ik}) states remains in the rectangular coordinate system, thereby yielding a regular one-to-one transformation of the: $G^{IK} = g^{ik} = \delta^{ik} = \delta^{IK} = G_{IK} = g_{ik} = \delta_{ik} = \delta_{IK}$ type, where δ^{ik}, δ_{ik} is the Kronecker delta. ψ_H is the stored mechanical energy function given by the

working potential known as the Helmholtz free energy as: $\psi_H = e - \theta\eta$, where the first term on the right represents the changes in internal energy, the second term on the right is the change of total entropy for the polymer chain conformation in the solvent. The constitutive form of each term will be discussed in the following subsection. The counterpart of the 1st Piola-Kirchoff stress tensor in the deformed configuration can be derived by the relationship between the area element in the undeformed and deformed configurations, which is acted upon by the same force through Nanson's equation; $\mathbf{n}da = J\underline{\mathbf{F}}^{T}\mathbf{N}dA$ giving;

$$\underline{\sigma} = \frac{1}{J}\underline{\mathbf{P}}\,\underline{\mathbf{F}}^{T}, \qquad \text{(G.3)}$$

which is Cauchy's measure of stress where J is the Jacobian of the deformation matrix, a measure of the volume strain and given the regular motion $J \geq 1$.

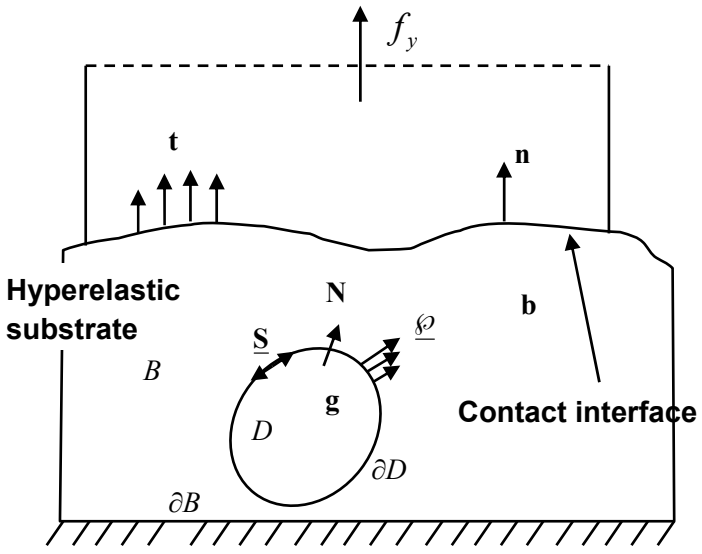

Figure A.7 Contact half-space showing polymer phase domain with Eshelby traction and configurational body forces.

Appendix H: Energy Momentum Tensor

The relationship between the elastic strain energy and the rate at which work is done by the standard and configurationally stresses on the phase domain (D) (figure A.7) is given by

$$\dot{W}(B) = \int_{\partial D} \underline{\wp}\, \mathbf{N} \cdot \mathbf{q}\, dA + \int_{D} \rho_D\, \mathbf{g}\, \cdot \mathbf{q}\, dV + \int_{\partial B} \underline{\mathbf{P}}\, \mathbf{n} \cdot \mathbf{v}^* dA + \int_{B} \rho\, \mathbf{b} \cdot \mathbf{v} dV, \quad \text{(H.1)}$$

where $\wp$ is the Eshelby's energy momentum tensor, which produces a traction acting upon the domain boundary (∂D) (Eshelby 1970), ρ_D and ρ are the mass density for D and the body (B), respectively; as described above, n and N are the vectors normal to ∂B and ∂D, respectively, and $\mathbf{v}^*$ ($= \mathbf{v} + \underline{\mathbf{F}} \cdot \mathbf{q}$) is the referential material velocity fields defined as the sum of the velocity field ($\mathbf{V}$) for B and the material flow rate ($\underline{\mathbf{F}} \cdot \mathbf{q}$) into the domain (Gurtin 2000).

The working balance after substituting the referential velocity and regrouping the terms for the body and the domain yields;

$$\dot{W}(B) = \int_{\partial D} \left(\underline{\wp}\, \mathbf{N} + \underline{\mathbf{P}}\, \underline{\mathbf{F}}\, \mathbf{N} \right) \cdot \mathbf{q}\, dA + \int_{D} \rho_D\, \mathbf{g}\, \cdot \mathbf{q}\, dV + \int_{\partial B} \underline{\mathbf{P}}\, \mathbf{n} \cdot \mathbf{v}\, dA + \int_{B} \rho\, \mathbf{b} \cdot \mathbf{v}\, dV. \quad \text{(H.2)}$$

This is the rate of work done, made invariant with respect to velocity field ($\mathbf{q}$). Satisfying the *Principle of Virtual Work* and the energy conservation axiom (1st Law) of thermodynamics yields the internal workings of the system;

$$0 = \int_{\partial D} \left(\underline{\wp}\, \mathbf{N} + \underline{\mathbf{P}}\,\underline{\mathbf{F}}\,\mathbf{N} \right) \cdot \mathbf{q}\; dA + \int_{D} \rho_D\, \mathbf{g}\; \cdot \mathbf{q}\, dV + \int_{B} \rho \dot{e} - \rho \theta \dot{s} + \nabla \cdot \mathbf{h}\; dV, \quad \text{(H.3)}$$

where $\dot{e}$ is the internal energy, $\dot{s}$ is the rate of heat generation or body configurational entropy production and the **h** is the heat flux vector through the control volume surface of the body (*B*). From the Helmholtz free energy ($\rho \dot{e} = \rho \dot{\psi}_H + \rho \dot{\eta} \theta$), where η is the entropy and θ is the absolute temperature (Kestin 1979), it may be seen that the configurational forces are a means of transforming the elastic energy provided by the external traction (**t**) into the movement of the domains within the body. In many systems this is a dissipative process, which must satisfy the Clausius-Duhem postulate (Flügge 1960**)** which states;

$$\int_{B} \rho \dot{\eta} \theta\, dV \geq \int_{B} \left(\rho\, \theta\, \dot{s} - \nabla \cdot \dot{\mathbf{h}} \right) dV \;\; for\; \forall B, \qquad \text{(H.4)}$$

under isothermal ($\dot{\theta} = 0$) conditions. Therefore, by applying both general axioms, the configurational balance takes the form of;

$$0 = \int_{\partial D} \left(\underline{\wp}\, \mathbf{N} + \underline{\mathbf{P}}\,\underline{\mathbf{F}}\,\mathbf{N} \right) \cdot \mathbf{q}\; dA + \int_{D} \rho_D\, \mathbf{g}\; \cdot \mathbf{q}\, dV + \int_{B} \rho \dot{\psi} - \rho \dot{s}_c \theta\; dV\,. \quad \text{(H.5)}$$

A form of the energy momentum tensor ($\underline{\wp}$) may be elucidated, by using the Reynolds' Transport theorem of the material rate of change over time of the total amount of free energy in the domain volume (Marsden 1983), with equation H.4 and applying the divergence theorem yields the time rate of growth of the free energy within the body (*B*), which is that dissipated on expanding the domain interface by the capillary force on the interface ($\underline{\mathbf{S}}$) (Gurtin 1993), yielding;

$$\frac{D}{Dt}\left\{\int_B \rho\psi_H - \rho s_c\theta\, dV\right\} \geq \int_{\partial D} \underline{\mathbf{S}}\mathbf{n}\cdot\mathbf{q}\, dS$$
$$= \int_D \rho_D\, \mathbf{g}\cdot\underline{\mathbf{F}}\cdot\mathbf{v}^*\, dV + \int_D \rho_D\, \hat{\mathbf{g}}\cdot\mathbf{q}\, dV. \tag{H.6}$$

This yields the simplified version of the configurational force balance,

$$0 = \int_{\partial D} \left(\underline{\wp} + \underline{\mathbf{P}}\,\underline{\mathbf{F}} - [\rho\psi_H - \rho s_c\theta]\,\underline{\mathbf{I}}\right)\mathbf{N}\cdot\mathbf{q}\, dA$$
$$+ \int_B \rho\left(\left(\nabla\psi_H - \nabla s_c\theta - s_c\nabla\theta\right)\underline{\mathbf{I}} + \frac{\rho_D}{\rho}\mathbf{g}\cdot\underline{\mathbf{F}}\right)\cdot\mathbf{v}\, dV \tag{H.7}$$

.

which reveals the true form of the *energy momentum tensor* and the domain *configurational body force* as functions of the free energy.

Eshelby's *energy momentum tensor* and the domain *configurational body force* as functions of the free energy are;

$$\underline{\wp} = [\rho\psi_H - \rho s_c\theta]\underline{\mathbf{I}} - \underline{\mathbf{P}}^{(inh)}\underline{\mathbf{F}}, \tag{H.8}$$

and

$$\mathbf{g} = -J\left(\nabla\psi_H - \nabla s_c\theta - s_c\nabla\theta\right)\underline{\mathbf{F}}^T, \tag{H.9}$$

where $\mathbf{g}$ is the isotropic internal body force have the same field form. In terms of the inhomogeneity domain surface stress, the Eshelby's energy momentum tensor may be expressed as;

$$\underline{\wp} = \underline{\mathbf{S}}\,\underline{\mathbf{K}} - \underline{\mathbf{P}}\underline{\mathbf{F}}, \tag{H.10}$$

where $\underline{\mathbf{S}}$ is the surface capillary stress tensor and $\underline{\mathbf{K}}$ is the curvature tensor.

Appendix I: Energy Momentum Tensor for Hyperelastic Multiphase Solid

Constitutive insight from the general form of the energy momentum tensor given by equation N.6 may be had by making it explicit in terms of the internal energy at the interface ($[e]$) substituting the Helmholtz free energy, where the brackets signify the interfacial jump condition, then;

$$\underline{\wp} = [\rho e - \rho s_c \theta]\underline{\mathbf{I}} - \underline{\mathbf{P}}\underline{\mathbf{F}}, \qquad \text{(I.1)}$$

where $[\rho e]$ and $[\rho s_c \theta]$ are interfacial quantities, defined by jump conditions $[\phi]$. The interfacial laws define the relationship of the Energy Balance for the bulk with respect to the interface, mainly described by the "pill-box" argument (Gurtin 1993), which is nothing more than the application of Reynolds's transport theorem, while acknowledging the principle of interconvertibility of energy;

$$\int_{\partial D} [\rho e] \cdot \mathbf{q}\, dA = \int_{D} \rho \dot{e} \cdot dV + \int_{\partial D} [\mathbf{h}] \cdot \mathbf{N}\, dA + \int_{\partial D} \vec{\mathbf{h}} \cdot \mathbf{q}_{\tan}\, dA + \int_{\partial D} \underline{\mathbf{S}}\,\underline{\mathbf{K}} \cdot \mathbf{q}\, dA, \qquad \text{(I.2)}$$

where $\underline{\mathbf{S}}$ is the surface stress, $\underline{\mathbf{K}}$ is the Weingarten map containing the information on the curvature (Gurtin 1975), and $\mathbf{U}$ is a steady velocity field of the bulk, $\vec{\mathbf{h}}$ represents the heat flux contribution at the edges of the "pill-box", which may be neglected by making it infinitesimally thin; such that; $\vec{\mathbf{h}} = 0$. Substituting the bulk energy balance in place of the internal energy and noting the balance across the interface by the bulk changes in entropy due to the lack of confinement of the polymer yields that the rate

of elastic strain energy is in turn balanced by the rate of work done by the surface stress;

$$\int_D [\underline{\mathbf{P}} : \dot{\underline{\mathbf{F}}}]\, dV = -\int_D \underline{\mathbf{S}}\underline{\mathbf{K}} \cdot \mathbf{U}_N \, dA \,. \tag{I.3}$$

This is a generalized form of *Laplace's constitutive equation* for a liquid droplet in equilibrium; $[p] = \gamma\bar{\kappa}$, where $\bar{\kappa}$ is the mean curvature, γ is the surface tension and $[p]$ is the scalar pressure difference between inside and outside of the phase (Kestin 1979b, Gurtin 1975). Then the thermostatic energy balance at the interface may be written in terms of the interfacial stress ($\underline{\mathbf{S}}$), entropy and heat flux jump conditions as; $[\rho e]\underline{\mathbf{I}} = \underline{\mathbf{S}}\underline{\mathbf{K}} - (\mu^{(\beta)}[n^{(\beta)}] + [\rho s\theta])\underline{\mathbf{I}}$, where $\mu^{(\beta)}$ is the scalar chemical potential and $n^{(\beta)}$ is the number of species. Further expressing the entropy in terms of its structural and configurational components;

$$[\rho e]\underline{\mathbf{I}} = \underline{\mathbf{S}}\underline{\mathbf{K}} - (\mu^{(\beta)}[\Delta n^{(\beta)}] + [\rho(s_{mix} + s_c)\theta])\underline{\mathbf{I}}, \tag{I.4}$$

where from the Gibbs-Duhem equation (Gibbs 1876) it is known that $[\rho\eta\theta] = -\mu^{(\beta)}[\Delta n^{(\beta)}] + [\rho s_{mix}\theta]$, then equation I.4 substituted into equation I.1 yields the Eshelby's energy momentum tensor in terms of the inhomogeneity domain surface stress as;

$$\underline{\wp} = \underline{\mathbf{S}}\underline{\mathbf{K}} - \underline{\mathbf{P}}\underline{\mathbf{F}}, \tag{I.5}$$

where $\underline{\mathbf{S}}$ is the surface capillary stress and $\underline{\mathbf{K}}$ is the curvature tensor, which is given by the second fundamental form ($\mathbf{II_S(s)}$) of differential geometry in the phase

surface manifold. In other words, the energy momentum tensor is proportional to the interfacial stress due to the interfacial area change produced by the volume increase due in turn to the addition of material to the domain. The surface capillary stress ($\underline{\mathbf{S}}$) on the phase domain boundary (∂D) (Gurtin 1993) has a configurational surface tensile (γ) component, which originates when material is added to the interface as D increases in volume and the surface shearing (ξ) component as this same volume increases and the interface moves in the normal direction; $\underline{\mathbf{S}} = (\gamma\underline{\Xi}+\xi\underline{\aleph})$, where $\underline{\Xi}$ ($=1-\mathbf{e}_3\otimes\mathbf{e}_3$) and $\underline{\aleph}$ ($=\mathbf{e}_1\otimes\mathbf{e}_2+\mathbf{e}_2\otimes\mathbf{e}_1$) are surface and shear projection tensors (Gurtin 1993).

Appendix J: Field Relationships for Dissipation in a Viscoelastic Contact

The entropy generation is given by the Clausius-Duhem postulate (**Truesdell 1984**) as;

$$\rho\dot{\eta} \geq \frac{\widetilde{\mathbf{H}}}{\theta^2}\cdot\nabla\theta - \frac{1}{\theta}\,\nabla\cdot\widetilde{\mathbf{H}} + \rho\dot{s}_{mix}, \qquad \text{(J.1)}$$

where $\widetilde{\mathbf{H}}$ is the heating flux which is ($\equiv \mathbf{H}+\underline{\mathbf{M}}^{(\beta)T}\underline{\Omega}\cdot(\mathbf{v}^{*(\beta)}-\mathbf{c}-\underline{\dot{\Omega}}\,\mathbf{x}^{(\beta)})$) a function of the inner heating flux ($\mathbf{H}$) and the mass flux due to chemical potential ($\underline{\mathbf{M}}$) (Bowen 1976, DeGroot and Mazur 1969) θ is the absolute temperature, and $\dot{s}_{mix}$ is the mixing entropy (Dill 2000). In terms of the energy balance for deformation of an elastic solid, the entropy generation is;

$$\rho\dot{\eta}\theta \geq \rho\dot{e} - \underline{\mathbf{P}}:\underline{\dot{\mathbf{F}}} + \frac{\widetilde{\mathbf{H}}}{\theta}\cdot\nabla\theta - \rho\theta\dot{s}_c, \qquad \text{(J.2)}$$

effectively asserting that the lower limit in production of entropy is due to heat dissipation, mass flow, the maintenance of a thermal gradient, and phase changes due to mixing. The flux of the energy momentum at the inhomogeneity interface is given by the divergence of the energy momentum tensor ($\underline{\wp}$) in equation H.8 as;

$$[\rho \nabla e]\,\underline{\mathbf{I}} = \nabla \cdot \underline{\wp} + [\rho(\theta \nabla s_c + s_c \nabla \theta)]\,\underline{\mathbf{I}} + \nabla \cdot (\underline{\mathbf{P}}\,\underline{\mathbf{F}}), \qquad \text{(J.3)}$$

where $\nabla \cdot \underline{\wp} = \Im^{inh}$ is the configurational inhomogeneity force on the phase domain. Taking its product with the rate of change of the polymer chain radius of gyration ($\dot{\Re}_g$); $\rho \dot{e} = \rho \nabla e \cdot \dot{\Re}_g$, yields the rate of change of the internal energy as a function of the internal variables;

$$\rho \dot{e} = \Im^{inh} \cdot \dot{\Re}_g + [\rho(\theta \nabla s_c + s_c \nabla \theta)] \cdot \dot{\Re}_g + \underline{\mathbf{P}} : \underline{\dot{\mathbf{F}}}, \qquad \text{(J.4)}$$

which by substituting into the Clausius-Duhem inequality (equation J.2) yields;

$$\rho \dot{\eta}\,\theta \geq \Im^{inh} \cdot \dot{\Re}_g + [\rho \dot{s}_c] \nabla \theta + \frac{\widetilde{\mathbf{H}}}{\theta} \cdot \nabla \theta, \qquad \text{(J.5)}$$

where $[\nabla s_c] \cdot \dot{\Re}_g = \dot{s}_c$ and $[\rho s_c] \nabla \theta = \Im^{th}$ is a material thermal force per unit volume (F / L^3), which acts similarly to the inhomogenous force ($\Im^{inh}$) on the manifold ($\mathrm{T}_p M$), (Marsden 1983, Maugin 1999, Maugin 2002) and drives a thermal flux (Hirschfelder 1954). **Equation J.5** shows that making the contact and applying the load produces dissipation, therefore detachment will require an additional amount of energy which will be dissipated. The term $(\dot{\mathbf{H}} / \theta) \cdot \nabla \theta$ is defined by the Helmholtz free energy ($-(\dot{\mathbf{H}} / \theta) \cdot \nabla \theta = \rho \dot{\psi}_H - \underline{\mathbf{P}} : \underline{\dot{\mathbf{F}}} + \rho \dot{\theta} s_c$) and represents the heat flux at the

crack tip during interfacial fracture, which may be defined by the limit of the Knowles-Sternberg's integral (Knowles 1972), referred to by Budianski and Rice (Budianski 1973) as the M-integral;

$$-\lim_{S\to 0}\oint_S\left\{\frac{\widetilde{\mathbf{H}}}{\theta}\cdot\nabla\theta\mathbf{n}\right\}dS=\lim_{S\to 0}\oint_S\left\{\rho\left(\dot{\psi}_H-\dot{\theta}s_c\right)\cdot\mathbf{n}-\mathbf{n}\underline{\mathbf{P}}:\dot{\underline{\mathbf{F}}}\right\}dS$$
$$=\lim_{S\to 0}\oint_S\left\{\rho\left(\psi_H-\theta s_c\right)\cdot\mathbf{n}-\mathbf{n}\underline{\mathbf{P}}:\underline{\mathbf{F}}\right\}dS\cdot\dot{\ell}=-G_{Ic}\cdot\dot{\ell} \tag{J.6}$$

where $\dot{l}$ is the rate of increase in crack length speed and G is the energy release rate. Note that the energy flux into the crack tip is the energy dissipated by crack opening and is given by;

$$\frac{G_{Ic}\cdot\dot{\ell}}{A_c}=\frac{1}{\theta}\mathbf{H}\cdot\nabla\theta. \tag{J.7}$$

Appendix K: Instrumental Analysis of Polymer-Grafted Surfaces

Elliposometry was used to measure the dry thickness of PAA, PS, and PS-b-PAA brushes formed at 12 and 24 hrs grafting reaction times (figure A.8). In general, increasing grafting time led to thicker polymer brushes and the dry thickness varied from approximately 135 to 270 nm over all samples.

X-ray photoelectron spectroscopy (XPS) results further confirmed PAA and PEG deposition based on the elemental carbon peaks near 300 eV, which are consistent with carboxylic acid groups (figure A.9). The presence of Si in these spectra suggests that the deposition was incomplete and that the underlying glass slides were partially exposed.

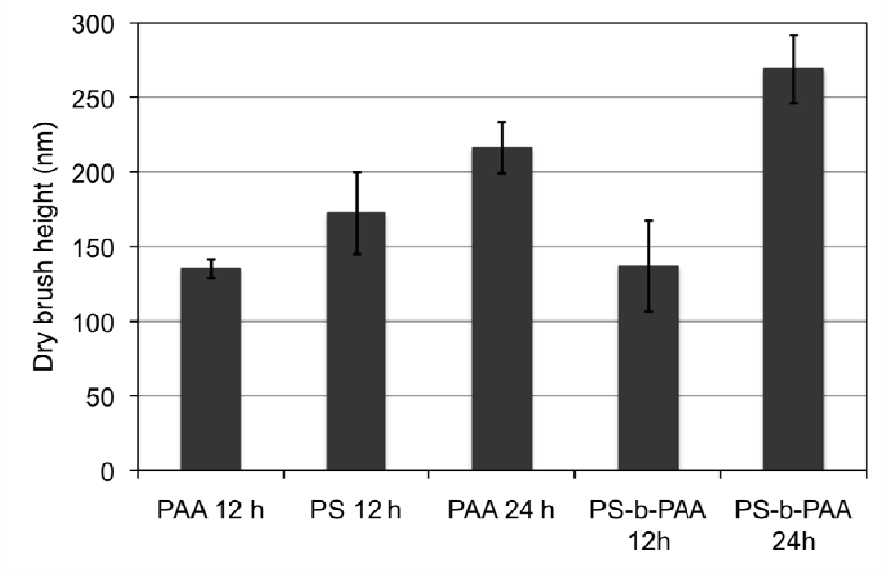

Figure A.8 Dry (concentrated) brush thickness based on ellipsometry (bottom left) for PAA and PS-b-PAA brushes formed on silicon wafers.

Furthermore, it is likely that a single PAA chain (450,000 MW) bound to both the surface sites to adopt a crosslinked carpet configuration, while PEG (20,000 MW) bound at its termini and adopted a brush configuration. XPS results confirmed PAA and PS-b-PAA brush formation. For PAA, Si was observed after 12 hrs of grafting, but was eliminated after 24 hrs consistent with greater brush growth that complete coverage of the substrate. Si was not observed for the remaining brushes. Compared to direct grafting of chains, brush growth via ATRP increased the degree of surface coverage.

Optical measurements of these coatings were performed in order to asses coating quality, as well as transparency (figure A.10a). UV-visible light transmission measurements were also conducted in order to assess coating light transmission

characteristics. An optical transfer function (figure A.10b) was generated from a white light optical test in order to assess the loss of resolution of images through the coatings. The surface-initiated atomic transfer radical polymerization (SI-ATRP) method was proven to be the most efficient in controlling the quality, the thickness of the polymer carpet which makes it more suitable as coating for *naval optical applications*.

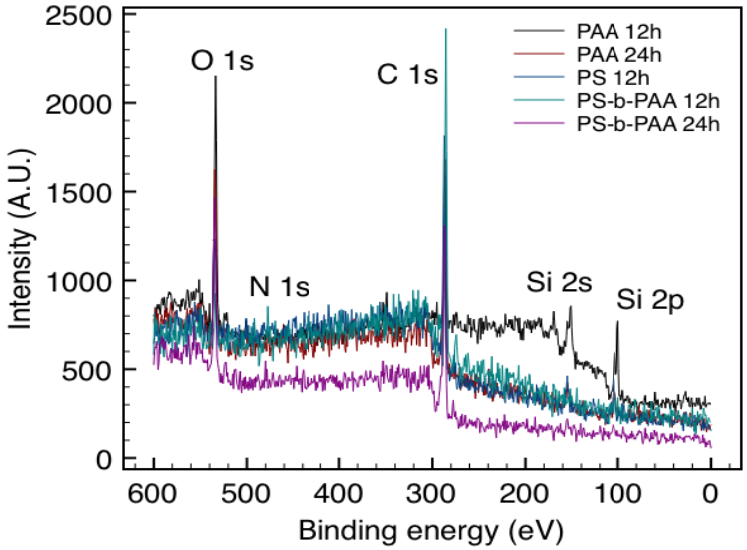

Figure A.9 XPS measurements for PAA and PS-b-PAA brushes formed on silicon wafers at 12 and 24 h grafting times. The binding energies for oxygen, nitrogen, carbon, and silicon are denoted.

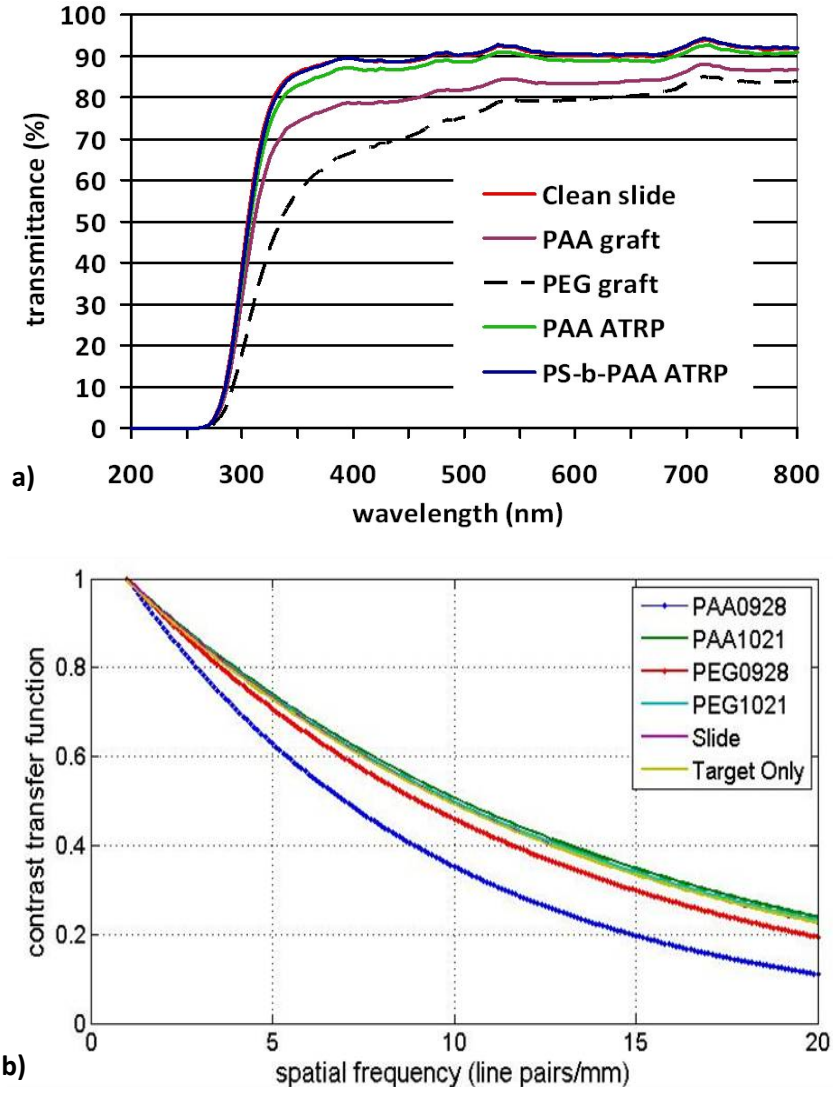

Figure A.10 Transmittance of ultraviolet-visible light (a) through coated glass slides for both grafted (method 1) and directly polymerized brushes (method 2). Contrast transfer function (b) measurement for grafted polymer brush coatings on glass.

Appendix L: Parametric Study Space Range

Table A.1 shows a summary of the mechanical properties of the hydrogel coatings tested along with ulva algae spore settlement tests. No particular property correlates directly with settlement efficiency. A more thorough analysis of all variables from the interaction between constitutive relations and field phenomenological equations satisfying the Buckingham Π theorem is required (Buckingham 1915).

Table A.1 Mechanical properties of hydrogel coatings.

Coating	E*(ω) (MPa)	ω (rads/s)	a_c (μm)	W_{ls} (mJ/m^2)	γ_{ls} (mJ/m^2)	G_{eff} (mJ/m^2)	spored density (no/mm^2)
6hrPS1.0	0.81	942.47	0.97	63.20	7.58	151.36	135.00
6hrPSbPAA 1.0	0.18	942.47	1.02	107.96	0.66	118.75	160.00
6hrPAA1.0	0.25	942.47	1.10	112.22	1.62	311.37	185.00
12hrPAA0.2	0.39	1130.97	0.68	90.60	0.46	139.82	-
12hrPAA0.5	0.15	1256.64	1.51	84.47	4.58	177.13	-
12hrPAA0.8	0.46	1256.63	1.17	98.93	6.62	55.43	-
12hrPAA1.0	0.10	1256.63	1.86	98.93	5.67	202.39	85.00
Hydroxilated Glass	3000	2324.77	1.52	118.23	8.03	118.25	135.00
LUBE10	0.63	10995.57	1.33	118.23	14.88	11.16	-
LUBE100	1.46	10995.57	1.19	143.11	26.52	14.49	-
LUBE200	1.15	10995.57	1.01	143.11	13.05	27.02	-
LUBE250	0.68	10995.57	0.47	143.11	0.97	0.58	-

Table A.2 Parameters to be varied during experiments to elucidate the polymer brush design models.

Coating	$F/R\ (mN/m)$	$\gamma^{(inh)}R/\mu^{(\beta)}$	$W_{ls}\,(mJ/m^2)$	$\phi(a_T\dot{l})\gamma^{(s)}/\gamma^{(inh)}$	$R/10^3 A_c E^* a_T\dot{l}/\omega\gamma^{(inh)}$
Multiphasic	3 - 30	50 –	80 - 140	-10 – 0	~ 10^{-5}
Viscoelastic	35	~ 65	~ 60	-4 – -1	~ 1
Elastic	> 35	-	115 - 120	~ -4	10^8–10^{10}

References:

Andrews, E.H., and Kinloch, A.J., 1973a, "Mechanics of adhesive failure. I," *Proceedings of the Royal Society of London A*, Vol. 332, pp. 385-99.

Andrews, E.H., and Kinloch, A.J., 1973b, "Mechanics of adhesive failure. II," *Proceedings of the Royal Society of London A*, Vol. 332, pp. 401-14.

Aninwene G.E., Abadian, P.N., Ravi, V., Taylor, E.N., Hall, D.M., Mei, A., Jay, G.D., Goluch E.D., and Webster, T.J., 2014, "Lubricin: A novel means to decrease bacterial adhesion and proliferation," *J. Biomedical Materials Research Part A*, DOI: 10.1002/jbm.a.35195.

Asaro, R. J., and Tiller, W. A., 1972, "Interface morphology development during stress corrosion cracking: Part I. Via surface diffusion," *Metallurgical and Materials Transactions B*, Vol. 3, pp. 1789-96.

Asay, D.B., and Kim S.H.*, 2005, "*Evolution of the Adsorbed Water Layer Structure on Silicon Oxide at Room Temperature," *J. Physical Chemistry B,*Vol. 109, pp. 16760-3.

Bowen, R.M., 1967, "Toward a Thermodynamics and Mechanics of Mixtures," *Archives Rational Mechanics and Analysis*, Vol. 24, pp. 370-403.

Bowen, R.M., 1976, "Theory of Mixtures," Part I of Vol. III; in Continuum Physics ed. by Eringen, A.C., Academic Press, New York, NY., pp. 2-122.

Broek, D., 1982, Elementary Engineering Fracture Mechanics, 3rd ed., *Kluwer Academic Publishers Group*, The Hague, The Netherlands, pp. 120, 290.

Buckingham, E., 1915, "Model Experiments and the Forms of Empirical Equations," *Transactions of the American Society of Mechanical Engineers*, New York, NY., Vol. 37, No. 1487, pp. 263-96.

Budianski, B., and Rice, J.R., 1973, "Conservation Laws and Energy-Release Rates," *J. of Applied Mechanics*, Vol. 40, pp. 201-03.

Callow, J.A., and Callow, M.E.,, 2006, "The Ulva Spore Adhesive System," In: Biological Adhesives, ed. By A.M. Smith and J.A. Callow, *Springer-Verlag*, Berlin Heidelberg, pp. 64.

Callow M.E., Callow, J.A., Ista, L.K., Coleman, S.E., Nolasco, A.C., and Lopez, G.P., 2000, "Use of Self-Assembled Monolayers of Different Wettabilities To Study Surface and Primary Adhesion Processes of Green Algal (*Enteromorpha*) Zoospores," *Appl. and Environ. Microbiol*., Vol. 66(8), pp. 3249-54.

Chen, I.J., and Lindner, E., 2007, "The stability of radio-frequency plasma-treated polydimethylsiloxane surfaces." *Langmuir*, Vol. **23**, pp. 3118–22.

Cherepanov, G.P., 1967, "Crack Propagation in Continuous Media," *P.M.M*., Vol. 31, pp. 467-88.

Chung, J.Y., Kim, K.H., Chaudhury, M.K., Sarkar, J., and Sharma, A., 2006, "Confinement-induced instability and adhesive failure between dissimilar thin elastic films," *European Physics J. E.*, Vol. 20, pp. 47-53.

Cleveland, J.P., Manne, S., Bocek, D., and Hansma, P.K., 1993, "A nondestructive method for determining the spring constant of cantilevers for scanning force microscopy," *Review of Scientific Instr*uments, Vol. 64(2), pp. 403-05.

Costerton, J.W., Stewart, P.S., and Ogden, S., 2001, "Battling Biofilms; The War is Against Bacterial Colonies that Cause Some of the Most Tenacious Infectious Known. The Weapon is Knowledge of the Enemy's Communication System," *Scientific American*, Vol. 284(7), pp. 75-81.

deGennes, P.G., 1979, Scaling Concepts in Polymer Physics, *Cornell University Press, Ithaca, NY.*, pp. 159.

deGennes, P.G., 1987, "Polymers at an Interface; A Simplified View," *Advances in Colloid and Interface Sciences*, Vol. 27, pp. 189-209.

deGroot, S.R., and Mazur, P., 1969, Non-Equilibrium Thermodynamics, *North-Holland Publishing Co.,* Amsterdam, NL., pp. 45.

Dill, K.A, and Bronberg, S., 2003, Molecular Driving Forces: Statistical Thermodynamics in Chemistry and Biology, *Garland Science,* New York, NY., pp. 267-76, 328-29.

Doi, M., and Edwards, S.F., 1986, The Theory of Polymer Dynamics, *Oxford University Press*, Oxford, UK, pp. 48-9, 103-4.

Efimenko, K., Wallace, W.E., and Genzer, J., 2002, "Surface Modification of Sylgard-184 Poly(dimethyl siloxane) Networks by Ultraviolet and Ultraviolet/Ozone Treatment," *J. Colloid Interface Science*, Vol 254, pp. 306-15.

Eshelby, J.D., 1970, "Energy Relations and the Energy-Momentum Tensor in Continuum Mechanics," in Inelastic Behavior of Solids ed. Kanninen, M.F., Adler, W.F., Rosenfield, A.R., and Jaffee, R.I., *McGraw-Hill Book Co.*, pp. 77-115.

Ferry, J.D., 1961, Viscoelastic Properties of Polymers, John Wiley & Sons, Inc., New York, NY, pp. 247-363.

Figliola, R.S., and Beasly, D.E.,1995, Theory and Design for Mechanical Measurements, 2nd ed., *John Wiley & Sons, Inc*., New York, NY, pp. 177-87.

Flory, P.J., and Rehner, J., 1943, "Statistical Mechanics of Cross-Linked Polymer Networks II. Swelling," *J. of Chemical Physics*, Vol. 11(11), pp. 521-26.

Flory, P.J., 1944, "Thermodynamics of Heterogeneous Polymers and Their Solutions," *J. of Chemical Physics*, Vol. 12(11), pp. 425-38.

Freund, L.B., 1998, "A Surface Chemical Potential for Elastic Solids," *J. Mechanics and Physics of Solids*, Vol. 46, pp. 1835-44.

Gao, H. and Yao, H., 2004, "Shape insensitive optimal adhesion of nanoscale fibrillar structures," *Proeedings of the National Academy of Science of the United States of America*, Vol. 101(21), pp. 7851-56.

Gent, A.N. and Petrich, R.P., 1969, "Adhesion of Viscoelastic Materials to Rigid Substrates," *Proceedings of the Royal Society of London A*, Vol. 310, pp. 433-48.

Gent, A.N., and Schultz, J., 1972, "Effects of Wetting Liquids on the Strength of Adhesion of Viscoelastic Materials," *J. Adhesion*, Vol. 3, pp. 281-294.

Genzer, J., and Efimenko, K., 2006, "Recent developments in Superhydrophobic surfaces and their relevance to marine fouling: a review," *Biofouling*, Vol. 22(5), pp. 339-60.

Green, A.E., Rivlin, R.S., and Shield, R.T., 1952, "General Theory of Small Elastic Deformations Superposed on Finite Elastic Deformations," *Proceedings of the Royal Society of London A*, Vol. 211, pp. 128-154.

Greenwood, J.A., and Johnson, K.L., 1981, "The mechanics of adhesion of viscoelastic solids," *Philosophical Magazine A*, Vol. 43(3), pp. 697-711.

Griffith, A.A., 1921, "The Phenomena of Rupture and Flow in Solids," *Philosophical Transactions of the Royal Society of London*, Vol. 221, pp. 163-98.

Gudipati, C.S., Finlay, J.A., Callow, J.A., Callow, M.E., and Wooley, K.E., 2005, "The Antifouling and Fouling-Release Perfomance of Hyperbranched Fluoropolymer (HBFP)-Poly(ethyleneglycol) (PEG) Composite Coatings Evaluated by Adsorption of Biomacromolecules and the Green Fouling Alga *Ulva,* " *Langmuir*, Vol. 20, pp. 3044-53.

Gurtin, M.E., 1993, Thermomechanics of Evolving Phase Boundaries in the Plane, *Springer-Verlag*, Berlin, Germany, pp. 26-37.

Gurtin, M.E., 2000, Configurational Forces as Basic Concepts of Continuous Physics, *Oxford University Press*, Oxford, UK, pp. 29-45, 63-65, 132.

Gurtin, M.E., Fried, E., and Anand, L., 2012, The Mechanics and Thermodynamics of Continua, *Cambridge University Press*, Cambridge, UK., pp. 291, 319-22.

Gurtin, M.E., and Murdoch, A.I., 1975, "A Continuum Theory of Elastic Material Surfaces," *Arch. Rational Mech. Anal*., Vol. 57, pp. 291-327.

Hertz, H., 1881, "On the Contact of Elastic Solids," *Journal fur die reine und angewundte Mathematik*, Vol. 92, pp. 156-71, reprinted in Miscellaneous

Papers; Hertz, Heinrich, 1857-1894, by *Hardpress Publishing*, Miami, FL., pp. 146-62.

Hillborg, H., Tomczak, N., Olah, A., Schonherr, H., and Vancso, G.J., 2004, "Nanoscale Hydrophobic Recovery: A Chemical Force Microscopy Study of UV/Ozone-Treated Cross-Linked Poly(dimethylsiloxane)," *Langmuir*, Vol. 20, pp. 785-94.

Hirschefelder, J.O., Curtis, C.F., and Bird, R.B., 1954, Molecular Theory of Gases and Liquids, *John Wiley & Sons*, New York, NY, pp. .

Hoipkemeier-Wilson, L., Schumacher, J.F., Carman, M.L., Gibson, A.L., Feinberg, A.W., Callow, M.E., Finlay, J.A., and Brennan, A.B., 2004, "Antifouling Potential of Lubricious, Micro-engineered, PDMS Elastomes against Zoospores of Green Fouling Alga *Ulva* (Enteromorpha)," *Biofouling*, Vol. 20(1), pp. 53-63.

Hong, W., Liu, Z., and Suo, Z., 2008, "Inhomogeneous swelling of a gel in equilibrium with a solvent and mechanical load," *International J. of Solids and Structures*, Vol. 46, pp. 3282-89.

Hong, W., Zhao, X., Zhou, J., and Suo, Z., 2009, "A theory of coupled diffusion and large deformation in polymeric gels," *J. of the Mechanics and Physics of Solids*, Vol. 56, pp. 1779-93.

Huergo, J., 2003, "Meanwhile, Back to Barnacles…," ONR Public affairs office, Media Releases, 1/23/2003.

Israelachvili, J.N., 1991, Intermolecular and Surface Forces, 2nd ed., *Academic Press*, San Diego, CA., pp.150, 319-22.

Jay, G.D., 1992, "Characterization of a bovine synovial fluid lubricating factor. I. Chemical, surface activity and lubricating properties," *Connective Tissue Research*, Vol. 28, pp. 71–88.

Jay G.D., Harris D.A., and Cha C-J., 2001, "Boundary lubrication by lubricin is mediated by O-linked β(1-3)Gal-GalNAc oligosaccharides," *Glycoconjugates J.*, Vol. 18, pp. 807–15.

Jay, G.D., Torres, J.R., Rhee, D.K.,. Helminen, H.K., Hytinnen, M.M., Cha, C-J., Elsaid, K., Kim, K-S., Cui, Y., and Warman, M.L., 2007a, "Association Between Friction and Wear in Diarthrodial Joints Lacking Lubricin," ***Arthritis & Rheumatism,*** Vol. 56(11), pp. 3662-69.

Jay, G.D., Torres, J.R., Warman, M.L., Laxer, R.M., Laderer, M., and Breuer, K.S., 2007b, "The role of lubricin in the mechanical behavior of synovial fluid," *Proeedings of the National Academy of Science of the United States of America*, Vol. 104(5), pp. 6194-99.

Johnson, K.L., Kendall, K., and Roberts, A.D., 1971, "Surface energy and the contact of elastic solids," *Proceedings of the Royal Society of London A*, Vol. 324, pp. 301–313.

Johnson, K.L., 1995, "The Adhesion of Two Elastic Bodies with Slightly Wavy Surfaces," Int. J. Solids Structures, Vol. 32(3/4), pp. 423-30.

Jones, R.A.L., 2002, Soft Condensed Matter, *Oxford University Press*, New York, N.Y., pp. 33.

Kaelble, D.H., 1964, "Theory and analysis of peel adhesion: Rate-temperature dependence of viscoelastic interlayers," *J. Colloid Interface Science*, Vol. 19, pp. 413-24.

Kavanagh CJ, Swain GW, Kovach BS, Stein J, Darkangelo-Wood C, Truby K, Holm E, Montemarano J, Meyer A, and Wiebe D., 2003, "The effects of silicone fluid additives and silicone elastomer matrices on barnacle adhesion strength," *Biofouling*, Vol. 19(6), pp. 381-90.

Kesari, H., 2010, "Role of surface roughness in hysteresis during adhesive elastic contact," *Phiosophical Magazine Letters*, Vol. 90(12), pp. 892-902.

Kinsler, L.E., Frey, A.R., Coppens, A.B., and Sanders, J.V., 2000, Fundamentals of Acoustics, 4th ed., *John Wiley & Sons, Inc*., New York, NY, pp. 8 – 11.

Knowles, J.K., and Sternberg, E., 1972, "On a Class of Conservation Laws in Linearized Finite Elastostatics," *Archives Rational Mechanics Anal*ysis, Vol. 44, pp. 187-211.

Krotil, H-S., Stifter, T., Waschipky, H., Weishaupt, K., Hild, S., and Marti, O., 1999, Pulsed force mode: a new method for the investigation of surface properties," *Surface Interface Analysis*, Vol. 27, pp. 336-40.

Larche, F. and Cahn, J.W., 1984, "Thermocmechanical equilibrium of multiphase solids under stress," *Acta Metallurgica*, Vol. 26, pp. 1579-89.

Li, Q., and Kim, K.-S., 2009, "Micromechanics of Rough Surface Adhesion: A Homogenized Projection Method," *Acta Mechanica Solida Sinica*, Vol. 22(5), pp. 377-90.

Li, Q., Kim, K.-S. and Rydberg, A., 2006 "Lateral force calibration of an atomic force microscope with a diamagnetic levitation spring system," Review of Scientific Instruments, Vol. 77, pp. 065105.

Li, J., Hu, Y., Vlassak, J.J., and Suo, Z., 2012, "Experimental determination of equations of state for ideal elastomeric gels," *Soft Matter*, Vol. 8, pp. 8121-28.

Long, C.J., Schumacher, J.F., and Brennan, A.B., 2009, "Potential for Tunable Static and Dynamic Contact Angle Anisotropy on Gradient Microscale Patterned Topographies," *Langmuir*, Vol. 25, pp. 12982-9.

Marsden, J.E., and Hughes, T.J.R., 1983, Mathematical Foundations of Elasticity, *Prentince-Hall Inc.*, Englewood Cliffs, NJ., pp. 36, 176-79.

Maugin, G.A., 1992, The Thermomechanics of Plasticity and Fracture, *Cambridge University Press*, Cambridge, UK., pp. 148.

Maugin, G.A., 1999, The Thermomechanics of Nonlinear Irreversible Behaviors: An Introduction, *World Scientific Publishing Co.*, London, UK., pp. 433.

Maugin, G.A., 2002, "Remarks on the Eshelbian thermomechanics of materials", *Mechanics Research Communications*, Vol. 29, pp. 537-42.

Maugis, D., 1992, "Adhesion of spheres: the JKR-DMT transition using a Dugdale model," *J. Colloid and Interface Sc*ience, Vol. 150, pp. 243-69.

Maugis, D., and Barquins, M., 1978, "Fracture mechanics and the adherence of viscoelastic bodies," *J.Phys. D: Applied Physics*, Vol. 11, 1989-2023.

Nonnenmacher, M., Greschner, J., Wolter, O., and Kassing, R., 1991, "Scanning force microscopy with micromachined silicon sensors," *J. of Vauum Science Techno!ogy B*, Vol. 9(2), pp. 1358-62.

Ouyang, M., Yuan, C., Muisener, R.J., Boulares, A., and Koberstein, J.T., 2000, "Conversion of Some Siloxane Polymers to Silicon Oxide by UV/Ozone Photochemical Processes," *Chemistry of Material*, Vol. 12, pp. 1591-96.

Radin, E.L., Swann, D.A., and Weisser, P.A., 1970 "Separation of a hyaluronate-free lubricating fraction from synovial fluid," *Nature*, Vol. 228, pp. 377-78.

Rhee, D.K., Marcelino, J., Baker, M., Gong, Y., Smits, P., Lefebvre, V., Jay, G.,D., Stewart, M., Wang, H., Warman, M.L., and Carpten, J.D., 2005, "The secreted glycoprotein lubricin protects cartilage surfaces and inhibits synovial cell overgrowth," *J. of Clinical Investigation*, Vol. 115(3), pp. 622-31.

Rahmawan, Y., Moon, M.-W., Kim, K.-S., Lee, K.-R., and Suh, K.-Y., 2010, "Wrinkled, Dual-Scale Structures of Diamond-Like Carbon (DLC) for Superhydrophobicity," *Langmuir*, Vol. 26, pp. 484-91.

Sader, J.E., Chon, J.W.M., and Mulvaney, P., 1999, "Calibration of rectangular atomic force microscope cantilevers," *Review of Scientific Instrum*ents, Vol. 70(10), pp. 3967-69.

Sader, J.E., 1999b, "Frequency response of cantilever beams immersed in viscous fluids with applications to the atomic force microscope," *J. of Applied Physics*, Vol. 84(1), pp. 64-76.

Sigal, G.B., Mrksich, M., and Whitesides, G.M., 1998, "Effects of Surface Wettability on the Adsorption of Proteins," *J. Am. Chem. Soc.*, Vol. 120, 3464-73.

Shield, T.W., Kim K.-S., and Shield, R.T., 1994, "The buckling of an elastic layer bonded to an elasticsubstrate in plane strain," *J. Applied Mechanics*, Vol. **61**, pp. 231–35.

Shultz, A.R., and Flory, P.J., 1952, "Phase Equilibria in Polymer-Solvent Systems," *J. of the American Chemical Society*, Vol. 74(19), pp. 4760-67.

Statz, A., Finlay, J., Dalsin, J., Callow, M., Callow, J.A., and Messersmith, P.B., 2006, "Algal antifouling and fouling-release of metal properties of metal surfaces coated with a polymer inspired by marine mussels," *Biofouling*, Vol. 22(6), pp. 391-99.

Sun, J.-Y., Xia, S., Moon, M.-W., Oh, K.H., and Kim, K.-S., 2011, "Folding wrinkles of a thin stiff layer on a soft substrate," *Proceedings of the Royal Society of London A*, Vol. 468, pp. 932–53.

Taylor, J.R. , 2005, Classical Mechanics, *University Science Books*, Sausalito CA, pp. 173, 272, 378-86.

Truesdell, C.A., 1984, Rational Thermodynamics, *Springer-Verlag*, Berlin, Germany, pp. 107-18, 219-36.

Timoshenko, S., and Woinowsky-Krieger, S., 1959, Theory of Plates and Shells, 2nd ed., *McGraw–Hill*, New York, NY, pp. 5.

Torres, J.R., Jay, G.D., Warman, M.L., and Kim, K-S., 2005, "Adhesive Force Reduction and Molecular Aggregation on Lubricin-Coated Contacts," *Proceedings of the World Tribology Congress*, WTC2005-64016.

Torii, A., Sasakiz, M., Hanex, K., and Okuma, S., 1996 "A method for determining the spring constant of cantilevers for atomic force microscopy," *Measurement Science and Technology*, Vol. 7, pp. 179–84.

Tortonese, M., and Kirk, M., 1997, "Characterization of application specific probes for SPMs," *SPIE* 3009, 0277-786X.

Williams, M.L., Landel, R.F., and Ferry, J.D., 1955, "The Temperature Dependence of Relaxation Mechanisms in Amorphous Polymers and Other Glass-forming Liquids," *J. of American Chemical Society*, pp. 3701-07.

Wenzel, R.N., 1936, "Resistance of Solid Surfaces to Wetting by Water," *Industrial & Enginering Chemical Research*, Vol. 28, pp. 988.

Westergaard, H.M., 1939, "Bearing Pressures on Cracks," *J. of Appl. Mech*., Vol. 6, pp. A49-A53.

Wu, C.H., 1996, "The Chemical Potential for Stress-driven Surface Diffusion," *J. of the Mechanics and Physics of Solids*, Vol. 49, pp. 2059-77.

Wu, M.S. and Kirchner, H.O.K., 2010, "Nonlinear elasticity modeling of biogels," *J. of the Mechanics and Physics of Solids*, Vol. 58, pp. 300-10.

Zappone, B., Ruths, M., Greene, G.W., Jay, G.D., and Israelachvili, J.N., 2007, "Adsorption, Lubrication, and Wear of Lubricin on Model Surfaces: Polymer Brush-Like Behavior of a Glycoprotein," *Biophysical J.*, Vol. 92(5), pp. 1693–1708.

Zhang, Z., Zhang, Z.T., Zhang, Y.W., Kim, K.-S., and Gao, H., 2012, "Strain-controlled switching of hierarchically wrinkled surfaces between superhydrophobicity and superhydrophilicity," *Langmuir*, 28 , pp. 2753–60.